論文 / 著書情報
Article / Book Information

題目(和文)	ATLAS検出器を用いたヒッグスを介し崩壊するチャージーノ・ニュートラリーノ対の直接生成事象探索
Title(English)	Search for direct production of charginos and neutralinos decaying via Higgs boson with the ATLAS detector
著者(和文)	留目和輝
Author(English)	Kazuki Todome
出典(和文)	学位:博士(理学), 学位授与機関:東京工業大学, 報告番号:甲第10929号, 授与年月日:2018年9月20日, 学位の種別:課程博士, 審査員:陣内 修,久世 正弘,河合 誠之,中村 隆司,山口 昌英
Citation(English)	Degree:Doctor (Science), Conferring organization: Tokyo Institute of Technology, Report number:甲第10929号, Conferred date:2018/9/20, Degree Type:Course doctor, Examiner:,,,,
学位種別(和文)	博士論文
Type(English)	Doctoral Thesis

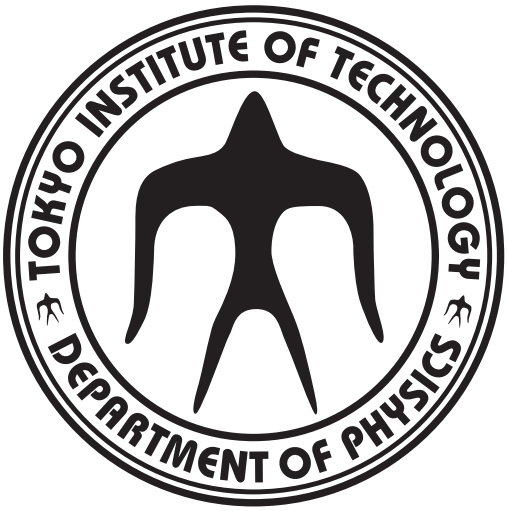

Ph.D Thesis

Search for direct production of charginos and neutralinos decaying via Higgs boson with the ATLAS detector

Kazuki Todome
Tokyo Institute of Technology, Department of Physics
Jinnouchi Lab.

August, 2018

Abstract

The basic model for particle physics, the Standard Model (SM), gives precise predictions, which have been verified by various experiments in past years. However, there are some problems which cannot be explained by the SM, such as the hierarchy problem and dark matter. In order to give solutions to the problems, various types of beyond the standard models have been proposed. One of such models is the SUperSYmmetry (SUSY). This thesis presents a search for the direct production of charginos $\tilde{\chi}_1^{\pm}$ and neutralinos $\tilde{\chi}_2^0$ which are the super partners of the gauge bosons predicted by the SUSY model.

In this thesis, the events where charginos decay via W boson and second lightest neutralinos decay via Higgs, and then Higgs decays to diphoton and W decays to $\ell\nu$, such as

$$pp \to \tilde{\chi}_2^0 + \tilde{\chi}_1^{\pm} \to \tilde{\chi}_1^0 + h + \tilde{\chi}_1^0 + W \to \tilde{\chi}_1^0 + \gamma + \gamma + \tilde{\chi}_1^0 + \ell + \nu$$

is chosen as the target process. In this channel, some of background processes are strongly suppressed by using a mass reconstructed by diphoton. Therefore, although expected signal yields are relatively lower than other channels, high significance is expected due to the scarce backgrounds.

The analysis is performed with 36.1 fb^{-1} of $\sqrt{s} = 13$ TeV proton-proton collision data collected by the ATLAS detector at LHC in 2015 and 2016. The background sources which can be suppressed by the diphoton mass cut are classified as non-peaking background, and the background sources which have Higgs in their process are classified as peaking background. The yield of non-peaking background is evaluated by data-driven method using data out of the signal region. And the yields of peaking background and signals are evaluated using simulation samples.

The analysis procedure has been constructed based on the previous analysis performed with $\sqrt{s} =$ 8 TeV proton-proton collision data. A new selection criterion, b-jet veto, is introduced, in order to suppress one major background, $t\bar{t}h$ process. This new selection improves sensitivity by $\sim 10\%$. Then, defined signal region is further optimized by dividing into two regions, SRa and SRd, instead to use tight criteria. Using the divided signal regions, significance is improved by $\sim 300\%$ at maximum.

Based on the optimized signal region, expected limit on excluded model parameters is evaluated. Evaluated limit is distributed around $m_{\tilde{\chi}_1^{\pm},\tilde{\chi}_2^0} = 180$ GeV, which is improved from $m_{\tilde{\chi}_1^{\pm},\tilde{\chi}_2^0} = 160$ GeV of the limit evaluated in the 8 TeV analysis.

After the study above have been performed, the data is unblinded to compare with the expectation. There are two events in SRa and nine events in SRd, which 0.36 ± 0.22 events and 5.35 ± 0.95 events are expected in SRa and SRd respectively. This mild excess is equivalent to 1.93σ deviation in SRa and 1.36σ deviation in SRd. Model dependent upper limits on the signal cross section are evaluated for all model assumed in the analysis. All the evaluated upper limits on the cross section are larger than the assumed model. Therefore, no model assumed in the analysis were excluded. Model independent upper limits on the signal yields are evaluated as 5.7 fb in SRa and 10.4 fb in SRd. These results suggest importance of further study with more data statistics expected in the on-going and future experiments.

Contents

Chapter 1

Introduction

The Standard Model (SM) of the particle physics was established in the late '60. It precisely describes the particles phenomena, and most of the observations and measurements from the experiments agree with the predictions by the SM so far. However, there are some facts that cannot be explained by the SM. In order to explain those, many extended models are proposed, which are known as Beyond Standard Models (BSM). One of the promissing BSM is the SUperSYmmetry (SUSY) theory. In this chapter, theoretical and experimental backgrounds of the particle physics are reviewed.

1.1 Standard Model

The Standard Model (SM) is the basic theoretical framework for the particle physics. The SM gives predictions about interactions and behaviour of elementary particles. The SM assumes twelve flavor of fermions, which have 1/2 of spin and consist "matter", and three types of interactions via bosons.

Table 1.1 shows the summary of the fermions. As shown in the table, the fermions consist of six types of quarks and six types of leptons. Both of them are categorized into three generations. The type is denoted as "flavor".

The interaction between those fermions are mediated by the propagation of the vector bosons following gauge theory. The bosons assumed in the SM are summarized in Table 1.2. As shown in the table, interactions in the SM are explained by two theories; the Quantum ChromoDynamics (QCD), which has $SU(3)_C$ symmetry, and the Glashow-Weinberg-Salam (GWS) theory, which has $SU(2)_L \times U(1)_{EM}$ symmetry.

The QCD explains the strong interactions between "coloured" particles such as quarks and gluons which are force carrier particles in the strong interaction [1]. Since gluons themselves have colour,

Table1.1 Fermions in Standard Model

Category	Generations			Charge
	1st	2nd	3rd	
Quarks	up (u)	charm (c)	top (t)	+2/3
	down (d)	strange (s)	bottom (b)	-1/3
Leptons	electron (e)	muon (μ)	tauon (τ)	-1
	electron neutrino (ν_e)	mu neutrino (ν_μ)	tau neutrino (ν_τ)	0

Table1.2 Bosons in Standard Model

Name		Interactions	Charge	Theory
Gluon	(g)	Strong	0	Quantum Chromodynamics
photon	(γ)	Electromagnetic	0	Glashow-Weinberg-Salam theory
Weak boson	($W^\pm$)	Wek	± 1	
	(Z^0)		0	

the potential between coloured particles is increased in proportion to the distance between particles. From increased potential, another pair of coloured particles are generated. As a result, coloured particles cannot be observed directly and only colour singlet hadrons can be observed. This is called "colour confinement".

The GWS theory explains the unified electroweak interaction [2, 3, 4]. At first, two fields are introduced; $SU(2)_L$ gauge field ($\mathbf{W}_\mu$) and $U(1)_{EM}$ gauge field (B_μ). Those fields under the gauge symmetries expect mass less bosons. Then, after the spontaneous symmetry breaking, often called as the Brout-Englert-Higgs mechanism, those two fields are mixed as following:

$$W_\mu^\pm = \frac{1}{\sqrt{2}}(W_\mu^1 \mp iW_\mu^2) \tag{1.1}$$

$$Z_\mu = W_\mu^3 \cos\theta_W - B_\mu \sin\theta_W \tag{1.2}$$

$$A_\mu = W_\mu^3 \sin\theta_W + B_\mu \cos\theta_W \tag{1.3}$$

where θ_W is Weinberg angle, defined as:

$$\sin\theta_W = \frac{e}{g} \tag{1.4}$$

where e is the coupling constant of A_μ or the elementary charge, and g is the coupling constant of $\mathbf{W}_\mu$. The gauge particles quantized by those gauge fields are listed in Table 1.2; γ is from A_μ, $W^\pm$ is from $W_\mu^\pm$ and Z^0 is from Z_μ. The Brout-Englert-Higgs mechanism predicts the existence of a scalar boson, called Higgs boson (h).

1.1.1 Standard Model in LHC experiment

In last decades, many collider experiments have been conducted to verify the SM, and to search for the BSMs.

Figure 1.1 shows the observed and the prediction for the cross section of various physics processes. The data points are measurements by the LHC experiment, which is used in this thesis. Detail of the experiment will be described in next chapter. The theoretical prediction, given as gray band in the figure, is from 10^{-3} to 10^{11} pb. Since those processes have origin of proton-proton collision, higher yields from QCD activities are expected than the yields from the electroweak activities. Since particles generated from the QCD have colour, it decays to bunch of hadrons and constructs "jet" in the detector. As expected, jet processes have the next-to-highest yields as shown in the figure[*1]. Although the range of predicted cross section is wide, almost all experimental measurements are consistent with the theoretical predictions.

One of the remarkable experimental results in the LHC experiment is the discovery of the Higgs particle. After the discovery of tau neutrino in 2000, the Higgs particle was the last missing element in the SM. It was discovered at the ATLAS and the CMS experiment in 2012 [6, 7]. Later it was confirmed that the characteristic of the discovered particle is consistent with the SM prediction about the Higgs particle. The mass of the Higgs particle was measured as 124.97 ± 0.24 GeV [8]. The discovery of the Higgs particle completes the SM.

1.1.2 Hierarchy problem and dark mater

Although the SM gives predictions for most of the physics processes with high accuracy, which are verified by various experiments, there are some issues that cannot be explained by the SM. In this section, two such issues are introduced; the hierarchy problem and dark matter.

The hierarchy problem can be seen in the calculation of the Higgs mass. As described in the previous section, the Higgs mass is experimentally measured as 125 GeV. On the other hand, the

[*1] The highest process is the inelastic scattering of proton-proton collision.

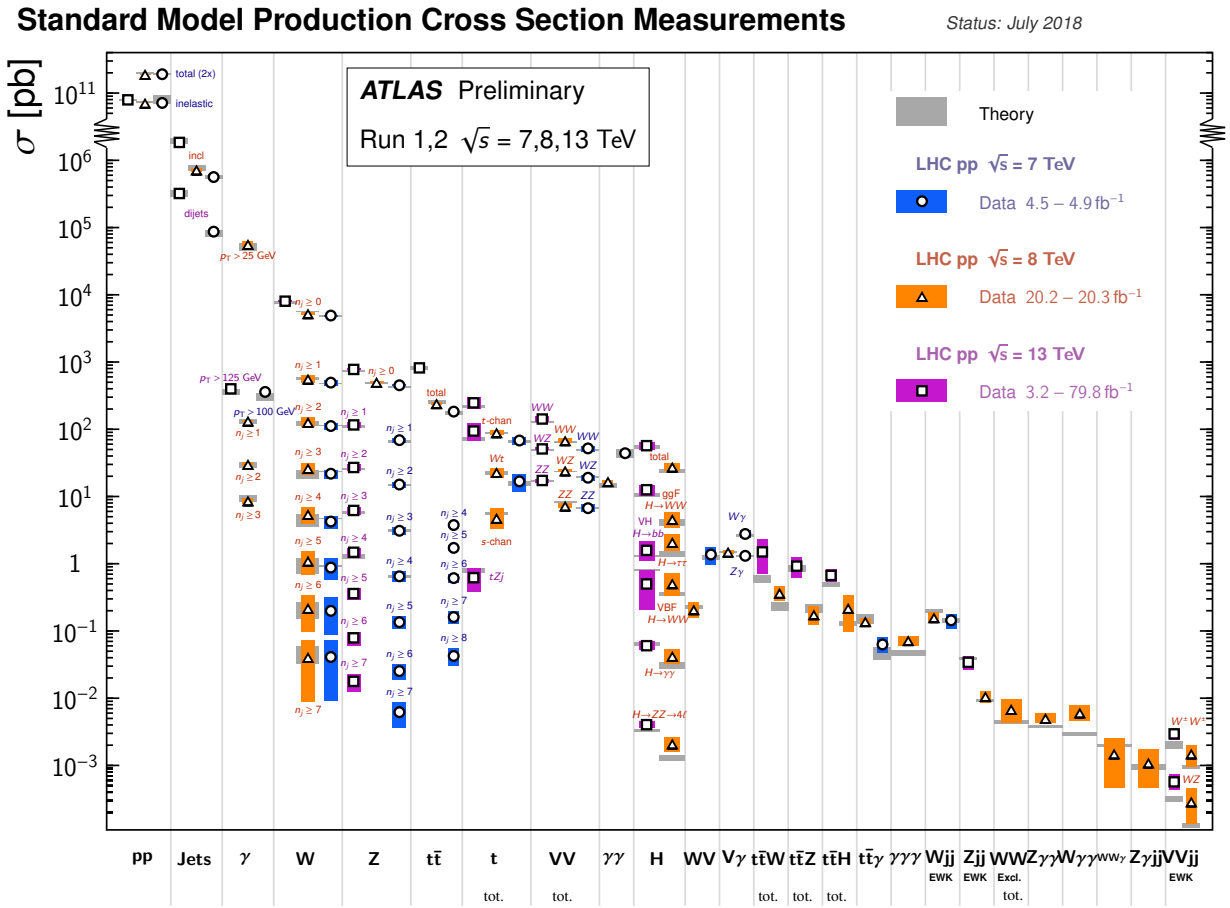

Figure1.1 Summary of several Standard Model total and fiducial production cross section measurements, corrected for leptonic branching fractions, compared to the corresponding theoretical expectations. All theoretical expectations were calculated at NLO or higher. The luminosity used for each measurement is indicated close to the data point. Some measurements have been extrapolated using branching ratios as predicted by the Standard Model for the Higgs boson. Uncertainties for the theoretical predictions are quoted from the original ATLAS papers. They were not always evaluated using the same prescriptions for PDFs and scales. The Wgamma and Zgamma theoretical cross-sections have non-perturbative corrections applied to the NNLO fixed order calculations (PRD 87, 112003 (2013)). Not all measurements are statistically significant yet. The figure is cited from [5]

mass can be calculated from the quantum field theory. The theoretical calculation explains the experimentally measured mass m_h^2 as:

$$m_h^2 = m_{h_0}^2 + \delta m_h^2 \tag{1.5}$$

where m_{h_0} is the Higgs bare mass and δm_h is the quantum correction. m_{h_0} is free parameter in the theory. However, the quantum correction is calculated as

$$\delta m_h = -\frac{|\lambda_f|^2}{8\pi^2}\Lambda^2 - \mathcal{O}(\log(\Lambda^2)) + \cdots \tag{1.6}$$

where λ_f is the Yukawa coupling of the fermion f and Λ is the cut-off scale parameter meaning upper limit of the energy scale that the SM is valid. If only the SM is considered, Λ is expected to be $\mathcal{O}(10^{19})$ GeV, which is the Planck scale. Since m_h is measured as 125 GeV, m_{h_0} is required to be

$\mathcal{O}(10^{19})$ GeV and two huge terms have to cancel out unnaturally to the level of $\mathcal{O}(10^2)$ GeV. This unnatural "tuning" is called hierarchy problem.

The other issue introduced in this section, dark matter, was obtained from the observation in the astrophysics. From the precise measurements by the Planck satellite [9], it is suggested that the SM particles can explain only 4.9% of energy of the whole universe. The rest is covered by dark matter, which is unknown to be massive particles, covering 26.8%, and dark energy, which is unknown energy accelerating the expansion of the universe, covering 68.3%. Since dark matter is not directly detected yet, the interaction between the SM particles and the dark matter must be very small.

The issues introduced above cannot be explained by the SM alone. In order to explain those, many extended models have been constructed, which are known as the Beyond Standard Model (BSM). One of the BSM is the Supersymmetry. It can explain both hierarchy and dark matter problems. It is explained in the next section.

1.2 Supersymmetry

1.2.1 Mechanism of Supersymmetry

The basic idea of SUperSYmmetry (SUSY) is to introduce a new symmetry between bosons and fermions[10]. SUSY assumes "supperpartner" for all the SM particles. The new particles are called SUSY particles. The SUSY particles are summarized in Table 1.3. As shown in the table, supperpartners of quark and lepton are called squark and slepton respectively. Supperpartners of bosons are called Gluino, Wino, Bino and Higgsino. Within a framework of the SM + SUSY, the operator transforming fermions and bosons are

$$Q\left|\text{Fermion}\right\rangle = \left|\text{Boson}\right\rangle, Q\left|\text{Boson}\right\rangle = \left|\text{Fermion}\right\rangle \tag{1.7}$$

and should not retain the symmetry.

The SUSY model can explain the hierarchy problem. The hierarchy problem is caused by the dominant quantum corrections of fermions. In SUSY model, all fermions have boson supperpartners which are supposed to have the same mass. And correction term of boson have opposite sign to the fermion correction and vice versa. Therefore, the correction terms are naturally cancelled and "tuning" is not needed anymore.

Because the SUSY particles are not discovered yet, the SUSY is broken in the our universe. However, even after the symmetry breaking, quantum corrections for higgs mass must be cancelled out naturally. In order to achieve such symmetry braaking, "soft" SUSY breaking is introduced as:

$$\mathcal{L} = \mathcal{L}_{\text{SUSY}} + \mathcal{L}_{\text{SUSY}} \tag{1.8}$$

where $\mathcal{L}_{\text{SUSY}}$ contains all of the gauge and Yukawa interactions and preserves SUSY invariance, and $\mathcal{L}_{\text{soft}}$ violates SUSY but contains only mass terms and coupling parameter with positive mass

Table1.3 SUSY particles

name	spin	corresponding SM particles
Squarks $(\tilde{u}, \tilde{c}, \tilde{t}, \tilde{d}, \tilde{s}, \tilde{b})$	0	Quarks (u, c, t, d, s, b)
Sleptons $(\tilde{e}, \tilde{\mu}, \tilde{\tau}, \tilde{\nu_e}, \tilde{\nu_\mu}, \tilde{\nu_\tau})$		Leptons $(e, \mu, \tau, \nu_e, \nu_\mu, \nu_\tau)$
Gluino $(\tilde{g})$	1/2	Gluon (g)
Wino $(\tilde{W})$		Weak boson (W, Z) and photon (γ)
Bino $(\tilde{B})$		
Higgsino $(\tilde{H})$	1/2	Higgs (h)

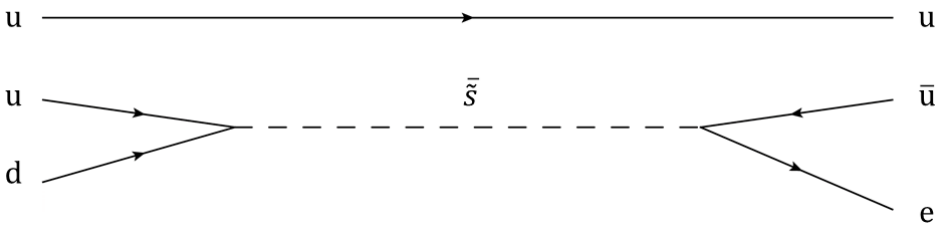

Figure1.2 Proton decay via SUSY particle ($\bar{\tilde{s}}$).

dimension, which are known as terms not to lead quadratic divergence even after symmetry breaking. Because of the $\mathcal{L}_{\text{soft}}$, supperpartners are expected to be heavier than the SM particles. Even after the symmetry breaking due to the $\mathcal{L}_{\text{soft}}$, there are no quadratic divergence shown in Equation 1.6.

The introduction of SUSY allow violations of baryon number (B) or lepton number (L). A famous process to violate the baryon number is the proton decay. With introduced SUSY particles, a proton may decay via a squark into a lepton and a meson, as shown in Figure 1.2. However, it is known that such violations are extremely small from severe experimental constraints [11]. In order to explain such observation, new symmetry, R-parity, is introduced. It is defined as

$$R = (-1)^{2S+3B-L} \tag{1.9}$$

where S is spin. The SM particles have a positive R-parity, and the SUSY particles have a negative R-parity. R-parity is expected to be conserved[*2]. Because of R-parity conservation, SUSY particles are expected to be generated by pair production and the Lightest SUSY Particle (LSP) cannot decay to SM particles. Since LSP is not discovered yet, it is expected to be neutral and not to have colour.

Among the SUSY particles shown in Table 1.3, Wino, Bino, and Higgsino are mixed. They are called electroweak gauginos. They are represented as mass eigenstates by $\tilde{\chi}_i^0 (i = 1, 2, 3, 4)$ (neutralino) for neutral particles and $\tilde{\chi}_i^{\pm} (i = 1, 2)$ (chargino) for charged particles. $\tilde{\chi}_1^0$ satisfies the expected conditions about the LSP described above.

Regarding dark matter, the LSP can be a good candidate. As described above, the LSP cannot decay to any other particle. And the expected interaction between LSP and the SM particles is only the weak interaction, which is extremely difficult for the direct detection. This expectation can explain the reason why dark matter has not been discovered yet. Those characteristics are ideal for the dark matter candidate.

The soft SUSY breaking term $\mathcal{L}_{\text{soft}}$ can be defined by 105 parameters. However, many of those parameters are strongly constrained by experimental observations such as neither CP-violation nor flavor changing neutral currents. By assuming first and second generation universality, free input parameters are only 19, which are:

- The ratio of the vacuum expectation value of the two higgs fields (1 parameter)
- The mass of the pseudoscalar higgs boson (1 parameter)
- The higgs-higgsino mass parameter (1 parameter)
- The bino, wino, and gluino mass parameters (3 parameters)
- The squarks and sleptons masses (10 parameters)
- The third generation trilinear couplings (3 parameters)

This model is called Phenomenological Minimal Supersymmetric Standard Model (pMSSM) [13]. The study described in this thesis is based on the pMSSM.

[*2] There are some models assuming R-parity violation. But from the fact that proton decay is not observed so far, there are upper limit on the R-parity violating couplings [12].

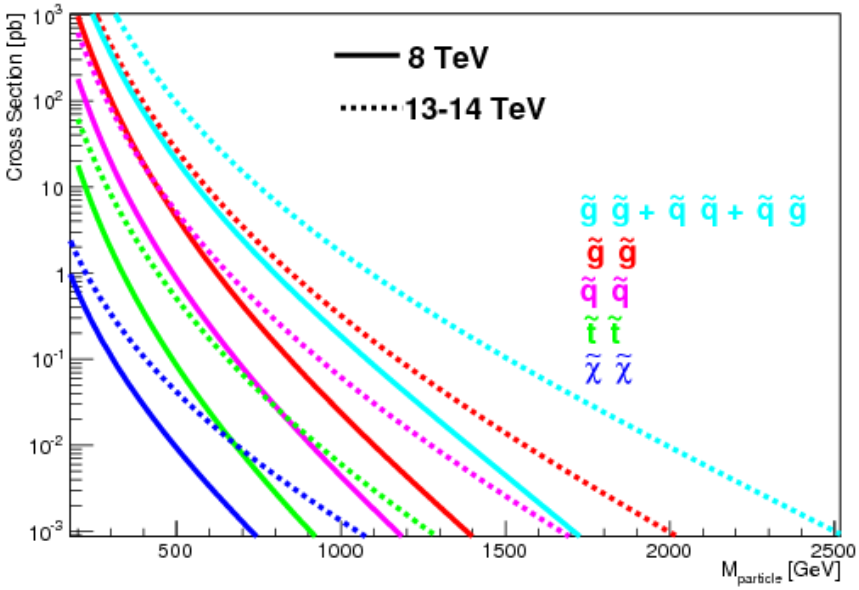

Figure1.3 Cross sections for SUSY particle production at $\sqrt{s} = 8$ TeV and 13、14 TeV. The figure is cited from [14]

1.2.2 SUSY searches in LHC experiment

In the LHC experiment, many types of SUSY searches have been performed. Because mass hierarchy of SUSY depends on the SUSY modeling parameters, many types of the pair production modes are candidates for the searches. Figure 1.3 shows the expected cross sections for SUSY particle pair production at the different center of mass energies in proton-proton collisions. As shown in the figure, gluino or squarks, which are generated by QCD interaction, have large cross sections. Therefore, if QCD production mode is accessible by experiment, it is expected to be observed in early stage of LHC experiment. However, as seen in Figure 1.4, even after the analysis using $\sim$ 20 fb^{-1} of 8 TeV data, experimental hints for the existence of SUSY particles have not been seen so far. This suggests that SUSY pair production may occur via QCD interaction but it is not accessible yet simply due to their high masses, or the production mode accessible by experiments is not QCD but electroweak interaction, such as the pair production of charginos and/or neutralinos. In this thesis, electroweak interaction is assumed as a production mode accessible by experiments, and we search for pair production of electroweak gauginos.

1.2.3 Electroweak gauginos

The search for pair production of electroweak gauginos is generally performed with the model so called "simplified" model. As described in Section 1.2.1, electroweak gauginos are expected to be mixed. However, in the simplified model, "pure" LSP and Next-to-Lightest SUSY Particle (NLSP) are assumed. In this thesis, LSP is assumed to be the bino, and NLSP is assumed to be the degenerated wino triplet. And the other supperpartners are assumed to be heavy and decoupled[*3].

The direct search for general neutral LSP has been performed as a general search for dark matter, such as [16]. However, such study is challenging because similar event kinematics can be seen in many SM process, and therefore large background contributions are expected. Hence, searches for direct

[*3] For the cross section calculation, all other supperpartners except for wino and bino are assumed to have 100 TeV mass. And mixing angles and trilinear couplings are assumed to be zero.

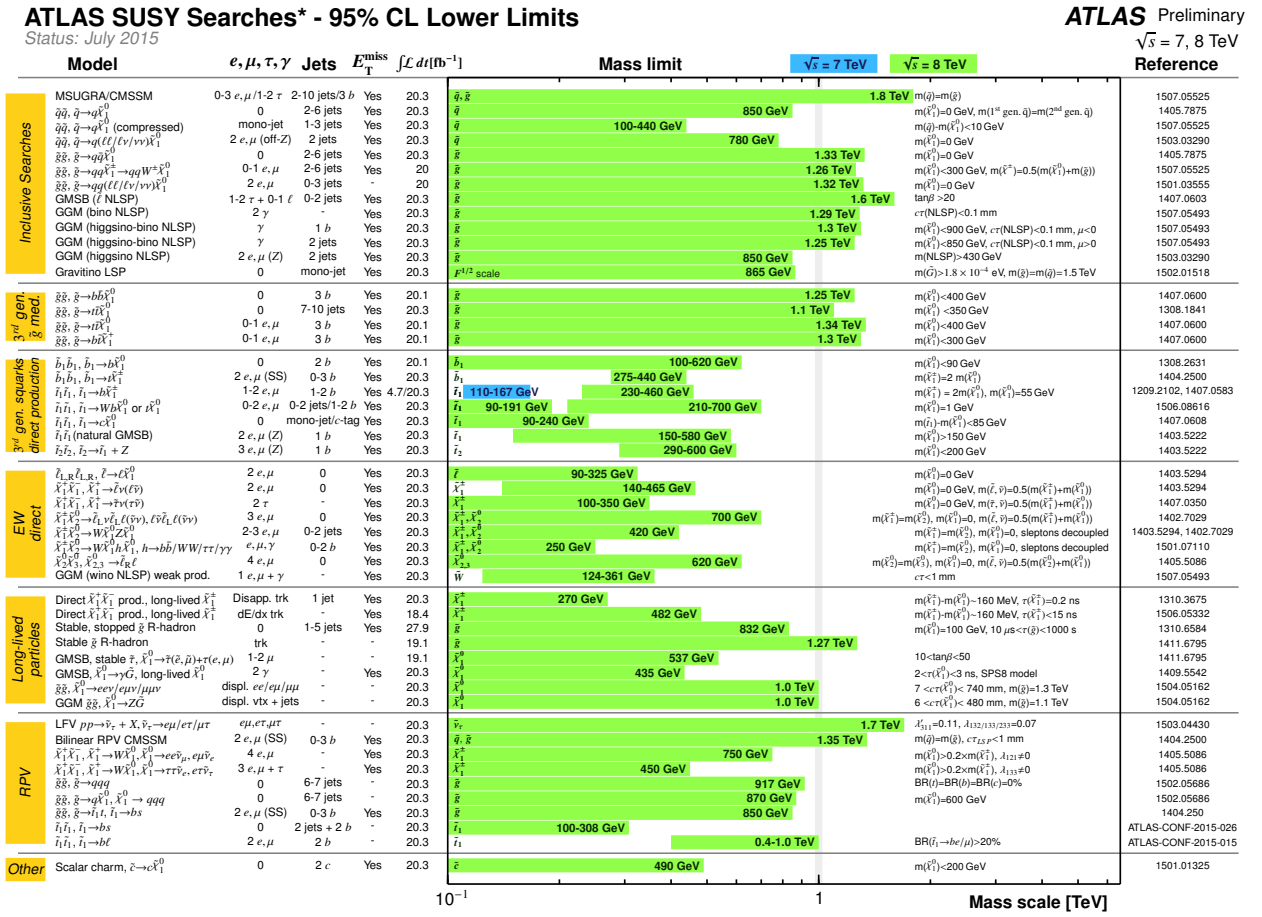

Figure1.4 Mass reach of ATLAS searches for Supersymmetry achieved at July 2015, before collecting collision data with $\sqrt{s} = 13$ TeV. The figure is cited from [15]

pair production of NLSPs, using event characteristics which are rare in SM process, are relatively more promising than searches for direct production of LSPs. As direct pair productions of wino like NLSP*4, two types of pair production can be expected; $\tilde{\chi}_1^{\pm}, \tilde{\chi}_2^0$ production or $\tilde{\chi}_1^+, \tilde{\chi}_1^-$ production*5 $\tilde{\chi}_1^{\pm}$ can decay to $\tilde{\chi}_1^0 + W^{\pm}$, and $\tilde{\chi}_2^0$ can decay to $\tilde{\chi}_1^0 + Z$ or $\tilde{\chi}_1^0 + h$. All of these combinations had been studied with 8 TeV data by the ATLAS experiment. The results are shown in Figure 1.5.

Because of small cross section of $\tilde{\chi}_1^+, \tilde{\chi}_1^-$ comparing to $\tilde{\chi}_1^{\pm}, \tilde{\chi}_2^0$ [17]*6, the exclusion reach of $\tilde{\chi}_1^+, \tilde{\chi}_1^-$ is smaller than the one for $\tilde{\chi}_1^{\pm}, \tilde{\chi}_2^0$. Comparing the results via WZ and via Wh, the analysis via WZ seems to be strong in excluding the model from the figure. However, this depends on the assumption of branching fraction of $\tilde{\chi}_1^{\pm}$. Both analyses with 8 TeV data via WZ [18] and via Wh [19] assume the branching fraction $\tilde{\chi}_2^0 \to \tilde{\chi}_1^0 + Z/h$ to be 100%. From the tree-level calculation with input of wino mass = 175 GeV and LSP mass = 0 GeV, $\mathrm{Br}(\tilde{\chi}_2^0 \to \tilde{\chi}_1^0 + h)$ is greater than $\mathrm{Br}(\tilde{\chi}_2^0 \to \tilde{\chi}_1^0 + Z)$, if Higgsino mass is assumed to be much larger than the masses of other electroweak gauginos [20]. This suggests that analysis via Wh can be powerful to search for electroweak gauginos pair production. Therefore, in this thesis, target physics process is determined to be decay via Wh. As having been done in the analysis with 8 TeV data, 100% branching ratios to W and h are assumed to simplify

*4 Pair productions of wino like NLSP and bino like LSP are strongly suppressed because direct coupling between them is prohibited.

*5 $\tilde{\chi}_2^0, \tilde{\chi}_2^0$ production is also a possible mode. However, such process is produced only from neutral weak currents, which is quite small, meaning production cross section is also quite small.

*6 This is mainly due to the proton PDF.

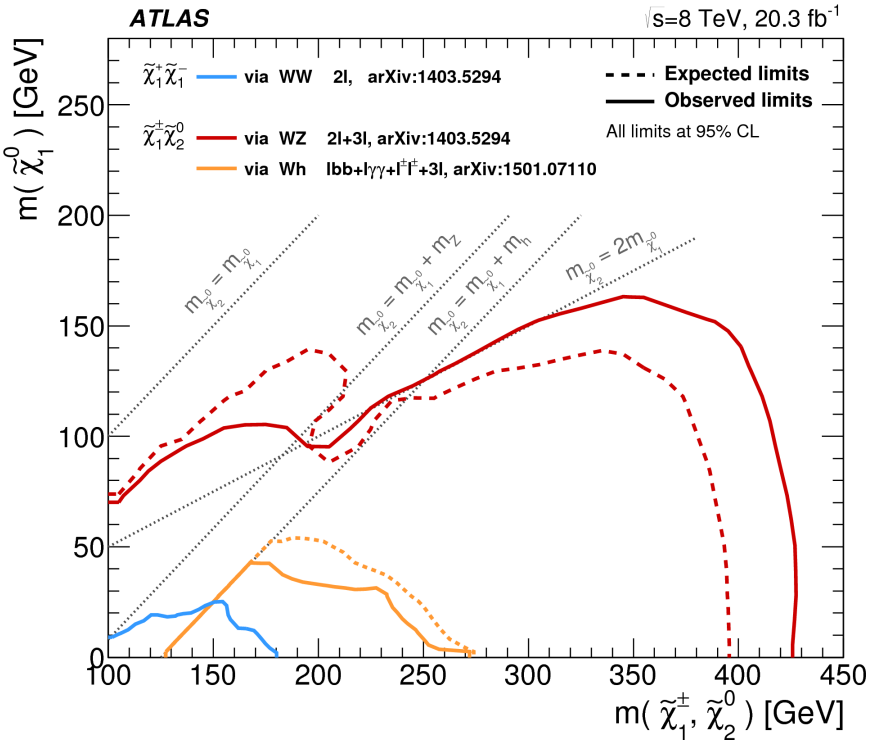

Figure1.5 The 95% CL exclusion limits on $\tilde{\chi}_1^+ + \tilde{\chi}_1^-$ and $\tilde{\chi}_1^\pm + \tilde{\chi}_2^0$ production with SM-boson-mediated decays, as a function of the $\tilde{\chi}_1^\pm$, $\tilde{\chi}_2^0$ and $\tilde{\chi}_1^0$ masses. The production cross-section is for pure wino $\tilde{\chi}_1^+\tilde{\chi}_1^-$ and $\tilde{\chi}_1^\pm\tilde{\chi}_2^0$. The plot is cited from [21]

the analysis.

There are further categorization using decay mode of W and h. Figure 1.6 shows the results of electroweak gaugino search decaying via W and h using 8 TeV data. As showing in the figure, there were four channels;

- 3ℓ channel: assuming $W \to \ell\nu$ and $h \to \ell\ell$[*7]
- $\ell^\pm\ell^\pm$ channel: assuming $W \to \ell\nu$ and $h \to \ell\nu qq$[*8]
- $\ell\gamma\gamma$ channel: assuming $W \to \ell\nu$ and $h \to \gamma\gamma$
- ℓbb channel: assuming $W \to \ell\nu$ and $h \to bb$

In this thesis, the third channel, $W(\to \ell\nu)h(\to \gamma\gamma)$ process is chosen as a target, which is called "diphoton" channel. Figure 1.7 shows the diagram of this channel. As shown in Figure 1.6, the diphoton channel is expected to have high exclusion performance because of following reasons. One of the big advantage of this channel is the characteristic of diphoton mass. Since diphoton are decay products from the Higgs, reconstructed mass of those two photons is expected to have keen peak around the Higgs mass. Such characteristic cannot be seen for most of the backgrounds. Therefore, by just limiting diphoton mass close to the Higgs mass, most of the backgrounds can be suppressed. In the case of 3ℓ channel, since h decays to two leptons and missing object, background suppression using di-lepton mass is not promising. This is further discussed in Section 3.2.1.

The lack of the expected QCD activities is also a strong motivation of this channel. Since the collected data is from proton-proton collisions, large QCD background are expected. Therefore, the channels assuming objects generated by QCD in the final state, such as ℓbb channel and $\ell^\pm\ell^\pm$

[*7] It is assuming to decay via $h \to WW/ZZ \to \ell\ell\nu\nu$ or $h \to \tau\tau \to \ell\ell$+missing.

[*8] It is assumed to decay via $h \to WW$. And signals decay via $h \to ZZ$ or $\tau\tau$ also have contribution if there are misidentified objects.

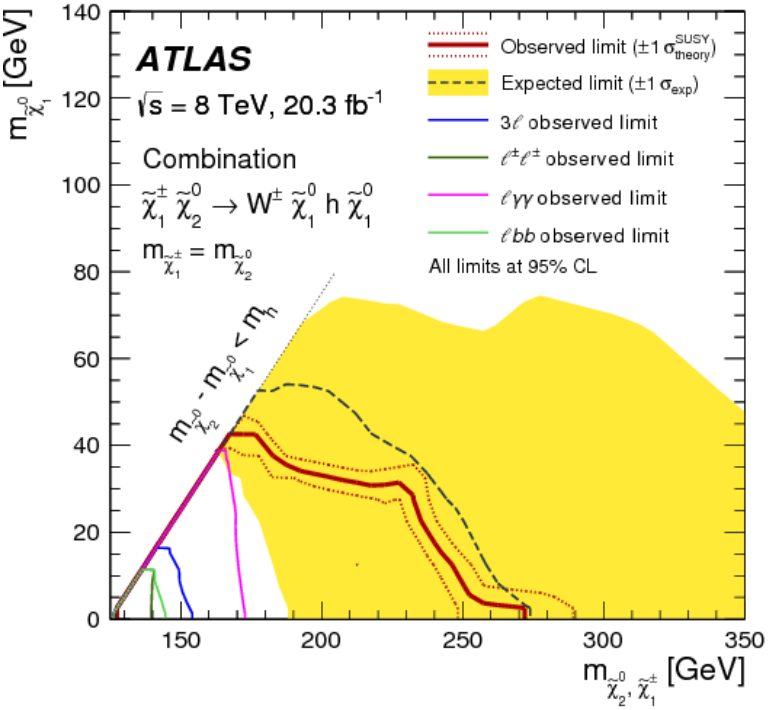

Figure1.6 Observed (solid line) and expected (dashed line) 95% CL exclusion regions in the mass plane of $m_{\tilde{\chi}_1^0}$ vs. $m_{\tilde{\chi}_1^\pm,\tilde{\chi}_2^0}$ in the simplified model, using 8 TeV data. The dotted lines around the observed limit represent the results obtained when changing the nominal signal cross section up or down by the $\pm 1\sigma_{\text{theory}}^{\text{SUSY}}$ theoretical uncertainty. The solid band around the expected limit shows the $\pm 1\sigma_{\text{exp}}$ uncertainty band where all uncertainties, except those on the signal cross sections, are considered. The figure is cited from [19]

channel, are expected to suffer huge QCD background. In addition, because estimation of the QCD backgrounds have large uncertainties, accuracy of the background estimation is limited.

Diphoton channel has advantages as described above. However, the diphoton channel has a difficulty as well. The major one is the expected low statistics. Since $\text{Br}(h \to \gamma\gamma)$ is only 0.23%, the yields of signal is expected to be small compared to the other channels. Therefore, during the development of the analysis, more weights are put on keeping acceptance of the signal yields, and the sophisticated treatments on the small statistics in the signal region.

1.3 Author's contributions

As described above, this thesis presents the analysis on searching for a direct pair production of charginos and neutralinos using decay channel $\tilde{\chi}_2^0 \to \tilde{\chi}_1^0 h \to \tilde{\chi}_1^0 \gamma\gamma$ and $\tilde{\chi}_1^\pm \to \tilde{\chi}_1^0 W \to \tilde{\chi}_1^0 \ell\nu$ with data collected with the ATLAS detector. The motivation for this search is described in this chapter.

In Chapter 2, experimental setup is described. The author contributed to the data acquisition system for the pixel detector, described in Section 2.2.1. Because of the update of center-of-mass energy, which is described in Section 2.1.2, it was expected that the bandwidth of some part of the data acquisition system of the pixel detector is going to reach the limit within the experiment from 2016. To avoid such situation, the data acquisition system for the outer most layer of the pixel detector was fully replaced at the beginning of 2016 [22]. The author developed the firmware for the new data acquisition system.

In Chapter 3, data and simulation samples used in the analysis are introduced. Those samples are processed and physics objects are reconstructed as described in Chapter 4. The author processed the

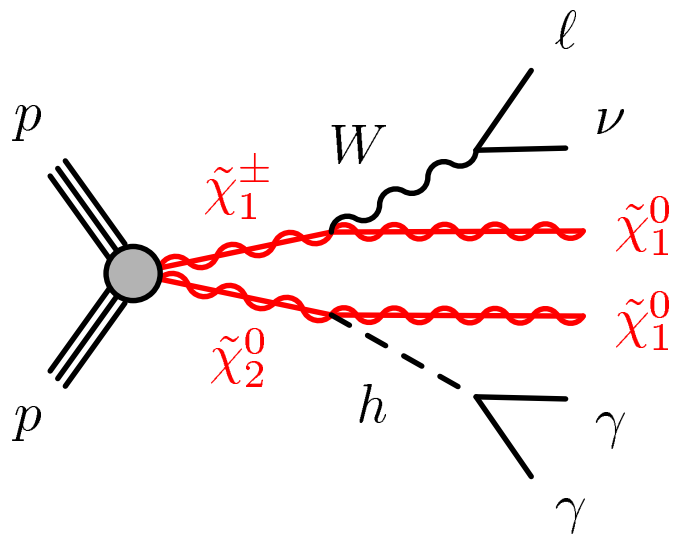

Figure1.7 Feynman diagram of diphoton channel.

signal samples and the updated background samples as described in Section 3.2.1. The author also verified the "isolation" definition for photon and electron, which is described in Section 4.2.1. As described in Equation 4.2, isolation criteria depend on the expected energy of the photon candidate. The author confirmed that this expected energy is close enough to the truth photon or electron energy, and there are no deviation which may be the source of bias of the selection.

From Chapter 5, analysis procedure and study performed for this search are discussed. The author contributed as the main analyzer for this search. All the figures used in those chapters are produced by the author. In Chapter 5, event selection criteria are described. As described in that chapter, the criteria optimization was started from the criteria used in previous work. All the criteria are confirmed and tuned as necessary by the author. In Chapter 6, procedure for the evaluation of backgrounds are described and verified. All the evaluation and the study described in this chapter was performed by the author. In Chapter 7, optimization of the signal region definition to improve significance is described. The topic described in this chapter is a major improvement from the previous work. The author performed the study described in this chapter and proposed optimized signal region. In Chapter 8, uncertainties and their effects are explained. The author evaluated those and found that the systematical effect is small enough compared to the statistical effect. In Chapter 9, observed events are statistically evaluated. All the interpretations have been performed by the author. In Chapter 10, all the studies described in this thesis are summarized.

Chapter 2

Large Hadron Collider and The ATLAS detector

The Large Hadron Collider (LHC) is the largest circular hadron collider in the world. The ATLAS detector is one of the multiple purpose detectors for the LHC. In this chapter, the experimental setup is described. The LHC is overviewed in Section 2.1, and the ATLAS detector is overviewed in Section 2.2.

2.1 LHC

The Large Hadron Collider (LHC) is a circular collider, which is made of two rings of superconducting hadron accelerators, constructed at the European Organization for Nuclear Research (Conseil Européen pour le Recherche Nucléaire, CERN). It is designed to collide proton beams at a total center-of-mass energy $\sqrt{s} = 14$ TeV. The construction was started by replacing the experimental setup for the Large Electron Positron collider (LEP) while reusing the tunnel for the accelerator located underground from 45 m to 170 m, around the border of Switzerland and France. Around the tunnel, of which length is 26.7 km, several detectors were constructed for the measurement of the collisions.

The proton beam for the collisions is accelerated by several types of the injectors step by step before the injection into the LHC. In Section 2.1.1, those LHC injector chains are overviewed. Then, the design of the LHC is explained in Section 2.1.2.

2.1.1 LHC injector chain

Figure 2.1 shows the full chain of the LHC injector. The chain is constructed as following order: Linear accelerator 2, Proton Synchrotron Booster, Proton Synchrotron and Super Proton Synchrotron before the LHC.

The Linear accelerator 2 (Linac2) generates proton sources from hydrogen gas by passing through them into an electric field to remove their electrons and injects them into the Proton Synchrotron Booster (PSB) as 50 MeV beams. The PSB, which consists of four super-imposed synchrotron rings distributed along 157 m length of circumference, accelerates the beam to 1.4 GeV and injects them into the Proton Synchrotron (PS). The PS, which is a synchrotron made by 277 conventional electromagnets distributed along 628 m length of circumference, accelerates the beam to 25 GeV, and injects them into the Supper Proton Synchrotron (SPS). The SPS is the last accelerator before the injection to LHC. It contains 1425 magnets distributed along 6.9115 km length of circumference and accelerates beam up to 450 GeV.

The proton beam in the LHC is accelerated in a form of bunches. It is designed so that 2808 bunches are filled in 3564 bunch places in LHC beam line with 25 nsec bunch spacing. The proton beam injected with 450 GeV is accelerated up to 7 TeV. More detail about the LHC is described in the next section.

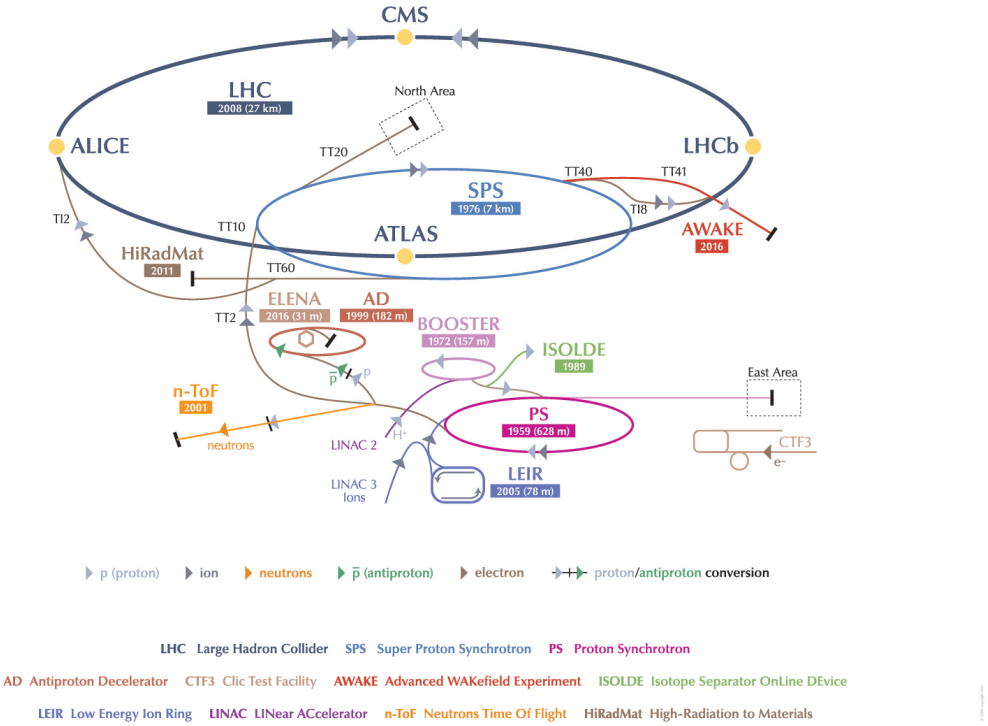

Figure2.1 The accelerator comples at CERN. The figure is cited from [23].

2.1.2 LHC design

The LHC is developed for the search for new physics. Event yield of new physics is a key of the experiment. The expected number of events per second generated in LHC collisions is given by:

$$N_{\text{event}} = L\sigma_{\text{event}} \tag{2.1}$$

where σ_{event} is the cross section for the target event, and L is the machine luminosity. The machine luminosity can be written for a Gaussian beam distribution as:

$$L = \frac{N_b^2 n_b f_{\text{rev}} \gamma_r}{4\pi\epsilon_n \beta^*} F \tag{2.2}$$

where N_b is the number of particles per bunch, n_b is the number of bunches per beam, f_{rev} is the revolution frequency, γ_r is the relativistic gamma factor, ϵ_n is the normalized transverse beam emittance, β^* is the beta function at the collision point, and F is the geometric luminosity reduction factor due to the crossing angle at the interaction point:

$$F = \left(1 + \left(\frac{\theta_c \sigma_z}{2\sigma^*}\right)^2\right)^{-1/2} \tag{2.3}$$

θ_c is the full crossing angle at the interaction point, σ_z is the RMS bunch length, and σ^* is the transverse RMS beam size at the interaction point, under the assumption of $\sigma_z \ll \beta^*$ [24]. The

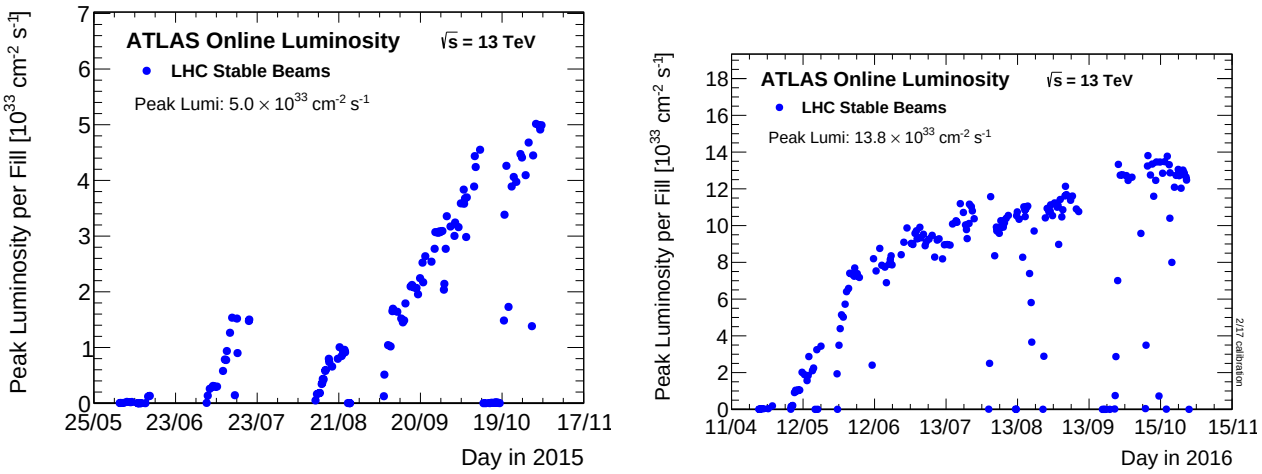

Figure2.2 Peak luminosity at ATLAS as a function of time

design values of those parameters are summarized in Table 2.1 with actual operation values shown in the right columns. With design parameters, L is expected to achieve 10^{34} cm^{2}s^{-1}.

Until 2012, the LHC was operated with 3.5 and 4 TeV proton beam. After that operation, there were two years of long shutdown to upgrade beam energy to 6.5 TeV. Then, finally from 2015, first operation with 6.5 TeV proton beam started. The experiment performed until 2012 is called Run 1, and experiment performed from 2015 is called Run 2. This analysis is using the data collected from 2015 to 2016.

Figure 2.2 shows the peak luminosity within those periods. At the beginning of the operation in 2016, it was found that there were unexpected objects in the beam pipe. Due to those objects, observed peak luminosity in early period of 2015 was lower than the design value. The peak luminosity increased mainly due to reduced full crossing angle θ_c after September 2015. In 2016, the peak luminosity further increased mainly due to reduced β^*. With those setups, integrated luminosity achieved 4.2 fb^{-1} in 2015 and 38.5 fb^{-1} in 2016.

Table2.1 Design and Operational parameters of LHC. Interaction point is assumed to be at the ATLAS detector. In September 2015, the full crossing angle was reduced from 370 μm to 280 μm. In later 2016, the beta function was reduced from 40 cm to 33 cm.

Parameters	Design	2012	2015	2016
Beam energy [TeV]	7	4	6.5	6.5
Bunch spacing [nsec]	25	50	25	25
Peak luminosity L [10^{34} cm^{2}s^{-1}]	1	0.75	1.4	1.7
Number of particles per bunch N_b [10^{11} per bunch]	1.15	1.65	1.1	1.2
Number of bunches per beam n_b	2808	1374	2220	2556
Revolution frequency $f_{\rm rev}$			11.2 kHz	
Normalized transverse beam emittance ϵ_n [μm]	3.75	2.5	2.2	2.2
Beta function at the ATLAS β^* [cm]	55	60	40	40 $\rightarrow$ 33
Full crossing angle at the ATLAS θ_c [μrad]	285	290	370 $\rightarrow$ 280	300
RMS bunch length at the ATLAS σ_z [cm]	7.55			
Transverse RMS beam size at the ATLAS σ^* [μm]	1.67			

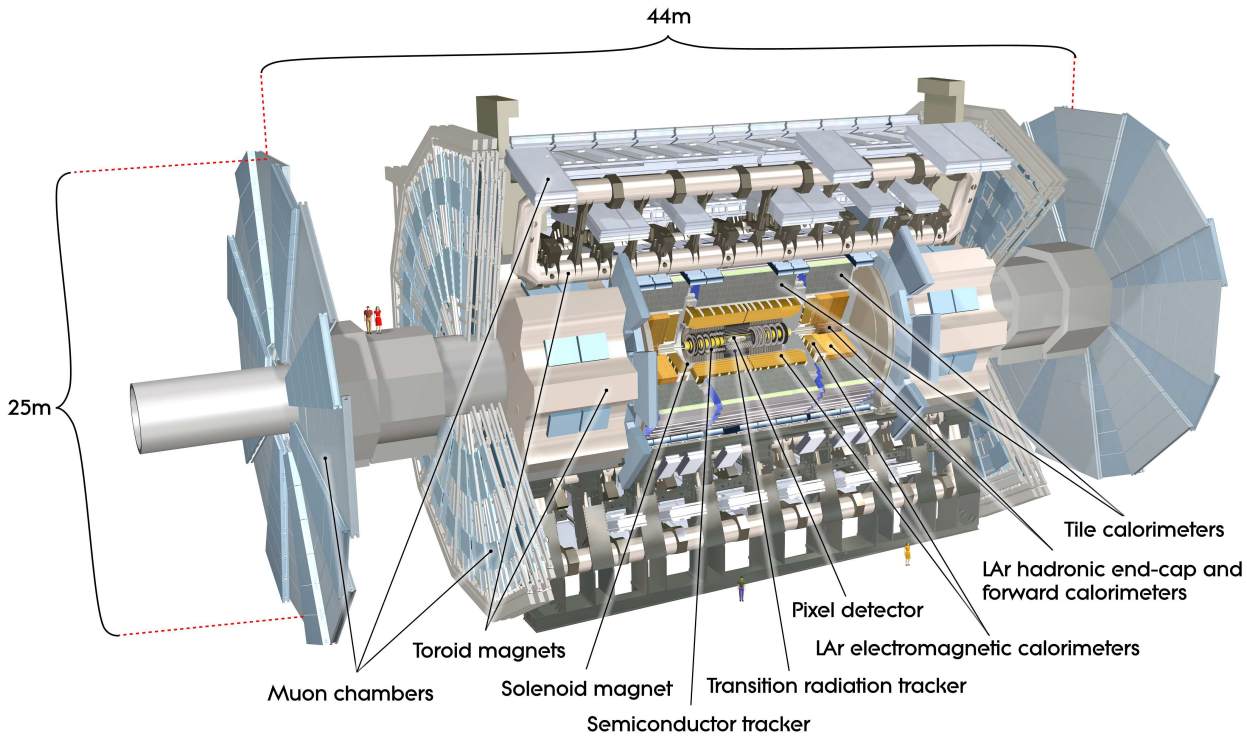

Figure2.3 Cut-away view of the ATLAS detector. The dimensions of the detector are 25 m in height and 44 m in length. The overall weight of the detector is approximately 7000 tonnes. The figure is cited from [25].

2.2 ATLAS detector

There are four detectors at LHC. Two general purpose detectors are the ATLAS and the CMS. One of the other detectors is LHCb, which is for the studies of b-physics. The last one is ALICE detector too, which is for heavy-ion collision experiments. In this section, the ATLAS detector, which is used in this analysis, is described.

The ATLAS, which stands for A Troidal LHC ApparatuS, is a general purpose detector for proton-proton collisions. Figure 2.3 shows the cut-away view of the ATLAS detector. As shown in the figure, its height is 25 m and its length is 44 m. It consists of following sub-detector systems from inner side:

- Inner Detector: The tracking system, described in Section 2.2.1. It consists of the pixel detector, the semiconductor tracker and the transition radiation tracker.
- Calorimeter: The detector to measure particle energy, described in Section 2.2.2. It consists of the electromagnetic calorimeter and the hadron calorimeter.
- Muon spectrometer: The subsystem for muons, which are particles that penetrate the calorimeter. It is described in Section 2.2.3. It consists of the thin gap chambers, resistive plate chambers, monitored drift chambers and cathode strip chambers.

The detector is constructed so that the center of the detector is located at the LHC collision point. Due to its shape shown in Figure 2.3, a cylindrical coordinate system is nominally used in the ATLAS experiment, while the beam direction defines the z-axis and x-y plane is transverse to the beam direction. The angle around z axis is measured by ϕ, and the polar angle θ from the beam axis is often interpreted to the pseudorapidity $\eta = -\ln[\tan(\theta/2)]$. The distance ΔR in the

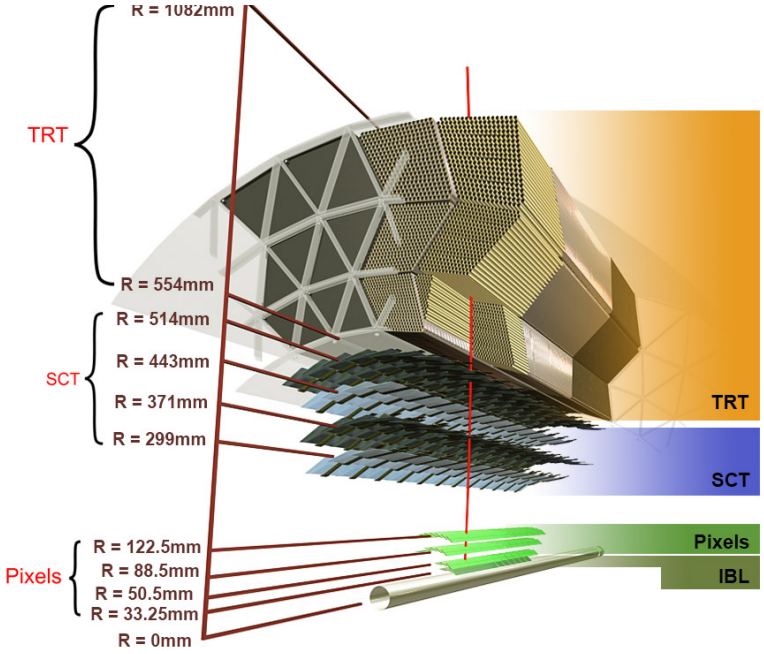

Figure2.4 Schematic x-y coross section view of a detailed layout of the Inner Detector (ID), including the new Insertable B-Layer (IBL). The figure is cited from [26]

pseudorapidity-azimuthal angle space, which is defined as $\sqrt{\Delta\eta^2 + \Delta\phi^2}$, is also often used. The region where the detector constructed in parallel to z-axis, is called "barrel" region, and the region where the detector constructed in x-y plane, is called "end-cap" region.

The detector has two magnet systems: a thin superconducting solenoid magnet surrounding the inner detector, and three large surrounding toroids arranged with an eight-fold azimuthal symmetry around the calorimeters. The magnet surrounding the inner detector provides 2 T solenoidal field to the tracking volume. Due to the field, momentum of charged particles in x-y plane, called transverse momentum p_T, can be measured by their tracks. In order to measure transverse momentum in high resolution, the resolution in ϕ direction is more important than that in η direction.

2.2.1 Inner Detector

Figure 2.4 shows the schematic x-y cross section view of the Inner Detector (ID). Figure 2.5 shows the r-z cross section view of it. As shown in the figures, the ID is made of the Pixel, the SemiConductor Tracker (SCT) and the Transition Radiation Tracker (TRT). Each sub-detector is described below.

Pixel detector

The pixel detector is installed in the inner most layer close to the beam line. The sensors of the pixel detector are made of n-type wafers with readout pixels on the n^+-implanted side of the detector. It has four barrel layers, covering $33.5 < r < 122.5$ mm and $|z| < 400.5$ mm, and three end-cap layers, covering $88.8 < r < 149.6$ mm and $495.0 < |z| < 650$ mm. The inner most barrel layer, which is called IBL, was installed after the run in 2012. The typical pixel size of the IBL is 50 μm (r-ϕ) $\times$ 250 μm (z), while that of the other pixel layers is 50 μm (r-ϕ)$\times$ 400 μm (z)

Figure 2.6 shows the typical structure of the pixel "module", which is an unit of the pixel detector. The module is made of the sensor containing 46080 readable channels in 63.4×24.4 mm^2, connected to 16 of the read-out Front End (FE) chips which detect analog signal from the sensor and digitize it for read-out, and the specific flex which is shown in the top of the figure. The flex contains Module

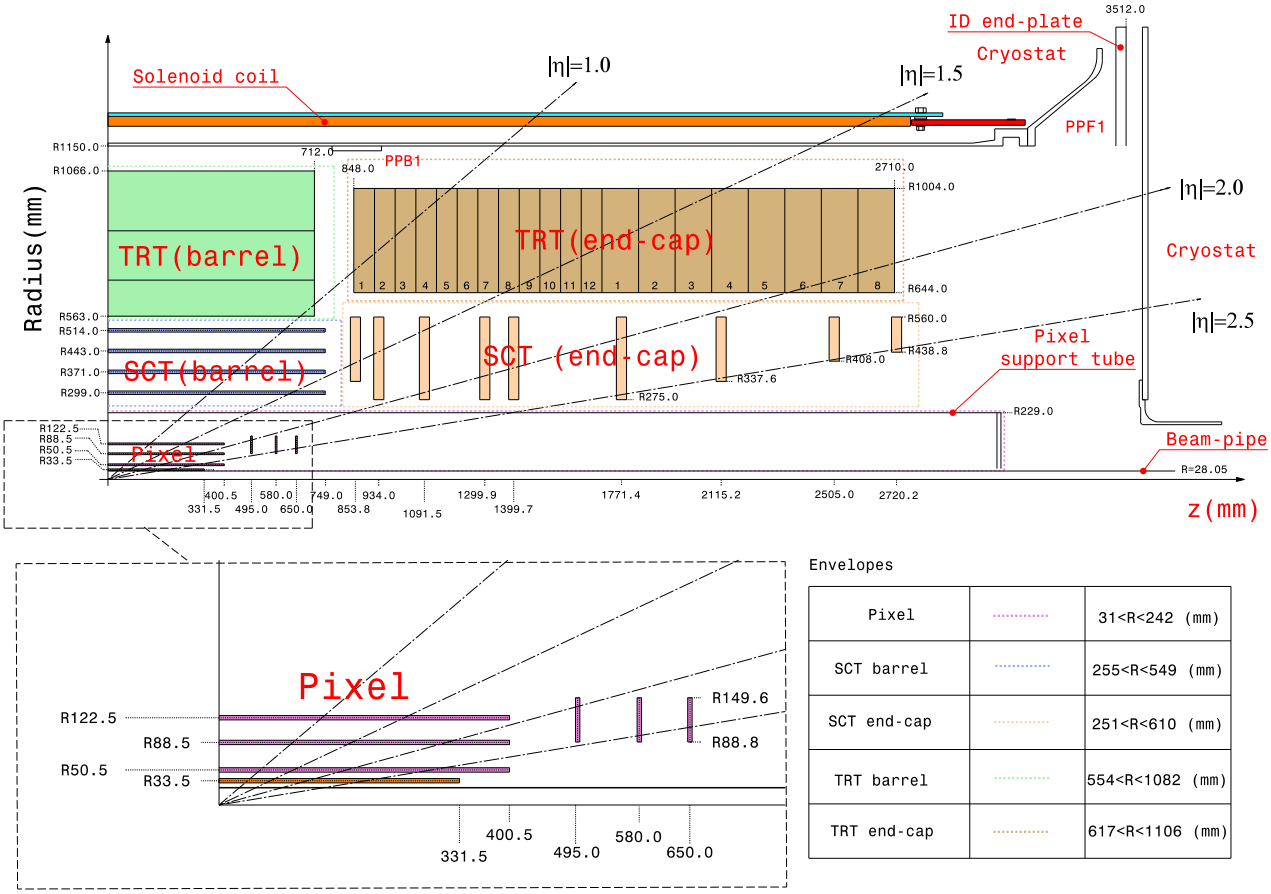

Figure2.5 The r-z cross section view of the layout of a quadrant of the ATLAS inner detector for Run 2. The figure is cited from [27]. The top panel shows the whole inner detector, whereas the bottom-left panel shows a magnified view of the pixel detector region. Compared to Run 1, the IBL (shown in orange in the bottom-left panel) and its services, together with the new beam pipe, were added.

Control Chip (MCC), which is controlling 16 of FEs, NTC thermistors for the temperature control and High-Voltage (HV) elements to supply HV to the sensor. The flex is connected to readout cabling via the connector on the "pigtail" shown as yellow plane in the figure.

In case of the IBL, FE has a role of MCC. Only two FEs are used to readout whole sensors in a module, while number of channels per module is 53760.

The pixel detector contains over 92 million pixels in total. For the barrel pixel layer, individual layer resolution of 10 μm in the ϕ direction and 115 μm in z direction are achieved.

Semiconductor Tracker

The SemiConductor Tracker (SCT) is the second inner most tracker, next to the pixel detector. The sensors of the SCT is single-sided p-in-n silicon strip sensor in 80 μm pitch. Since one SCT sensor has high resolution only in one direction, two sensors are glued back-to-back with a 40 mrad rotation around the geometrical center of the sensors. Each side of the sensor has 768 readable strips of which length is 6 cm. Owing to this angle, the module achieves resolution of 580 μm in the z direction, while 17 μm in ϕ direction is achieved. Although the resolution in z direction is worse than that of the pixel sensor, this concept can reduce readout channel significantly, as 6×12.6 cm space is covered by 768×2 readout strips while for Pixels 46080 readout channels are needed to cover 63.4×24.4 mm^2. Therefore, the inner-most region, where it is requested to measure tracks in high resolution, is covered by the pixel detector, and outer region, which has large surface area

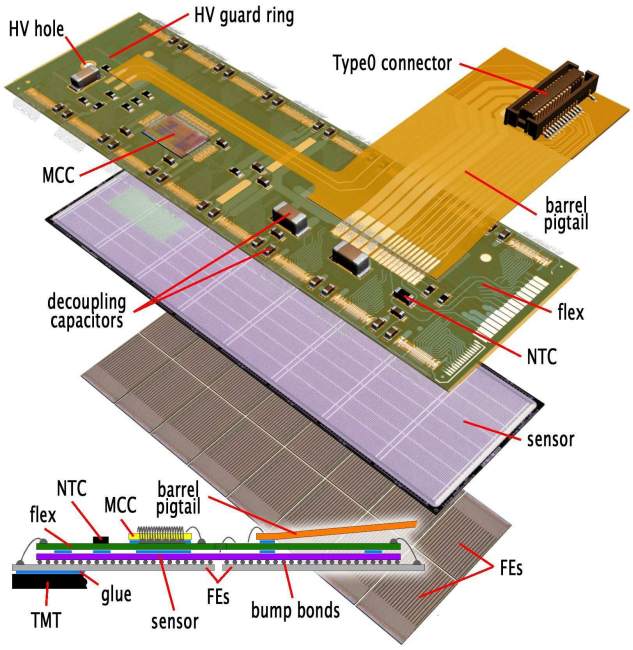

Figure2.6 Schematic view of a barrel pixel module illustrating the major pixel hybrid and sensor elements, including the MCC (module-control chip), the front-end (FE) chips, the NTC thermistors, the high-voltage (HV) elements and the Type0 signal connector. On the bottom of the module, there is a Thermal Management Tile (TMT). The figure is cited from [25].

needed to be covered, is covered by the SCT. There are 15912 strips for the barrel region.

Figure 2.7 shows the typical structure of the SCT "module", which is an unit of the SCT detector. The module is made of the two glued sensors, connected to 6 of the read-out Front End (FE) chips which are mounted on the hybrid assembly. The module is constructed on the baseboad made by thermal pyrolytic graphite (TPG), which has high conductivity providing a thermal path between the coolant and the sensors. The board has beryllia facings which are interfaced to the cooling system.

The SCT has four barrel layers, covering $299.0 < r < 514.0$ mm and $|z| < 749.0$ mm, and nine end-cap layers, covering $275.0 < r < 560.2$ mm and $853.8 < |z| < 2720.2$ mm. The detail geometry is shown in Figure 2.5.

Transition Radiation Tracker

The Transition Radiation Tracker (TRT) is the tracker located in the outer-most layer of the ID. The sensors of the TRT is polyimide drift straw tubes with a diameter of 4 mm, with the tungsten wire with diameter of 31 μm plated with 0.5–0.7 μm gold, supported at the end of the straw by an end-plug. The straws were cut to 144 cm for the barrel and 37 cm for the end-caps, and filled by the gas mixture with 5–10 mbar over-pressure. The design value of the gas mixture is 70% Xe, 27% CO_2 and 3% O_2, which achieves 2.5×10^4 gain with 1530 V. The position resolution of this sensor in $r - \phi$ plane is 120 μm in the barrel region. The tubes are installed in parallel to the beam line in the barrel region, and in parallel to the r direction in the end-cap region.

The TRT has three types of the modules in barrel, covering $563.0 < r < 1066.0$ mm and $|z| < 712.0$ mm, and two types of module in the end-caps, covering $644.0 < r < 1004.0$ mm and $848.0 < |z| < 2710.0$ mm. Each module layer has several layers of straws. The structure is designed so that all charged tracks with $p_{\mathrm{T}} > 5$ GeV in $|\eta| < 2.0$ must pass through at least 36 straws except in the barrel-end-cap transition region, which is $0.8 < |\eta| < 1.0$. Even in the barrel-end-cap transition region, charged particles pass at least 22 straws.

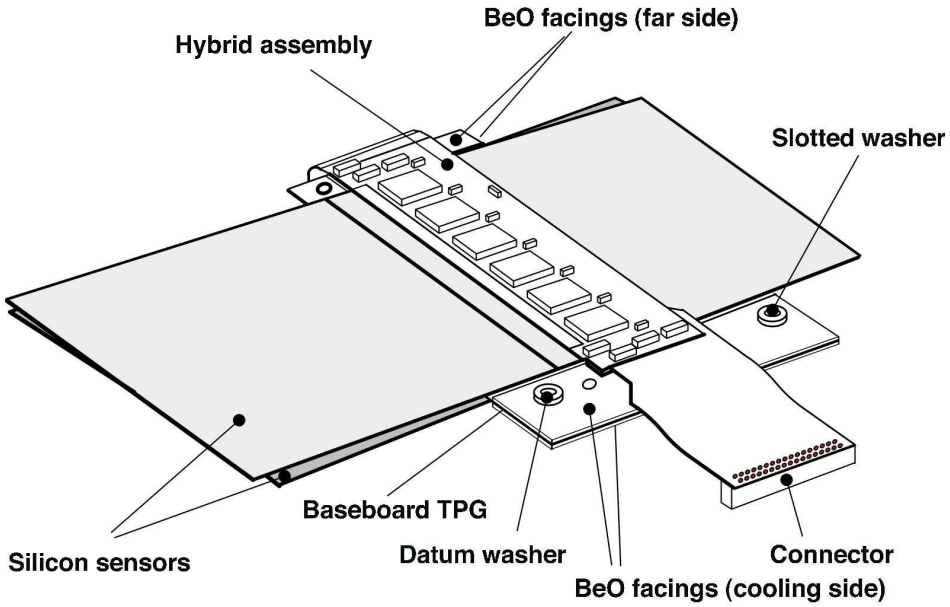

Figure2.7 Drawing of a barrel module, showing its components. The thermal pyrolytic graphite (TPG) base-board provides a high thermal conductivity path between the coolant and the sensors. The figure is cited from [25].

2.2.2 Calorimeter

Figure 2.8 shows the cut-away view of the ATLAS calorimeter system. As shown in the figure, the calorimeter system is made of the LAr electromagnetic calorimeter and three types of hadronic calorimeters, the tile calorimeter, the LAr hadronic end-cap calorimeter and the LAr forward calorimeter.

Those detectors were designed to provide containment for electromagnetic and hadronic showers. Therefore, radiation length (X_0) and interaction length (λ) are important parameters for the calorimeter. In the calorimeter, energy is measured using energy deposits from showers. In order to generate showers efficiently, several types of absorbers are used in the ATLAS detector, as explained in the following sections. The electromagnetic calorimeter has thickness $> 22X_0$in the barrel, and thickness $> 24X_0$in the end-caps. The hadronic calorimeter has thickness $> 9.7\lambda$ in the barrel and thickness $> 10\lambda$ in the end-caps.

Further detail about each sub-detector is described below.

Electromagnetic calorimeter

Figure 2.9 shows a sketch of a part of the ElectroMagnetic (EM) calorimeter in the ATLAS detector. This type of the EM calorimeter covers $|\eta| < 1.475$. It consists of accordion shape lead absorbers and liquid argon (LAr) as the active detector medium. The shape of the absorbers is chosen to make several active layers in depth.

The first layer has strip cells to distinguish two collimated photons decayed from π^0 and photons form collisions.The second layer is the main detector to measure the energy. The last layer is to collect energy leaking from the second layer.

The end-cap region is covered by two wheels of LAr ElectroMagnetic End-cap Calorimeter (EMEC); inner one covering $1.375 < |\eta| < 2.5$ and the other covering $2.5 < |\eta| < 3.2$. Those calorimeters have same structure with the EM calorimeter. In front of the detector described above, there is detector called PreSamplers (PS), which has only 11 mm depth of active layer to measure the energy lost in front of the calorimeters, covering $|\eta| < 1.8$.

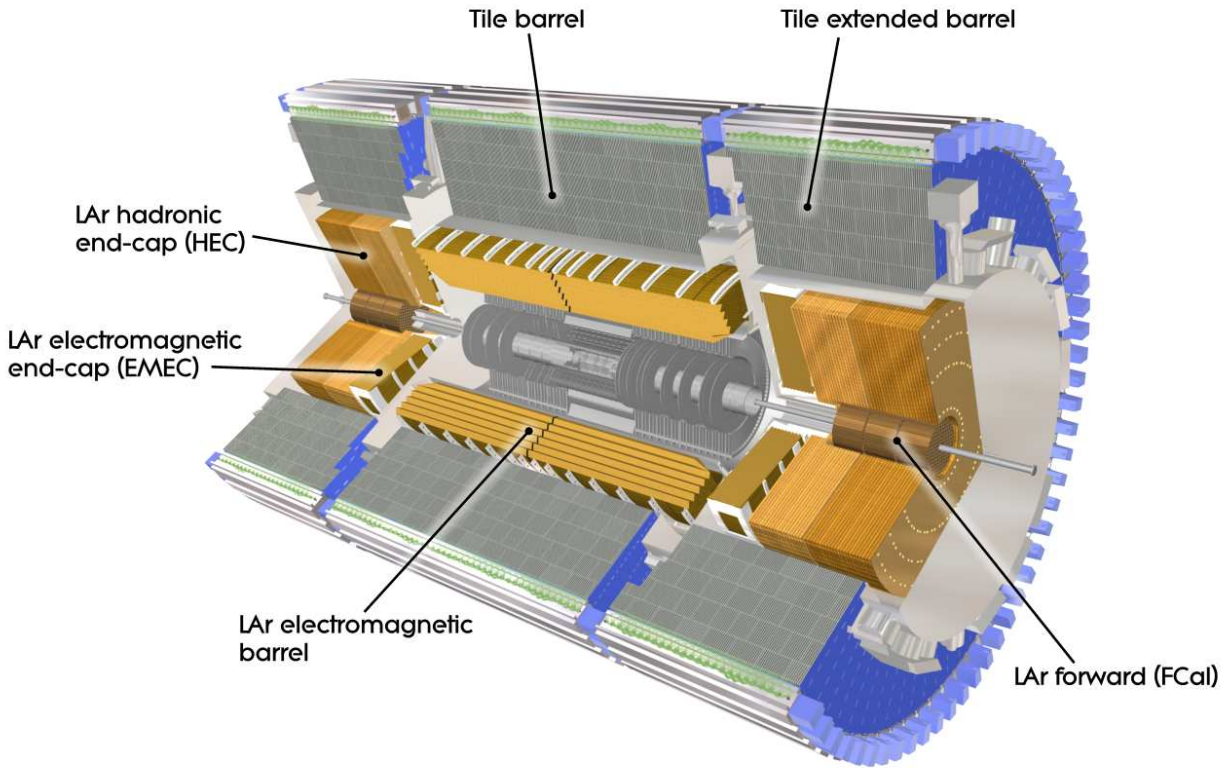

Figure2.8 Cut-away view of the ATLAS calorimeter system. The figure is cited from [25].

The geometry of the detector is summarized in Table 2.2. Since $1.37 < |\eta| < 1.52$ is intermediate region between the barrel and the end-caps, this region is called the crack region.

Hadronic calorimeter

The three types of hadronic calorimeter are located outside of the EM calorimeter.

The calorimeter placed outside of the EM calorimeter is the tile calorimeter. It consists of steel absorbers and scintillating tiles as the active detector medium. The main part covers $|\eta| < 1.0$, and two extended parts cover $0.8 < |\eta| < 1.7$.

Further high η region is covered by the LAr Hadronic End-cap Calorimeter (HEC) located behind the end-cap EM calorimeter. It consists of flat shape copper absorbers and liquid argon as the active detector medium. It covers $1.5 < |\eta| < 3.2$.

The most forward region is covered by the Forward Calorimeters (FCal), which has three layers. The first layer consists of flat shape copper absorbers and liquid argon as the active detector medium. The other layers consist of tungsten absorbers and liquid argon as the active detector medium. Due to high particle fluxes in this region, the gap for liquid argon is smaller than 0.6 mm, in contrast to the 2 mm gap for the EM calorimeter. It covers $3.1 < |\eta| < 4.9$.

2.2.3 Muon Spectrometer

Figure 2.8 shows the cut-away view of the ATLAS muon system. The system consists of four types of sub detectors and large toroid magnets arranged with an eight-fold azimuthal symmetry around the z axis. The barrel toroid magnet provides 1.5 to 5.5 Tm of magnetic field to the region $0 < |\eta| < 1.4$, and the end-cap toroid magnets provide 1 to 7.5 Tm of magnetic field to the region $1.6 < |\eta| < 2.7$.

The sub detectors are following; the Monitored Drift Tubes (MDT), the Cathode Strip Chambers

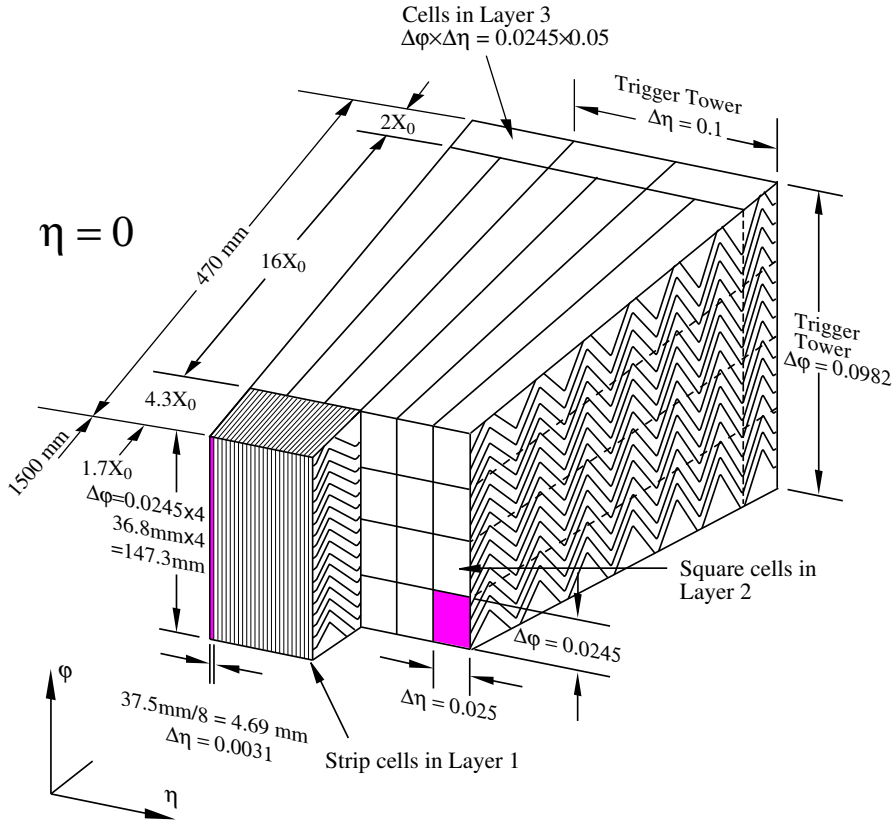

Figure2.9 Sketch of a barrel module of the electromagnetic calorimeter where the different layers are clearly visible with the ganging of electrodes in phi. The granularity in eta and phi of the cells of each of the three layers and of the trigger towers is also shown. The figure is cited from [25].

Table2.2 Geometry of EM calorimeter

Layers	Granularity ($\Delta\eta \times \Delta\phi$)	Covering η
Presampler in barrel	0.025×0.1	$\|\eta\| < 1.52$
Presampler in end-caps	0.025×0.1	$1.5 < \|\eta\| < 1.8$
1st layer of EM calorimeter in barrel	$0.025/8 \times 0.1$	$\|\eta\| < 1.4$
	0.025×0.025	$1.40 < \|\eta\| < 1.4$
1st layer of EM calorimeter in end-cap	0.050×0.1	$1.375 < \|\eta\| < 1.425$
	0.025×0.1	$1.425 < \|\eta\| < 1.5$
	$0.025/8 \times 0.1$	$1.5 < \|\eta\| < 1.8$
	$0.025/6 \times 0.1$	$1.8 < \|\eta\| < 2.0$
	$0.025/4 \times 0.1$	$2.0 < \|\eta\| < 2.4$
	0.025×0.1	$2.4 < \|\eta\| < 2.5$
	0.1×0.1	$2.5 < \|\eta\| < 3.2$
2nd layer of EM calorimeter in barrel	0.025×0.025	$\|\eta\| < 1.4$
	0.075×0.025	$1.40 < \|\eta\| < 1.475$
2nd layer of EM calorimeter in end-cap	0.050×0.025	$1.375 < \|\eta\| < 1.425$
	0.025×0.025	$1.425 < \|\eta\| < 2.5$
	0.1×0.1	$2.5 < \|\eta\| < 3.2$
3rd layer of EM calorimeter in barrel	0.050×0.025	$\|\eta\| < 1.35$
3rd layer of EM calorimeter in end-cap	0.050×0.025	$1.5 < \|\eta\| < 2.5$

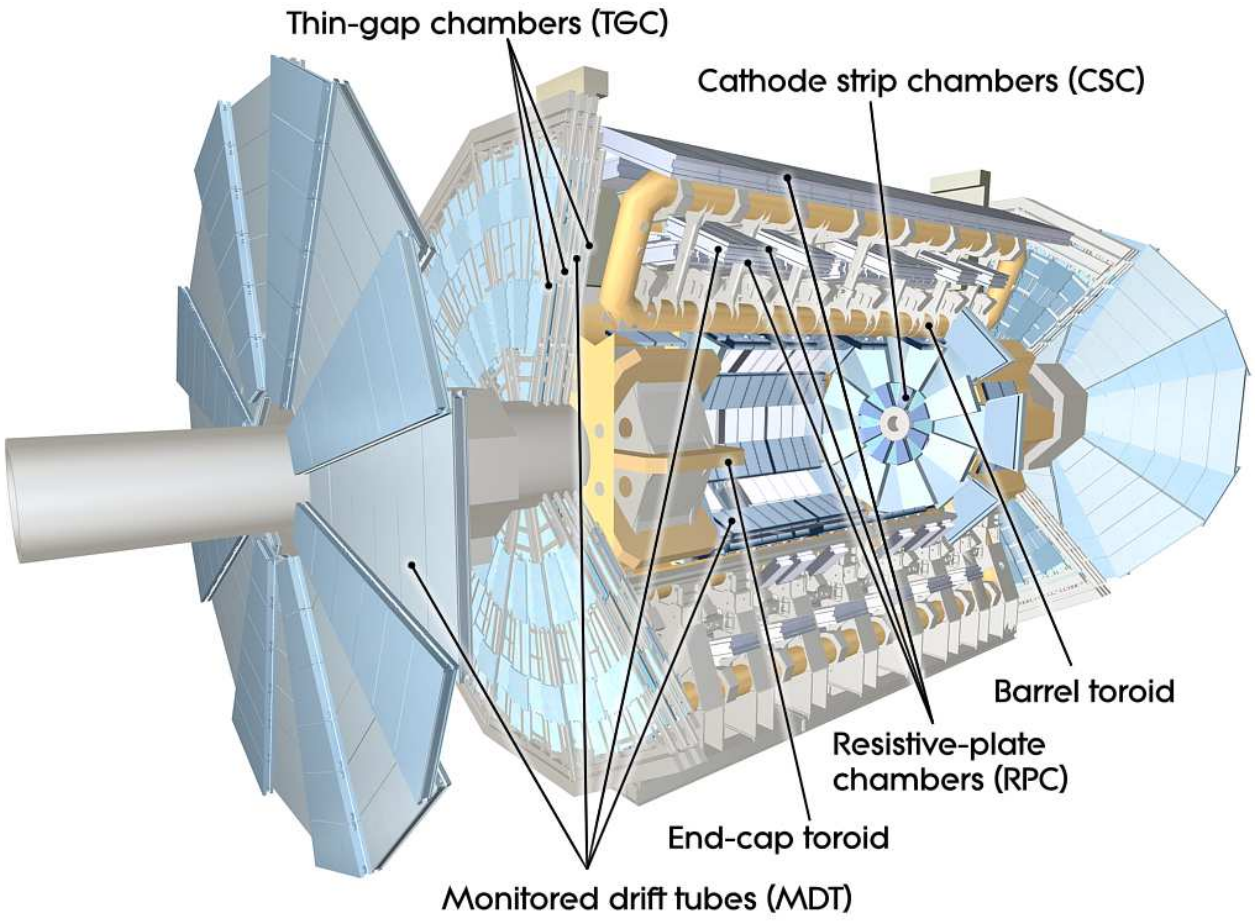

Figure2.10 Cut-away view of the ATLAS muon system. The figure is cited from [25].

(CSC), the Resistive Plate Chambers (RPC) and the Thin Gap Chambers (TGC). Figure 2.11 shows the cross-section of the muon system. Each sub-detector shown in the figure is described below.

Monitored Drift Tubes

The Monitored Drift Tubes (MDT) is the main detector to measure momentum precisely. The sensor of the MDT is drift tubes with a diameter of 29.970 mm, with the gold-plated tungsten-rhenium wire with a diameter of 50 μm. The tube is filled by the gas mixture with 3 bar. The design value of the gas mixture is 93% Ar and 7% CO_2, which achieves 2×10^4 gain with 3080 V. The position resolution of this sensor in transverse direction is 60-80 μm per tube. From the precise position measured by this detector, tracks are reconstructed and used to measure precise momentum.

This detector is shown in the figure with following naming:

- First character shows the location, barrel (B) or end-cap (E).
- Second character shows the layer, inner (I), middle (M), outer (O) or Extra (E).
- Last character shows the sector, large (L) or small (S).

As shown in the figure, it covers $|\eta| < 2.7$, except for the inner most layer which covers $|\eta| < 2.0$.

Cathode Strip Chambers

The Cathode Strip Chambers (CSC) covers the inner most layer of the forward region, where high counting rate is expected so the MDT cannot be used safely. The gap of the CSC is filled with the gas mixture of 80% Ar and 20% CO_2, which achieves 6×10^4 gain with 1900 V. The position

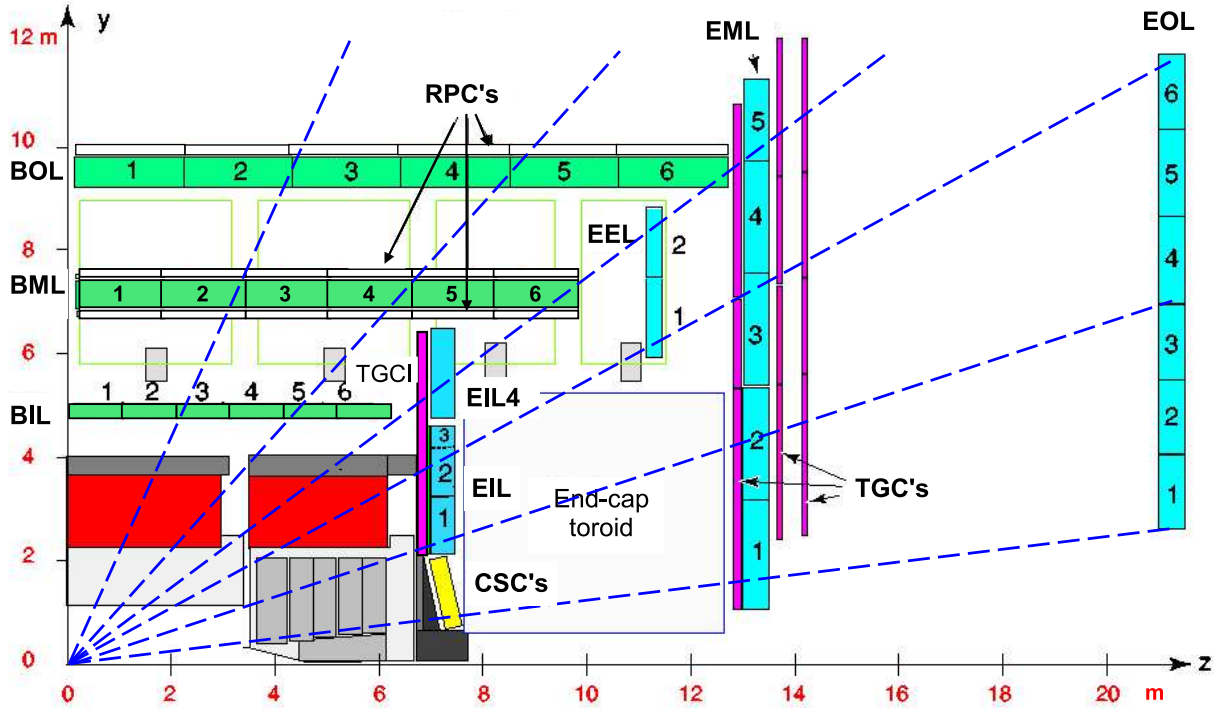

Figure2.11 Cross-section of the muon system in a plane containing the beam axis (bending plane). Infinite-momentum muons would propagate along straight trajectories which are illustrated by the dashed lines and typically traverse three muon stations. The figure is cited from [25].

resolution of this sensor is 60 μm per CSC plane. It covers the inner most layer of $2.0 < |\eta| < 2.7$.

Resistive Plate Chambers

The Resistive Plate Chambers (RPC) is for trigger system in barrel region. The detector consists of parallel 2 mm plastic plates with a 2 mm gap. The gap is filled with the gas mixture of 94.7% $C_2H_2F_4$, 5% Iso-C_4H_{10} and 0.3% SF_6, which achieves the detection efficiently greater than 98.5% per layer with 1900 V. It covers $|\eta| < 1.05$.

Thin Gap Chambers

The Thin Gap Chambers (TGC) is for trigger system in end cap region. The TGC is multi-wire proportional chamber. The wire to chamber distance is 1.4 mm, and the wire to cathode distance is 1.4 mm. The gap is filled with the gas mixture of 55% CO_2 and 45% n-pentane, which achieves 3×10^5 gain with 2900 V. It covers $2.0 < |\eta| < 2.7$.

2.2.4 Trigger system

As described in Section 2.1.1, the bunch space of the LHC is 25 nsec. Hence, collision rate is detected in 40 MHz. However, most of the detected events are background events. Because of limited resource for the data acquisition, all events cannot be recorded. Therefore, the trigger system, which filters only interesting events, is used in the ATLAS experiment. Figure 2.12 shows the overview of the trigger system. There are two types of trigger system used in the ATLAS experiment; the Level 1 (L1) trigger and the high level trigger, as described below.

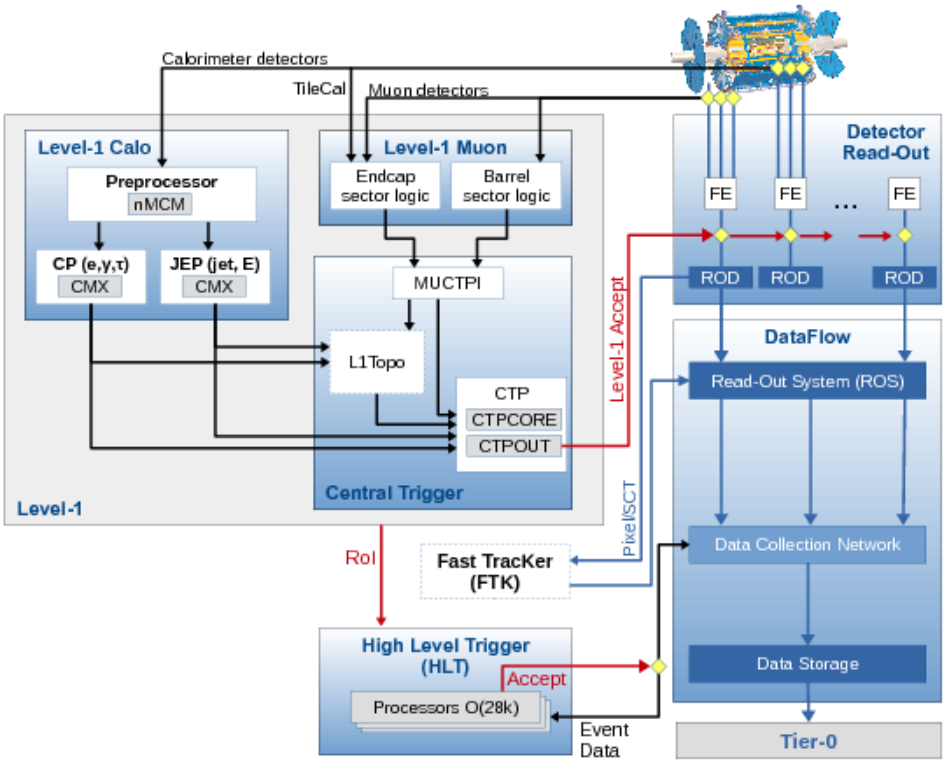

Figure2.12 The ATLAS trigger and data acquisition system in Run 2 with emphasis on the components relevant for triggering, cited from [28]

L1 trigger

The L1 trigger is hardware-based trigger. This trigger gives decision based on the information from the calorimeter and the muon system, for the barrel region and the end-cap region individually. The information related to muon is processed at the level-1 Muon system, and calorimeter information is processed at the level-1 Calo system, by a new FPGA-based multi-chip module (NMCM). Then the Cluster Processor (CP) identify electron/photon and tau, and Jet/Energy-sum Processor (JEP) identify jets and missing transverse momentum. The outputs from the level-1 muon system is processed at the Muon-to-CTP interface (MUCPTI). The outputs from the level-1 Calo system and MUCPTI are used at Level 1 Topological trigger (L1Topo) to combine the objects. All those information are processed at the Central Trigger Processor (CTP), which submits L1 trigger based on dedicated trigger menu. L1 trigger is accepted by the Read Out Driver (ROD).

Only when L1 trigger is accepted, the ROD for all the detector starts read out data from the Front End (FE) chips. The L1 trigger menu is designed to achieve ∼100 kHz of read out.

High Level Trigger

The next step of the trigger is the High Level Trigger (HLT). This is software-based trigger.

The data taken by L1 triggers are buffered in the Read-Out System (ROS). Then, based on the L1 trigger information, the Region-of-Interest (RoI) is used at the HLT processors. Online reconstructions are performed only for the objects in the RoI, and the dedicated HLT algorithm is applied.

Only events accepted by the HLT are recorded in the Data Storage. The HLT menu is designed to achieve ∼1 kHz of data recording.

Chapter 3

Data and Simulation samples

The search for new physics is generally performed as a search for the deviation from the expectation based on the SM. The events expected by the SM are background for such search, and the events expected by new physics are signal. In order to search for the deviation, it is important to understand the characteristics of the background and the signal. Both expectation, based on the SM and new physics, can be provided by simulated samples. In this chapter, details of collected data and simulated samples are introduced.

3.1 Data samples

The LHC has been operated at $\sqrt{s} = 13$ TeV from 2015. The dataset used in this analysis is collected using the ATLAS detector in 2015 and 2016. Figure 3.1 shows the integrated luminosity in 2015 and 2016. Because of the DAQ inefficiency and the start up time for the electronics of the tracking detectors, not all of the delivered luminosity can be recorded, as shown in the figures.

Total recorded integrated luminosity is 3.9 fb^{-1} in 2015 and 35.6 fb^{-1} in 2016. However, some of those data were recorded when a sub detector system had a trouble. The largest effect in 2015 is that the IBL was turned off for two runs, corresponding to 0.2 fb^{-1}. And the largest effect in 2016 is that the toroid magnet was off for some runs, corresponding to 0.7 fb^{-1}. The data collected when some sub detector had a trouble are removed and not used in the analysis. Total integrated luminosity used in the analysis is 3.2 fb^{-1} in 2015, and 32.9 fb^{-1} in 2016. Therefore, overall integrated luminosity used in the analysis is 36.1 fb^{-1}.

3.1.1 Trigger

As described in Section 2.2.4, data is collected using prepared triggers. In this analysis, the used dataset is collected by diphoton trigger, which is dedicated for the events contain two or more photons. Among several types of the diphoton triggers developed in the ATLAS experiment, HLT_g35_LOOSE_g25_LOOSE, which is the loosest type of trigger, is used for this analysis. This trigger is dedicated for the events containing leading photons with greater than 35 GeV transverse momentum and sub-leading photons with greater than 25 GeV transverse momentum. The efficiently of this trigger for the target diphoton events are closest to 100% [30].

3.1.2 Blind analysis

The collected data is used not only for the estimations of the existence of new physics, but also for the evaluations of the backgrounds. At first background estimations have been performed, then observed data is compared with the expected backgrounds. Within the procedure of the background estimation, collected numbers of events or distributions of data, which are used for the estimation of the existence of new physics, are hidden, in order to avoid artificial bias, such as under estimation of the background. This procedure is called “blind” analysis, and the hidden region is called blinded

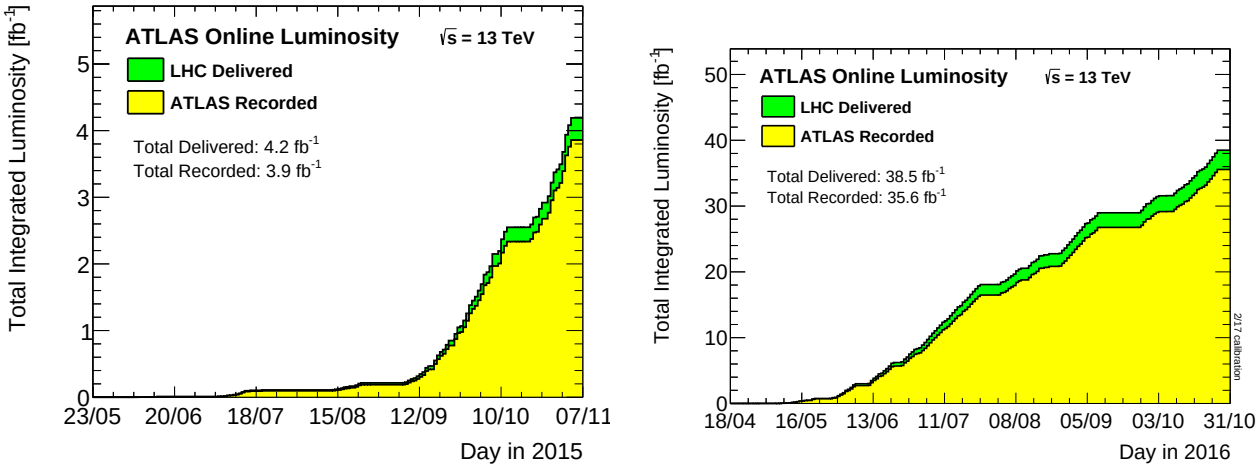

Figure3.1 Total integrated luminosity in 2015 (left) and 2016(right) versus time. Delivered integrated luminosity is shown in green, and recorded integrated luminosity is shown in yellow. The figures are cited from [29].

region, which is equivalent to the signal region described in Table 5.1. The background estimations described up to Chapter 8 have been performed with blinded data, and the blinded region is opened in Chapter 9. Instead of using data in the signal region, the simulation samples described in the next section is used as expected distributions.

3.2 Simulation samples

Monte Carlo (MC) simulation samples are produced for background estimation and evaluation of the significance of the signals. Event generators are used to simulate proton-proton inelastic scattering, parton shower, and hadronization. As an input to the simulation, prepared Parton Distribution Function (PDF) set is used. Non-perturbative parameters for the simulation, which cannot be determined from theories, are "tuned" to reproduce the observed event. Depending on the physics process, several types of generators, PDFs and tunes are used. Those are explained in this section. The generated events are used as inputs to simulator for the detector system based on the GEANT4 [31, 32]. Outputs of the detector simulation contain energy deposits, hit timing, etc. in detector elements. These are further transformed to the digital outputs from detector components through digitization process. These data are in the same format as the ones from the data from real detector.

The MCs for the backgrounds are explained in Section 3.2.1. The MCs for the signals are explained in Section 3.2.2.

3.2.1 Backgrounds

As described in Figure 1.7, two photons, one lepton and the missing transverse energy ($E_{\mathrm{T}}^{\mathrm{miss}}$) are expected in the final state of the signal. Some types of the events predicted in the SM have the same final state with signal. Therefore, those are expected as background sources.

Those backgrounds sources are classified into two types. The backgrounds including a SM higgs particle within their process is classified as "peaking backgrounds", which are Wh, Zh, $t\bar{t}h$, VBFh and ggh. And the other type of the backgrounds is "non-peaking backgrounds", which are $W\gamma\gamma$, $Z\gamma\gamma$, $W\gamma$, $Z\gamma$, $\gamma\gamma$, $t\bar{t}$, and single photon. All samples are summarized in Table 3.1.

As described in Section 6.1, MC samples for the non-peaking backgrounds are not used for the estimation of their contributions. Instead, the estimation for the non-peaking backgrounds has been

performed with data-driven method. Those MC samples are only used for the comparison between the data used in the data-driven method and the SM expectation. On the other hand, the MC samples for the peaking backgrounds are directly used for the backgrounds estimation. Because of this reason, two types of MC samples for Wh and Zh are used in the analysis.

The non-peaking backgrounds except for the $t\bar{t}$ are generated using the leading order (LO) generator SHERPA v2.1.1 simulation package [33] with the CT10 PDF set [34]. The tunes have been done inside SHERPA.

The $t\bar{t}$ is generated using the NLO generator POWHEG [35] for the hard scatterings and PYTHIA6 [36] for the rest with the CT10 PDF set. For the tunes, the Perugia2012 [37] tune is used.

The first set of the Wh and Zh samples are called "LO samples", since those samples are generator with the LO generator. Those are generated using the LO generator PYTHIA8 [38] with the NNPDF2.3LO PDF set [39, 40]. For the tune, the A14 [41] tune is used. The LO samples are used with the early selections, which are introduced in Section 5.1, for the optimization and some validations.

The next set of the Wh and Zh samples are called "NLO samples", since those samples are generator with the next-to-leading order (NLO) generator. Those are generated using the NLO generator POWHEG+MiNLO for the hard scatterings and PYTHIA8 for the rest with the CT10 and CTEQ6L1 [42] PDF sets. For the tunes, the AZNLO tune [42] is used. The total cross section for the normalization is calculated with NNLO QCD and NLO EW. Then, the correction for EW at NLO is applied by the reweighting factor based on the truth transverse momentum of W or Z.

The LO samples are used in the early stage of analysis. The NLO samples are used mainly for the statistical evaluation of the results. The effect of the difference of the sample is evaluated in Section 7.4.2 as negligible level.

The VBFh and ggh are generated using the LO generator PYTHIA8 with the CTEQ6L1 PDF set. For tune, the AZNLO tune is used. The processes are calculated with LO, then scaled to NNLO by applying scaling factor called k-factor.

The $t\bar{t}h$ are generated using aMcAtNlo [43] for the hard scatterings Herwigpp V2.7.1 [44] for the rest with the CT10 and CTEQ6L1 PDF sets. For the tune, the CTEQ6L1-UE-EE-5 tune [45] is used.

3.2.2 Signals

The signal samples are created under the assumptions described in Section 1.2.3. The only free parameters are the mass of LSP ($m_{\tilde{\chi}_1^0}$) and the mass of NLSP and the lightest chargino ($m_{\tilde{\chi}_1^\pm,\tilde{\chi}_2^0}$). Figure 3.2 shows the points of the values of the created signal points in the $m_{\tilde{\chi}_1^0}$ versus $m_{\tilde{\chi}_1^\pm,\tilde{\chi}_2^0}$ parameters space. As shown in the figure, there is a theoretical limitation about $m_{\tilde{\chi}_1^0}$ and $m_{\tilde{\chi}_1^\pm,\tilde{\chi}_2^0}$. Since $\tilde{\chi}_2^0 \to \tilde{\chi}_1^0 h$ is assumed, $m_{\tilde{\chi}_1^\pm,\tilde{\chi}_2^0} - m_{\tilde{\chi}_1^0}$ must be larger than the Higgs mass. This is shown as a

Table3.1 Simulation samples used in this analysis.

process	generator	PDF	tune
$t\bar{t}$	POWHEG + PYTHIA	CT10	Perugia2012
All other non-peaking backgrounds	SHERPA	CT10	SHERPA
Wh and Zh LO samples	PYTHIA	NNPDF2.3LO	A14
Wh and Zh NLO samples	POWHEG + MiNLO + PYTHIA	CT10 and CTEQ6L1	AZNLO
VBFh and ggh	PYTHIA	CTEQ6L1	AZNLO
$t\bar{t}h$	aMcAtNlo + Herwigpp	CT10 and CTEQ6L1	CTEQ6L1-UE-EE-5

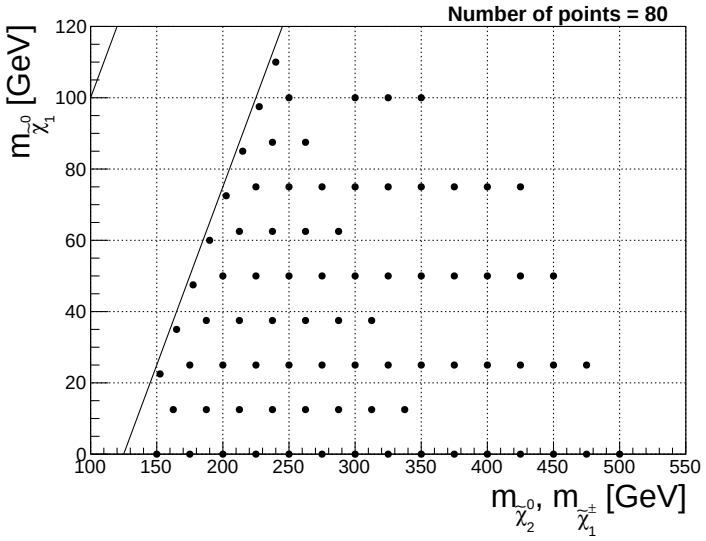

Figure3.2 Assumed signal sample points in $(m_{\tilde{\chi}_1^\pm,\tilde{\chi}_2^0}, m_{\tilde{\chi}_1^0})$ space. The diagonal line shows $m_{\tilde{\chi}_1^\pm,\tilde{\chi}_2^0} - m_{\tilde{\chi}_1^0} = 125$ GeV.

diagonal line in the figure.

All the signal samples are generated using MG5_aMC@NLO v2.3.3 [46] for the matrix element calculation for the hard process part and PYTHIA8 for the rest with the NNPDF23LO PDF set [39]. For the tune, the A14 tune is used. The fast simulation (Atlfast-II [47]) is used for the simulation of the detector response, instead of the "full" simulation used for the other samples. The cross sections for those samples, which depend on $m_{\tilde{\chi}_1^\pm,\tilde{\chi}_2^0}$, are summarized in Table 3.2.

Table3.2 Cross sections of assumed signal sample points.

$m_{\tilde{\chi}_1^\pm,\tilde{\chi}_2^0}$ [GeV]	Cross sections [fb]
150	5.1809
152.5	4.8789
162.5	3.8718
165	3.6621
175	2.9533
177.5	2.8037
187.5	2.2927
190	2.1837
200	1.8074
202.5	1.7261
212.5	1.4431
215	1.3815
225	1.1651
227.5	1.1180
237.5	0.9137
240	0.9137
250	0.7825
262.5	0.6494
275	0.5430
287.5	0.4570
300	0.3869
312.5	0.3295
325	0.2819
337.5	0.2425
350	0.2094
375	0.1581
400	0.1210
425	0.0938
450	0.0734
475	0.0581
500	0.0464

Chapter 4

Object Reconstruction

Events in collected data and generated simulations contain hit information on the detector. From those, candidates of the physics objects, such as photons, leptons, jets, which are a collimated spray of hadrons coming from QCD activities, and missing transverse momentum ($E_{\mathrm{T}}^{\mathrm{miss}}$), are reconstructed. Then, specific selection criteria for each type of object are applied. In this chapter, reconstruction procedures for each object are described.

4.1 Term definitions

Hit information on the detector are interpreted as tracks and deposit energies, and then reconstructed as physics objects. Before the introductions about the reconstruction procedures, which are described in the next section, some terms used in the explanations are defined in this section.

4.1.1 E_{T} and p_{T}

Tracks of charged particles are reconstructed by hit information on the ID [48]. As described in Section 2.2, 2 T solenoidal magnetic field is provided to the tracking volume. Because of the field, charged particle draws curved path in the ID. From the curvature radius in x-y plane, transverse momentum p_{T} can be measured. In this chapter, p_{T} means the transverse momentum measured by track. Hit information on the calorimeters are interpreted as deposit energy. In this chapter, it is denoted as E_{T} (transverse energy).

E_{T} and p_{T} have relation such as

$$E_{\mathrm{T}} = \sqrt{m^2 + p_{\mathrm{T}}^2}. \tag{4.1}$$

Since mass m is negligible comparing to scale of E_{T} and p_{T}, E_{T} of correctly reconstructed object is equal to p_{T}. After this chapter, assuming all objects are correctly reconstructed, all momentum or energy are denoted by p_{T}.

4.1.2 Primary vertexes and μ

The other term used in this chapter is the primary vertex. Since the ATLAS collects collisions of proton beams, there are multiple interactions expected in a beam crossing. The number of interactions in a beam crossing is denoted as μ[*1]. The point of each interaction is denoted as primary vertex.

The primary vertex is reconstructed by track information. Reconstructed tracks are extrapolated to the beam spot center, then the z coordinate of the primary vertex is evaluated. The tracks sharing the primary point are used to determine the vertex position. More detail are described in [49].

[*1] This is used in Table A.2

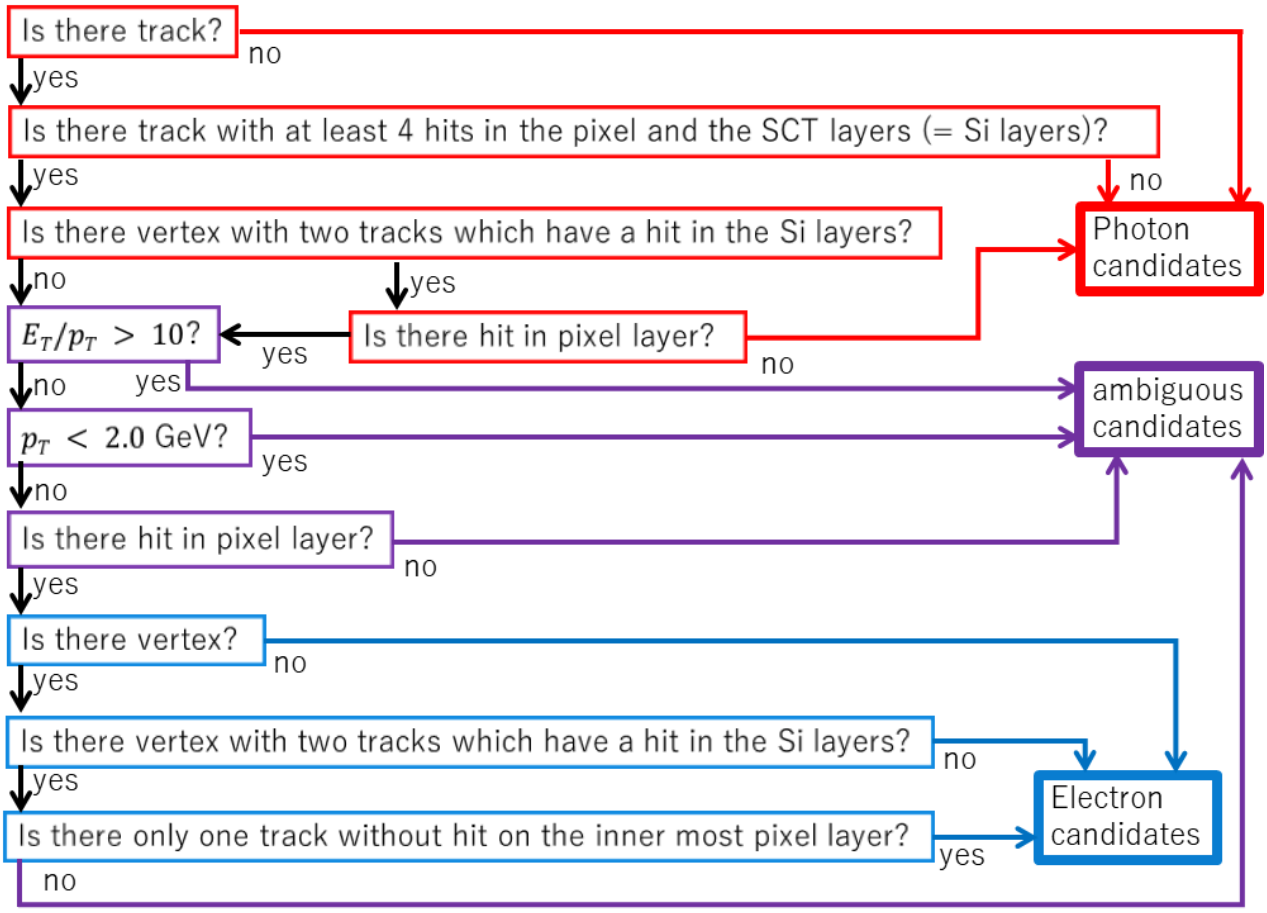

Figure4.1 Photon and electron candidates classification workflow.

4.2 Objects

4.2.1 Photons and Electrons

Reconstruction of candidates

Due to their simulator characteristics in the detector, a photon object and an electron object are reconstructed in the same workflow described in following.

At first, electromagnetic clusters of the cells of the second EM calorimeter layer are reconstructed. For this reconstruction, $\eta \times \phi = 3 \times 5$ cells of the window are used for the scan of the local maximum of the total E_{T}. If E_{T} of the cluster is greater than 2.5 GeV, it is used as a seed of the object. Then, the energy collected around the seed are used as inputs to the clustering algorithm [50] to construct topological cluster.

When a cluster is constructed at EM calorimeter, candidates of the associated tracks are defined by the tracks reconstructed by the inter detector that are matched to the cluster by the extraction of the track. If a vertex for two associated tracks are reconstructed, it is saved as a candidate for the photon conversion vertex.

By using those information, object are classified as a photon, an electron or an "ambiguous" object which could be a photon or an electron. Only when object is surely not considered to be an electron (photon), it is classified as a photon (electron) candidate respectively. Figure 4.1 shows the overview of the classification algorithm, which is described below.

In the following cases, the object is classified as a photon.

- There are no tracks.
- There are no tracks with at least 4 hits in silicon layers (the pixel detector and the SCT).
- There is a vertex reconstructed by two tracks which have hit on the silicon layers but no hit in the pixel layers. In this case, the object is considered as a converted photon.

When the object is not classified as a photon, the object is checked about following criteria:

- $E_{\mathrm{T}}/p_{\mathrm{T}} < 10$. Otherwise, the object is not likely an electron since p_{T} of an electron measured by the track should be close to its E_{T}.
- $p_{\mathrm{T}} > 2.0$ GeV. Otherwise, the object has too low momentum to conclude it is an electron candidate.
- There is a track with a hit on the pixel layers. Otherwise, the object is not likely an electron since it is rare for an electron track.

In the cases that the object cannot pass at least one of the criteria listed above, the object is classified as an ambiguous object, since it is not classified as a photon, nor an electron.

The object, which is not classified as a photon or an ambiguous object, is classified as an electron candidate in the following cases:

- There are no vertices.
- There is a vertex but it is due to accidental vertex with cosmic ray or noise. To confirm it, a vertex must pass one of following criteria:
  - It is not reconstructed by two tracks having a hit on the pixel layers.
  - It is reconstructed by two tracks having a hit on the pixel layers, but only one track has a hit on the inner most pixel layer.

The object which dose satisfy any criteria above is classified as an ambiguous object. The ambiguous objects are used as both photon and electron candidates in the following selection procedure.

Selection of photon candidates

The dedicated criteria for the photon candidates and for the electron candidates are applied to the classified objects. The ambiguous objects are used as both candidates in this step, and overlap is removed later.

For the photon candidates, following criteria are applies:

- passing "Tight" photon IDentification (ID)
- $|\eta| < 2.37$ excluding the crack region of $1.37 < |\eta| < 1.52$ (See Section 2.2.2)
- passing "FixedCutTightCaloOnly" isolation criterion
- $E_{\mathrm{T}} > 27$ GeV

An important purpose of those requirements is to reduce fake candidates mostly due to π^0 mesons decaying to two photons. Two photons decayed from a π^0 with high momentum are collimated and geometrically close at the EM calorimeters. Therefore, the cluster at the second EM calorimeter can be merged into one cluster. Since the signal detected at the second EM calorimeter is due to photons, even if it is originally from π^0, it is difficult to distinguish it from truth prompt photons. The criteria described above are designed to reduce such fake candidates, as following.

The photon ID is developed in the ATLAS experiment to distinguish truth photons from fake photons, as described in [51]. It is based on the energy deposits in the first and second EM calorimeter, and the leakage into the hadronic calorimeter. The ID was tuned to provide about 85% efficiency at 40 GeV.

The first EM calorimeter provides useful information in the photon ID definition. As described in Section 2.2.2, it has fine segmentation to detect two photons from π^0 separately. In order to ensure the quality of the photon ID, the requirement on the η measured by the first EM calorimeter is applied.

The isolation requirement is a different approach to reduce fake candidates. In general, mesons,

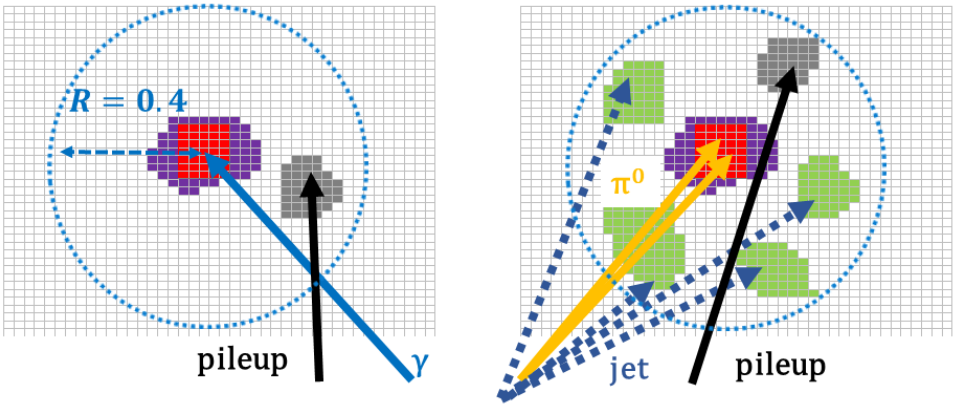

Figure4.2 Schematics of topoEtcone40. Images shows the cells of the second EM calorimeter layer. Left image is for photon, and right image is for π^0 decayed into diphoton. There are pileup effects for both cases. For π^0 case, there are jet contributions also. topoEtcone40 is calculated from total deposits energy ($\Sigma_{R<0.40}E_{\mathrm{T}}$) within $R = 0.4$ cone, which is shown as a blue circle. In order to remove contribution of photon, deposits energy within $\eta \times \phi = 5 \times 7$ window ($E_{\mathrm{T}}^{5\mathrm{x}7\ \mathrm{core}}$), which is shown as red cells, is subtracted. Then, expected deposits energy leaked from the window ($f_{\mathrm{leak}}(E_{\mathrm{T}}^{5\mathrm{x}7\ \mathrm{core}}, \eta)$), which is shown as purple cells, is calculated and subtracted. Finally, pileup effect ($\rho(\eta)$), which is shown as gray cells, is subtracted. topoEtcone40 for photon is close to 0. On the other hand, topoEtcone40 for π^0 can be large value due to jet contributions shown as green cells.

such as π^0, are generated by the strong production, while photons are generated by the electroweak production. Therefore, other QCD activities, such as jets, are expected to be around a meson, which are not expected for a truth photon. The isolation requirement is suppressing objects with such jets activities. Several types of the criteria are developed in the ATLAS experiment.

In this analysis, "FixedCutTightCaloOnly" is used as the isolation criterion. This is the requirement on the calorimeter isolation energy, represented by topoEtcone40. Figure 4.2 shows the schematic of the topoEtcone40 definition. Idea of topoEtcone40 is total energy deposits around photon candidates. It is evaluated from the total energy deposits within an $\eta - \phi$ cone of a radius $\Delta R = 0.40$ around the center of the cluster of the photon candidate ($\Sigma_{R<0.40}E_{\mathrm{T}}$). $\Sigma_{R<0.40}E_{\mathrm{T}}$ include energy deposits of photon candidate and pileup effect also. In order to evaluate energy deposits inside cone except for photon, energy deposits of photon is evaluated separately and subtracted. It is evaluated from deposits energy within $\eta \times \phi = 5 \times 7$ window ($E_{\mathrm{T}}^{5\mathrm{x}7\ \mathrm{core}}$) at first. Then, expected deposits energy leaked from the window is calculated using a dedicated function of $E_{\mathrm{T}}^{5\mathrm{x}7\ \mathrm{core}}$ and η ($f_{\mathrm{leak}}(E_{\mathrm{T}}^{5\mathrm{x}7\ \mathrm{core}}, \eta)$). Pileup effect ($\rho(\eta)$) is also evaluated as a function of η. Then, topoEtcone40 can be defined as:

$$\mathrm{topoEtcone40} = \Sigma_{R<0.40}E_{\mathrm{T}} - E_{\mathrm{T}}^{5\mathrm{x}7\ \mathrm{core}} - f_{\mathrm{leak}}(E_{\mathrm{T}}^{5\mathrm{x}7\ \mathrm{core}}, \eta) - \rho(\eta) \tag{4.2}$$

Due to uncertainty on the $f_{\mathrm{leak}}(E_{\mathrm{T}}^{5\mathrm{x}7\ \mathrm{core}}, \eta)$, the width of the topoEtcone40 become wider with larger $E_{\mathrm{T}}^{5\mathrm{x}7\ \mathrm{core}}$. Therefore, the threshold of "FixedCutTightCaloOnly" is tuned as a function of the photon transverse energy, as following:

$$\mathrm{topoEtcone40} < 2.45\mathrm{GeV} + 0.22 \times E_{\mathrm{T}} \tag{4.3}$$

The last criterion is on photon transverse energy. In this analysis, further selections are applied in the signal region requirement. This is discussed in Section 5.3.2.

Selection of electron candidates

For the electron candidates, following criteria are applied:

- passing "TightLLH" electron IDentification (ID)
- $|\eta| < 2.47$ excluding the crack region of $1.37 < |\eta| < 1.52$
- passing "gradient loose" isolation criterion
- $|z_0 \sin\theta| < 0.5$ mm
- $|d_0/\sigma_{d_0}| < 5.0$
- $p_{\mathrm{T}} > 15$ GeV

In the case of the electron candidates, main source of the fake are hadronic jets and photons converting to electron positron pairs. Electrons in hadronic jets or converted from the photon can be electron candidates, even if they are not prompt electrons.

The "TightLLH" electron ID is developed based on the log likelihood (LLH) with the multivariate analysis (MVA) technique [52]. The definition of the "TightLLH" uses information from the hadronic calorimeter, the EM calorimeter and the inner detectors.

The η cut is based on the range where the four momentum of the electron can be calculated based on the track measured by the inner detectors.

The isolation requirement is to suppress hadronic jets, as it is for the photon isolation. For the isolation requirement, two discriminating variables are used: a calorimetric isolation energy and a track isolation. The calorimetric isolation energy is evaluated by topoEtcone20, which is the same with topoEtcone40 except for the size of the radius for the calculation which is $\Delta R = 0.20$ instead of 0.40. The track isolation is represented by ptvarcone40. It is defined as the sum of transverse momentum of all the track within a cone of $\Delta R = \min(0.40, 10\mathrm{GeV}/E_{\mathrm{T}})$ around the candidate electron track, excluding the electron associated track. The track used in this calculation are only those which pass following criteria:

- $p_{\mathrm{T}} > 1$ GeV
- 7 or more hits in the silicon layers
- 2 or less missing hits in the silicon layers
- 1 or less missing hits in the pixel layers
- 1 or less hits in the silicon layers assigned to more than one track
- $|z_0 \sin\theta| < 0.3$ mm

The "gradient loose" criterion is tuned to provide 95% of the total efficiency for 25 GeV electrons, and 99% total efficiency at 60 GeV. The thresholds for calorimetric isolation energy and track isolation are not fixed values. The total efficiency is evaluated by using simulation of $Z \to ee$.

The selection for z_0 and d_0 is to request that the origin of the track is close to the primary vertex, which is the common origin for the high-quality reconstructed tracks. Those parameters are called impact parameters, which are showing distance from the primary vertex to the track, as shown in Figure 4.3. d_0 is the closest distance from the track to the primary vertex in the (x, y) plane. z_0 is the z intercept in the (z, direction of p_{T}) plane. d_0 is divided by uncertainty on d_0 and requested that the size of d_0 is within 5σ. z_0 is weighted by $\sin\theta$, where θ is track angle from the z axis. $z_0 \sin\theta$ means distance from the track to the primary vertex in the (z, direction of p_{T}) plane.

The last criterion is on electron momentum. In this analysis, further selections are applied in the signal region requirement. This is discussed in Section 5.3.3.

4.2.2 Muons

Reconstruction of candidates

Muon candidates are reconstructed using the information from the inner detectors and the muon spectrometer (MS).

At first stage of the reconstruction, muon candidates are reconstructed by the inner detectors and the muon spectrometer individually. The reconstruction with the inner detector is performed as did for other charged particles. On the other hand, the reconstruction with the muon spectrometer is performed as following steps:

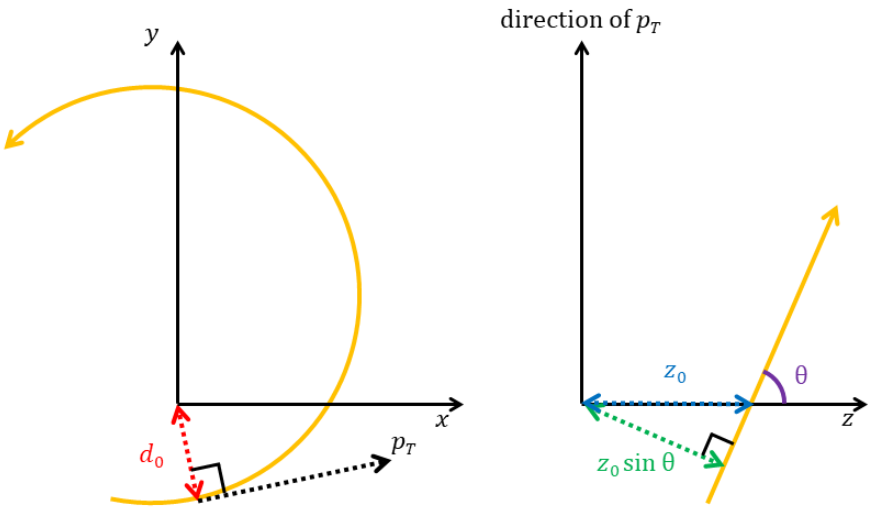

Figure4.3 Image of the impact parameters. Left image shows an image of d_0. Charged particle draw an arc in the (x, y) plane as shown as an orange arrow. d_0 is closest distance from the track to the primary vertex in the (x, y) plane, which is shown as a red arrow. Right image shows an image of $z_0 \sin\theta$. z_0 is the z intercept in the (z, direction of p_{T}) plane, which is shown as a blue arrow. With weight of $\sin\theta$, where θ is is track angle from the z axis, closest distance from the track to the primary vertex in the (z, direction of p_{T}) plane ($z_0 \sin\theta$) is evaluated, as shown as $z_0 \sin\theta$.

- Hit patterns for the muon track candidates are searched inside each muon chamber in the MS.
- The track candidates are reconstructed by fitting hits on different layers. The fit is performed from the seeds generated from the hit segments in the middle layers of the detector, and then extended to the inner and outer layers.
- If there are segments used by several track candidates, an overlap removal algorithm is applied. The algorithm selects the best assignment of the segment to a single track or two tracks as a shared segment.
- The hits associated with each track candidate are fitted using a global χ^2 fit to remove low quality tracks from the candidates.

After the individual reconstruction by the inner detectors and the muon spectrometer, those information are combined in several ways. Depending on which subdetectors are used in the reconstruction, four types of the muons are defined [53]. In this analysis, only following two types of the muon are used as muon candidates.

- Combined muons: A combined track is formed from the tracks reconstructed by the inner detectors and the muon spectrometer using global refit. Most of the muons are reconstructed by the pattern recognition from the muon spectrometer and then extrapolating to the track in inner detectors.
- Extrapolated muons: a muon track is reconstructed only using the track in the muon spectrometer with a loose requirement on compatibility with originating from the interaction point when extrapolating the track. This is to extend the acceptance for muon reconstruction into the region $2.5 < |\eta| < 2.7$, which is not covered by the inner detectors.

Selection of muon candidates

For the reconstructed muon candidates, following criteria are applied:

- passing “medium” muon IDentification (ID)

- $|\eta| < 2.7$
- passing "gradient loose" isolation criterion
- $|z_0 \sin\theta| < 0.5$ mm
- $|d_0/\sigma_{d_0}| < 3.0$
- $p_{\mathrm{T}} > 10$ GeV

Those criteria are to suppress background, mainly from pion and kaon decays, while keeping high efficiency for the prompt muons and guaranteeing a robust momentum measurement,

The "medium" muon ID is developed as the default selection for muons in the ATLAS experiment, to minimize the systematic associated with muon reconstruction and calibration. Individual criteria for the Combined muons and for the Extrapolated muons are defined in [53], based on the information from the muon spectrometer and the inner detectors. The reconstruction efficiency of the muon with this muon ID is greater than 95%. The η cut is based on the region covered by three layers of MDTs. Since the Combined muon candidates are reconstructed within the inner detector coverage ($|\eta| < 2.5$), and the Extrapolated muon candidates are reconstructed in $2.5 < |\eta| < 2.7$, this cut does not affect the candidates.

The isolation requirement is to suppress muon from semileptonic decays in hadronic jets. As in the case of electron, muons originating from the decay of heavy particles, such as W, Z or higgs are often produced with isolation from other particles, unlike the muons from semileptonic decays. As discriminating variables for the muon isolation, topoEtcone20 and ptvarcone30 are used. The definitions of them are the same with the ones for the electron isolation, expect for the cone size of ptvarcone30, which is $\Delta R = \min(0.30, 10\mathrm{GeV}/E_{\mathrm{T}})$

The "gradient loose" criterion is tuned to provide 95% of the total efficiency for 25 GeV muons, and 99% total efficiency at 60 GeV, which are the same working point as the case of the electrons. The total efficiency is evaluated by using simulation of $Z \to \mu\mu$.

The selection for z_0 and d_0 is, again as it is for the electron, to request that the origin of the track is close to the primary vertex.

The last criterion is on muon momentum. In this analysis, further selections are applied in the signal region requirement. This is discussed in Section 5.3.3.

4.2.3 Jets

Reconstruction of candidates

Quarks and gluons generated by proton-proton collision immediately transform into bunch of hadrons, as described in Section 1.1.1. It is detected as a "jet" in the detector.

The candidates of the jet objects are reconstructed using the anti-k_T algorithm [54] with a distance parameter $R = 0.4$. The input to the algorithm is the topological clusters [55] at the calorimeters. Several topological clusters are combined as following:

- For all the combination of the topological clusters i and j, distances $d_{ij} = \min(p_{T_i}^{-2}, p_{T_j}^{-2})\frac{\Delta_{ij}^2}{R^2}$ and $d_{iB} = p_{T_i}^{-2}$ are calculated, where $\Delta_{ij}^2 = (y_i - y_j)^2 + (\phi_i - \phi_j)^2$ and p_{T_i}, y_i, ϕ_i are the transverse momentum, rapidity and azimuthal angle around z-axis of the cluster i.
- The minimum distance is searched.
  - If d_{iB} is the minimum, the cluster i is classified as a jet and removed from the list of the clusters.
  - If d_{ij} is the minimum, the cluster i and the cluster j are combined into one cluster.
- The steps described above are repeated until all the clusters are combined and classified as jets.

With this algorithm, clusters within the distance parameter R are combined into one cluster. If there are several clusters within R, the cluster with high momentum has priority to be combined.

Selection of candidates

To all the candidates of jets, two acceptance cuts, $p_T > 30$ GeV and $|\eta| < 2.8$, are applied. In order to suppress the contributions from pile-up jets, the Jet Vertex Tagger (JVT) cuts are applied. JVT is likelihood that the jet is hard scatter jet [56]. Jets are rejected if they have $p_T < 60$ GeV, $|\eta| < 2.4$, and JVT < 0.59.

The selections described above are all for the jet candidates. However, the jet candidates are used to vetoing event also, which is called bad-jet veto. Bad jet due to the noise in the calorimeter or cosmic ray can be a jet candidate. The quality of the event which contains such object cannot be guaranteed. Therefore, such event is vetoed by tagging the object as bad jet [57]. If such object exists even after the overlap removal, which is described in Section 4.2.4, the event is removed from the analysis.

The other type of tag for jet used in this analysis is the b-jet tagging, which is used in Section 5.3.7. A jet originating from b-hadron decay, which is called b-jet, can be identified using its characteristics. In ATLAS experiment, following three types of inputs are used [58]:

- Secondary Vertex: Due to its relatively long life time, the decay point of b-hadron is not matching to the primary vertex. Such point is called secondary vertex. In the b-jet tagging algorithm, the secondary vertex is reconstructed, and its characteristics is used for the tagging.
- Impact Parameter: Even without finding the secondary vertex, tracks in the b-jet have different characteristics, since some of them are originating from secondary vertex. Based on this approach, likelihood of b-jet or other jets are calculated using impact parameter of tracks and used for the tagging.
- Decay Chain Multi-Vertex Algorithm (JetFitter [59]): The JetFitter algorithm tries to reconstruct the topological structure from the priority vertex to b-hadron and c-hadron. The reconstructed information are used for the tagging.

Using the inputs discussed above, a boosted decision tree algorithm to discriminate b-jet from other jets are trained. The trained algorithm, called MV2c20[*2], provide the output shown in Figure 4.4. In this analysis, the working point providing 77% efficiency for b-jet is used. This tag is used in Section 5.3.7

4.2.4 Overlap removal

Just after the reconstruction of the physics objects described above, some of the objects can be double counted as several physics objects. One possible reason of such reconstruction is misidentification for one of the object. Muon track can be misidentified as an electron or a converted photon. Converted photon can be misidentified as an electron. Energy deposit on the calorimeter by electron and photon can be misidentified as a jet. When one of the reconstructed object is jet, there is another possibility that overlapped object is part of jet. Muon, photon, and electron can be a part of jet. Such overlap is removed in the following order in this analysis:

- If an electron and a muon share a track, it is used for a track for the muon.
- If a jet and an electron are found within $\Delta R < 0.2$, the object is interpreted as an electron and the overlapping jet is removed from the event.
- If a jet and an electron are found within $0.2 < \Delta R < 0.4$, the object is interpreted as jet and the electron is removed.
- If a jet and a muon are found within $\Delta R < 0.4$, the object is interpreted as jet and the muon is removed from the event.
- If a jet and a photon are found within $\Delta R < 0.2$ the object is interpreted as photon and the

[*2] The name came form the composition of background sample for the training, which is 20% c-jets and 80% light-flavour jets.

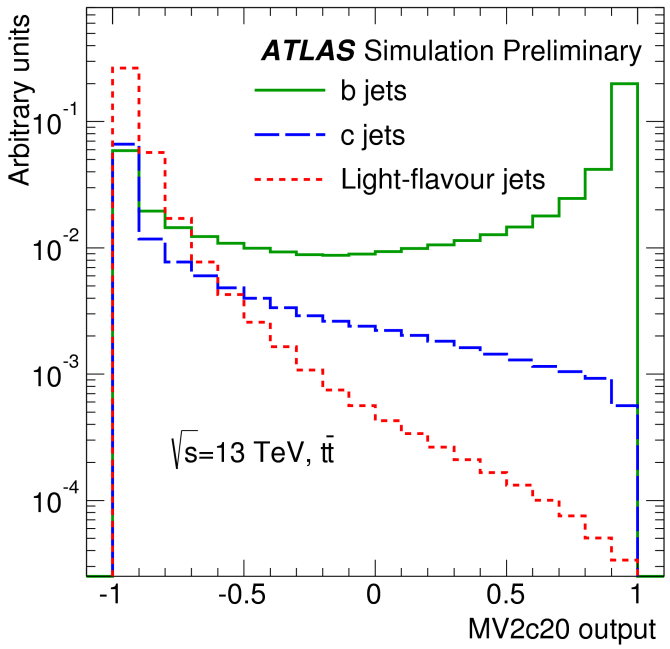

Figure4.4 The MV2c20 output for b- (solid green), c- (dashed blue) and light-flavour (dotted red) jets in tanti-t events. The figure is cited from [58].

overlapping jet is removed from the event.

- If a jet and a photon are found within $0.2 < \Delta R < 0.4$, the object is interpreted as a jet and the overlapping photon is removed from the event.
- If a electron and a photon are found within $\Delta R < 0.4$, the object is interpreted as electron and the overlapping photon is removed from the event.
- If a muon and a photon are found within $\Delta R < 0.4$, the object is interpreted as muon and the overlapping photon is removed from the event.

4.2.5 Missing transverse energy

After the overlap removal, one more physics object is reconstructed, which is the missing transverse energy ($\mathbf{E}_{\mathrm{T}}^{\mathrm{miss}}$). Because of the momentum conservation in transverse plane, the total momentum or the invisible particles, can be estimated by negative vector sum of the detected objects. In this analysis, a neutrino decayed from W boson and two $\tilde{\chi}_1^0$ are expected as sources of $\mathbf{E}_{\mathrm{T}}^{\mathrm{miss}}$.

$\mathbf{E}_{\mathrm{T}}^{\mathrm{miss}}$ is defined as following:

$$(\mathbf{E}_{\mathrm{T}}^{\mathrm{miss}})_{x(y)} = (\mathbf{E}_{\mathrm{T}}^{\mathrm{miss}})_{x(y)}^{e} + (\mathbf{E}_{\mathrm{T}}^{\mathrm{miss}})_{x(y)}^{\gamma} + (\mathbf{E}_{\mathrm{T}}^{\mathrm{miss}})_{x(y)}^{\mathrm{jet}} + (\mathbf{E}_{\mathrm{T}}^{\mathrm{miss}})_{x(y)}^{\mu} + (\mathbf{E}_{\mathrm{T}}^{\mathrm{miss}})_{x(y)}^{\mathrm{Soft\ Term}}, \quad (4.4)$$

where each term is computed from the negative vector sum of calibrated reconstructed objects in the respective category. The last term is for objects called soft term, which is calculated from the reconstructed tracks which are not associated to any physics object [60, 61].

4.2.6 Skimming sample

For establishment of the analysis procedure, collected data is expected to be analyzed several times. In order to analyze data efficiently, skimming of events is performed. The skim has been performed just after the reconstruction of physics object candidates, before the selection of them. At that stage, the events not passing following criteria are removed.

- The dataset is included in the good run list, which is the list of good quality dataset commonly used in the ATLAS experiment.
- The event is associated with a primary vertex. Otherwise the event can come from cosmic muon or noise.
- The event is not used if one of the following problems occurred:
  - Noise burst at the LAr calorimeter.
  - Recovery from the trip of the low voltage power supply for the tile calorimeter.
  - DAQ had been done during the recovery procedure for single event upsets in the SCT.
- The event dose not include more than one muon with a $|z_0| > 1\,\text{mm}$ or $|d_0| > 0.2\,\text{mm}$, which is likely cosmic muon.
- The event passes at least one of following selections[*3]:
  - The event contains more than one photon candidate with greater than 30 GeV transverse energy.
  - The event contains at least one photon candidate with greater than 30 GeV transverse energy and at least one electron candidate with greater than 30 GeV momentum.
  - The event contains more than one electron candidate with greater than 30 GeV momentum.

The events passing the criteria above are used in the analysis described in the following chapters.

[*3] These selections are applied as loose pre-selections.

Chapter 5

Event selection

As described in Section 1.2, the relative yield of new physics to the SM physics is expected to be small. Therefore, it is important to suppress the contributions of the SM events, while keeping acceptance of the contributions of the new physics.

In this chapter, the signal region is defined. At first, overall development of the analysis procedures are overviewed in Section 5.1. In Section 5.2, the signatures of the signals and the backgrounds are overviewed. Based on the described signatures, the signal region is defined in Section 5.3.

5.1 Overview of development of analysis procedure

At first, the signal region is defined based on the previous study. The selection criteria used in early stage of the development are denoted as "early selections". Using the early selections, procedures to evaluate yields are established, as described in the next chapter. Then rough uncertainties on the evaluated yields are evaluated. Using those procedures and rough uncertainties, the signal region is further optimized, as described in Chapter 7. After the optimization, some selections and samples are changed. The selections used after this change are denoted as "final selections". The difference between the early selections and the final selections are evaluated in Section 7.4.2. With the final selections and the optimized signal regions, uncertainties are re-evaluated, then the expected upper limit is evaluated in Chapter 8.

5.2 Overview of event signatures

As described in Figure 1.7, two photons, one lepton and the missing transverse energy ($E_{\mathrm{T}}^{\mathrm{miss}}$) are expected in the final state of the signal. Therefore, exactly two photons, exactly one lepton, and a requirement on the missing transverse energy, which is $E_{\mathrm{T}}^{\mathrm{miss}} > 40\,\mathrm{GeV}$, are requested as the basic selections. Only electron or muon is considered as a lepton in the final state in this analysis. In the case of tau, it decays immediately. Only when tau decays into leptons, the event is used as signal in this analysis.

The backgrounds which can pass the basic requirements are classified into two types, as introduced in Section 3.2.1. The backgrounds including a SM higgs particle within their process is classified as peaking background. The other type of the backgrounds is non-peaking backgrounds. Since those two types of the backgrounds have different signatures, those are considered separately.

5.2.1 Peaking backgrounds

The peaking backgrounds are mainly from W with associated SM higgs, which is called SM Wh. In contrast to the large missing transverse energy in the signal events, the missing transverse energy in the peaking backgrounds events is relatively small due to lack of the LSP particles. Therefore, the variables related to the missing transverse energy are the key to suppress peaking backgrounds.

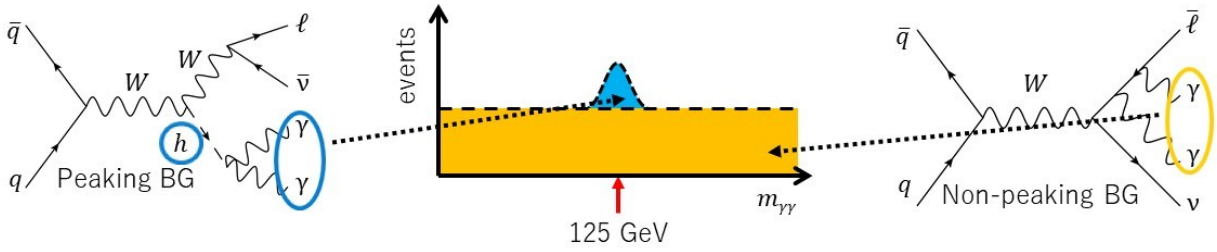

Figure5.1 Image of $m_{\gamma\gamma}$ distributions. In contrast to the peaking backgrounds and signals (shown as a blue region) which have $m_{\gamma\gamma}$ close to 125 GeV because of the higgs particles within their processes, the non-peaking backgrounds (shown as an orange region) have wide range of $m_{\gamma\gamma}$.

5.2.2 Non-peaking backgrounds

The non-peaking backgrounds are mainly from W or Z associated with diphoton. Due to the same reason with the peaking backgrounds, the non-peaking background events have relatively small missing transverse energy.

Additionally, invariant mass of the diphoton system ($m_{\gamma\gamma}$) is an important variable to suppress non-peaking backgrounds. Figure 5.1 shows a conceptual drawing of $m_{\gamma\gamma}$ distribution. As shown in the figure, for the signal and the peaking backgrounds, two photons are from the SM higgs decay. Therefore, reconstructed $m_{\gamma\gamma}$ is close to the mass of the SM higgs particle (125 GeV). On the other hand, $m_{\gamma\gamma}$ of the non-peaking background events may not be close to the mass of the SM higgs particle. Therefore, the non-peaking backgrounds can be suppressed by the cut on $m_{\gamma\gamma}$.

5.3 Signal region definitions

After the basic selection described in the previous section, further cuts are applied to reduce backgrounds. In this section, the requirements for the signal region are described.

In order to show their discrimination power, the distributions of discriminating variables are shown in the following sub section. All the distributions shown in this section are after the basic selections and the $m_{\gamma\gamma}$ requirement, which is $105 < m_{\gamma\gamma} < 160$ GeV. The region $120 < m_{\gamma\gamma} < 130$ GeV is called Higgs window and it blinded. The region out of the Higgs window are called sideband region. Since only the higgs window is used as the signal region, the contributions of the non-peaking backgrounds, which is distributed in both the sideband and higgs window, are scaled by 10/55 which is the ratio of $m_{\gamma\gamma}$ width between the higgs window and the sideband window[*1]. Detail about the window width is described in Section 5.3.5.

In this analysis, most of the requirements are the same with the 8 TeV analysis [19]. Each requirement threshold is reconsidered by using distributions shown in this section, and some of them are updated to improve the sensitivity to the signal.

5.3.1 Signal focus points

Most of the kinematic distributions of signals depend on the assumed mass of LSP and NLSP. In the optimization and the evaluation of the backgrounds steps, three focus points are used.

One of the focus points is a signal assuming $(m_{\tilde{\chi}_1^\pm,\tilde{\chi}_2^0}, m_{\tilde{\chi}_1^0}) = (150, 0)$ GeV, called low-mass signal.

[*1] For this scaling, it is assumed that non-peaking backgrounds have linear $m_{\gamma\gamma}$ shape. This is validated in Section 6.1.2.

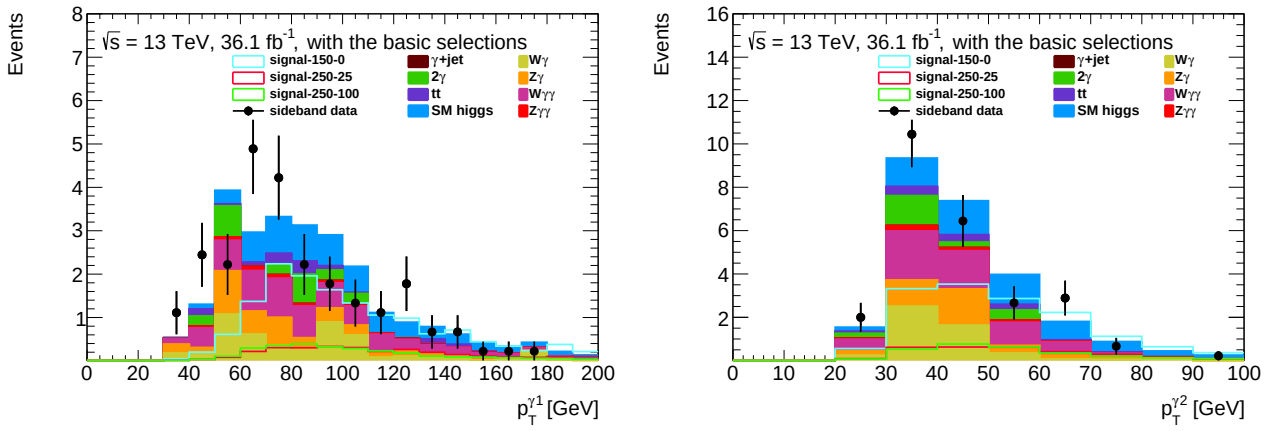

Figure5.2 $p_{\mathrm{T}}^{\gamma 1}$ (left) and $p_{\mathrm{T}}^{\gamma 2}$ (right) distributions with the basic selections, which are exactly two photons, exactly one lepton, and $E_{\mathrm{T}}^{\mathrm{miss}} > 40\,\mathrm{GeV}$. Contributions of non-peaking backgrounds are scaled by 10/55, which is the ratio of $m_{\gamma\gamma}$ width between the higgs window and the sideband window. Data (black points) are shown only for those distributed out of higgs window, and are scaled by 10/45. Shown uncertainty is only statistical error on sideband data.

This signal had been excluded by the 8 TeV analysis. This point is used to ensure that the significance in low mass parameter space of the model is kept.

The other type of focus points are called high-mass signals. Those are signals assuming $(m_{\tilde{\chi}_1^\pm,\tilde{\chi}_2^0}, m_{\tilde{\chi}_1^0}) = (250, 25)$ GeV and $(m_{\tilde{\chi}_1^\pm,\tilde{\chi}_2^0}, m_{\tilde{\chi}_1^0}) = (250, 100)$ GeV. Those two signals are chosen to evaluate typical signatures of signal event in high mass parameter space of the model. The optimization has been performed to improve sensitivity to the high-mass signals.

5.3.2 Photon selection

The two photons passing the object selections described Section 4.2.1 are sorted by their transverse momentum, and called leading photon or sub-leading photon. Figure 5.2 shows their momentum. Unless otherwise noted, the plots shown in this section are after the basic selection:

- Exactly two photons.
- Exactly one lepton.
- $E_{\mathrm{T}}^{\mathrm{miss}} > 40$ GeV

Regarding data, for those distributed in the sideband windows are shown, and for those distributed in the Higgs window are blinded. Then, the contributions of the non-peaking backgrounds are scaled by $\frac{10}{55} = \frac{\text{width of the higgs window in GeV}}{\text{width of the sideband in GeV}}$. Also, the contributions of sideband data are scaled by $\frac{10}{55-10} = \frac{\text{width of the higgs window in GeV}}{\text{width of the sideband in GeV} - \text{width of the blinded Higgs window in GeV}}$. The contributions of peaking backgrounds are merged as "SM higgs", and all the backgrounds are shown as a stacked histogram. Regarding uncertainty, only statistical fluctuation of sideband data are shown as black bars, which are calculated based on Poisson function.

As described in Section 3.1.1, diphoton trigger is used to collect data with $p_{\mathrm{T}}^{\gamma 1} > 35\,\mathrm{GeV}$ and $p_{\mathrm{T}}^{\gamma 2} > 25\,\mathrm{GeV}$. As described in Section 4.2.6, event must pass at least one of the conditions for skimming described below;

- Event contains more than one photon candidate with greater than 30 GeV momentum.
- Event contains at least one photon candidate with greater than 30 GeV momentum and at least one electron candidate with greater than 30 GeV momentum.
- Event contains more than one electron candidate with greater than 30 GeV momentum.

Therefore, events shown in Figure 5.2 are only passing the pre-selections on photon momentum

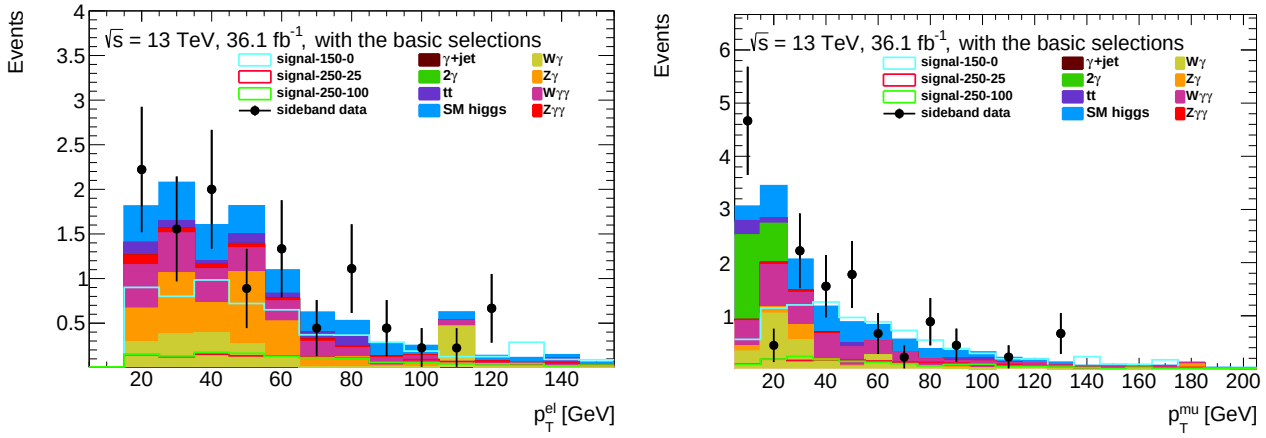

Figure5.3 p_{T}^{e} (left) and p_{T}^{μ} (right) distributions with the basic selections, which are exactly two photons, exactly one lepton, and $E_{\mathrm{T}}^{\mathrm{miss}} > 40\,\mathrm{GeV}$. Contributions of non-peaking backgrounds are scaled by 10/55, which is the ratio of $m_{\gamma\gamma}$ width between the higgs window and the sideband window. Data (black points) are shown only for those distributed out of higgs window, and are scaled by 10/45. Shown uncertainty is only statistical error on sideband data.

described above.

In the 8 TeV analysis, $p_{\mathrm{T}}^{\gamma 2} > 20\,\mathrm{GeV}$ was applied [19]. The right plot in Figure 5.2 shows that signals are distributed to lower momentum region. Therefore, it is recommended to set the threshold for $p_{\mathrm{T}}^{\gamma 2}$ as low as possible to keep signal acceptance.

For the leading photon, $p_{\mathrm{T}}^{\gamma 1} > 40\,\mathrm{GeV}$ is applied as in the 8 TeV analysis. For the sub-leading photon, two types of selection thresholds are used in this analysis. When the optimization study described in Section 7 and the validations of the method to evaluate non-peaking backgrounds described Section 6.1 are performed, $p_{\mathrm{T}}^{\gamma 2} > 27\,\mathrm{GeV}$ are applied. However, this requirement can be a source of bias since this threshold is lower than the threshold applied at the skimming step described above. Therefore, the threshold for $p_{\mathrm{T}}^{\gamma 2}$ is increased to 31 GeV after those studies. This is discussed in more detail in Section 7.4.2. The requirements before changing the threshold for $p_{\mathrm{T}}^{\gamma 2}$ are noted as the early selections, and the requirements after the change are noted as the final selections.

5.3.3 Lepton selection

Figure 5.3 shows the momentum distributions of electrons and muons. For both leptons, 25 GeV is applied as the threshold for their transverse momentum. The isolation criterion for the electron applied in the object selection described in Section 4.2.1 is tuned to provide more than 95% of efficiency for $Z \to e^{+}e^{-}$ events from this threshold.

5.3.4 Missing transverse energy selection

Figure 5.4 shows the missing transverse energy distribution. As described in Section 5.2, the distribution is after applying $E_{\mathrm{T}}^{\mathrm{miss}} > 40\,\mathrm{GeV}$ as a part of the basic selections.

Figure 5.4 suggests that both type of the backgrounds can be suppressed by increasing threshold for $E_{\mathrm{T}}^{\mathrm{miss}}$ as expected. However, the acceptance for the low-mass signal decreased with higher threshold for $E_{\mathrm{T}}^{\mathrm{miss}}$. Therefore, further requirement on $E_{\mathrm{T}}^{\mathrm{miss}}$ is not applied in the signal region requirements. Instead, this discriminating variable is used for the optimization, which is dividing the signal region to improve significance, described in Chapter. 7

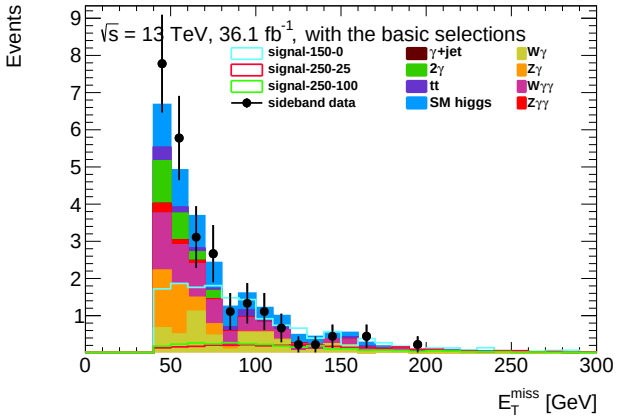

Figure5.4 Missing transverse energy distribution with the basic selections, which are exactly two photons, exactly one lepton, and $E_{\mathrm{T}}^{\mathrm{miss}} > 40\,\mathrm{GeV}$. Contributions of non-peaking backgrounds are scaled by 10/55, which is the ratio of $m_{\gamma\gamma}$ width between the higgs window and the sideband window. Data (black points) are shown only for those distributed out of higgs window, and are scaled by 10/45. Shown uncertainty is only statistical error on sideband data.

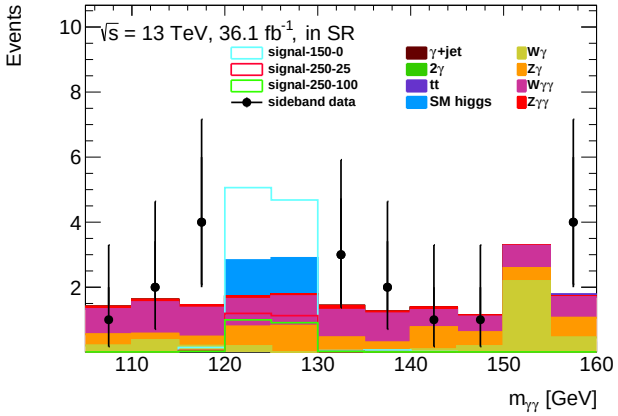

Figure5.5 $m_{\gamma\gamma}$ distribution with the signal region selections except for $m_{\gamma\gamma}$ cut, which are summarized in Table 5.1. Scaling applied to the other plot is not applied to this plot. Data (black points) are shown only for those distributed out of higgs window. Data distributed in the Higgs window are blinded. Shown uncertainty is only statistical error on sideband data.

5.3.5 Diphoton invariant mass

As described in Section 5.2.2, the invariant mass of the diphoton system ($m_{\gamma\gamma}$) is an important variable to suppress the non-peaking backgrounds. $m_{\gamma\gamma}$ is defined as following:

$$m_{\gamma\gamma} = \sqrt{2E_T^{\gamma 1}E_T^{\gamma 2}(\cosh\Delta\eta - \cos\Delta\phi)}$$

Figure 5.5 shows $m_{\gamma\gamma}$ distribution. For this figure, not the basic selection but the inclusive singal regon requirements summarized in Table 5.1 are applied. Scaling factors on non-peaking backgrounds and sideband data are not applied. Data distributed in the Higgs window are blinded.

As described at the beginning of Section 5.3, $105 < m_{\gamma\gamma} < 160$ GeV is required for the sideband region, and $120 < m_{\gamma\gamma} < 130$ GeV is required for the signal region. [*2]

[*2] The sideband range is validated in Section 6.1.2 in detail.

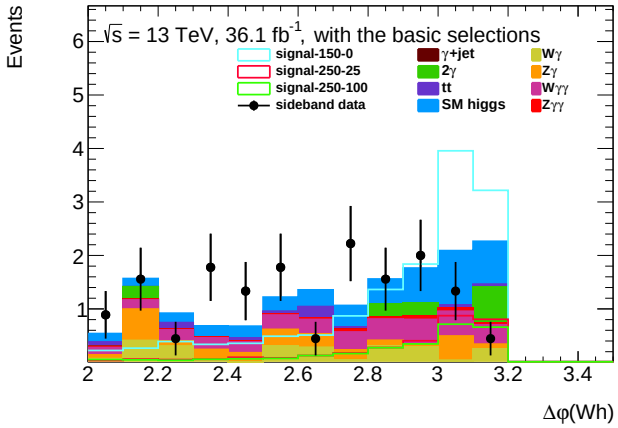

Figure5.6 $\Delta\phi(\mathrm{W},\mathrm{h})$ distribution with the basic selections, which are exactly two photons, exactly one lepton, and $E_{\mathrm{T}}^{\mathrm{miss}} > 40\,\mathrm{GeV}$. Contributions of non-peaking backgrounds are scaled by 10/55, which is the ratio of $m_{\gamma\gamma}$ width between the higgs window and the sideband window. Data (black points) are shown only for those distributed out of higgs window, and are scaled by 10/45. Shown uncertainty is only statistical error on sideband data.

The non-peaking backgrounds are uniformly distributed [*3] in the sideband region as shown in Figure 5.5. In contrast, the signals and the peaking backgrounds are distributed only in the higgs window. Therefore, the ratio between higgs window width and sideband window width is applied as a scaling factor to evaluate the contribution of the non-peaking backgrounds in the higgs window for the kinematic distribution except for $m_{\gamma\gamma}$ distribution.

5.3.6 W boson and higgs systems

The "W boson object" is reconstructed from the missing transverse energy and the lepton [*4]. The higgs object is reconstructed from the two photons. Since all objects in the final states of the signals and the SM Wh can be reconstructed as a higgs object or a W object, those two objects are expected to fly away back-to-back in lab frame. On the other hand, additional objects and miss-reconstructed objects are expected in final state of non-peaking backgrounds. Therefore, the angular distribution between the W object and the higgs object can be smaller than the case of the signal and SM Wh.

In order to suppress the non-peaking backgrounds using the angular information, $\Delta\phi(\mathrm{W},\mathrm{h})$ is defined as ϕ separation between the W object and the higgs object. Figure 5.6 shows the $\Delta\phi(\mathrm{W},\mathrm{h})$ distribution. As expected above, the signals and the peaking backgrounds are distributed in high $\Delta\phi(\mathrm{W},\mathrm{h})$ region. And distributions of the non-peaking backgrounds are relatively flat. As a signal region requirement, $\Delta\phi(\mathrm{W},\mathrm{h}) > 2.25$ is applied, as applied in the 8 TeV analysis.

Because of the contribution of the LSPs to the missing transverse energy, reconstructed masses of the W object and a photon object can be discriminating variables. In this analysis, the transverse masses reconstructed with the missing transverse energy, the lepton, and one of the photons are used as the discriminating variables in the signal region requirement. The transverse mass reconsidered with the missing transverse energy and the lepton without using photon objects is used for the optimization described in Chapter 7. The transverse mass reconstructed with leading photon (γ_1) is noted as $M_{\mathrm{T}}^{\mathrm{W}\gamma 1}$. And the transverse mass reconstructed with sub-leading photon (γ_2) is noted as $M_{\mathrm{T}}^{\mathrm{W}\gamma 2}$. The transverse mass reconstructed without using photon objects is noted as $M_{\mathrm{T}}^{\mathrm{W}}$. Definition

[*3] The shape of $m_{\gamma\gamma}$ distribution of the non-peaking background is validated in Section 6.1.2 in detail.
[*4] W object is not always truth W boson. In the case of signal, it includes two LSPs.

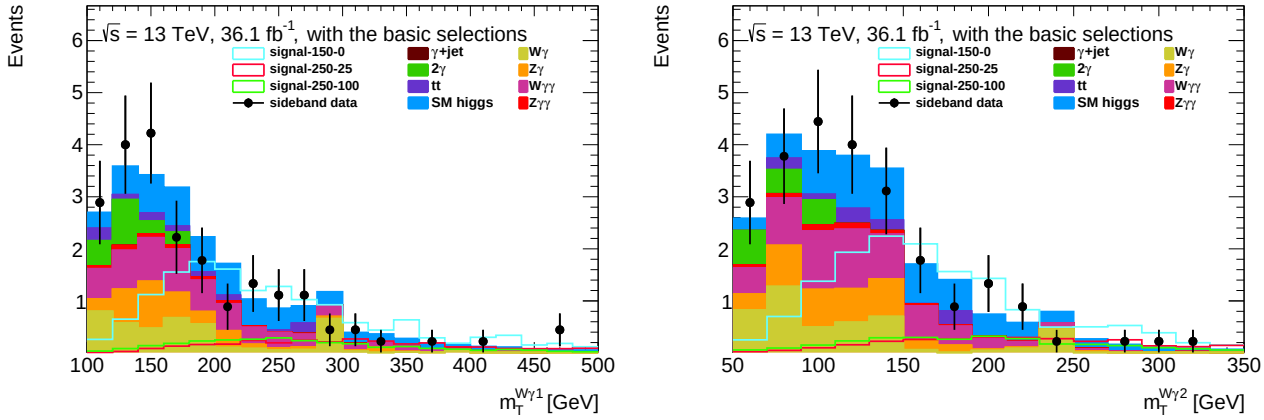

Figure5.7 $M_{\mathrm{T}}^{\mathrm{W}\gamma 1}$ (left) and $M_{\mathrm{T}}^{\mathrm{W}\gamma 2}$ (right) distributions with the basic selections, which are exactly two photons, exactly one lepton, and $E_{\mathrm{T}}^{\mathrm{miss}} > 40\,\mathrm{GeV}$. Contributions of non-peaking backgrounds are scaled by 10/55, which is the ratio of $m_{\gamma\gamma}$ width between the higgs window and the sideband window. Data (black points) are shown only for those distributed out of higgs window, and are scaled by 10/45. Shown uncertainty is only statistical error on sideband data.

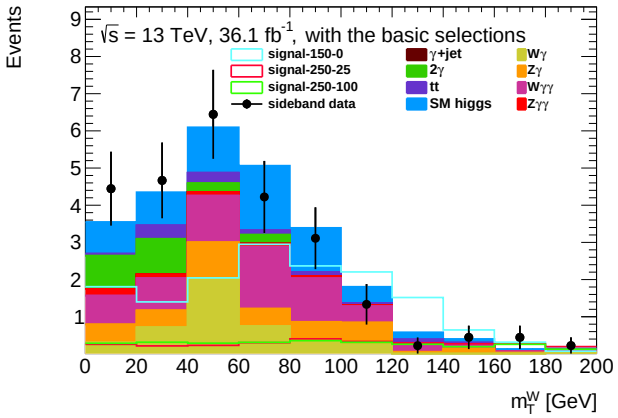

Figure5.8 $M_{\mathrm{T}}^{\mathrm{W}}$ distribution with the basic selections, which are exactly two photons, exactly one lepton, and $E_{\mathrm{T}}^{\mathrm{miss}} > 40\,\mathrm{GeV}$. Contributions of non-peaking backgrounds are scaled by 10/55, which is the ratio of $m_{\gamma\gamma}$ width between the higgs window and the sideband window. Data (black points) are shown only for those distributed out of higgs window, and are scaled by 10/45. Shown uncertainty is only statistical error on sideband data.

of those transverse masses are following:

$$M_T^{W\gamma i} = \sqrt{2E_T^{\gamma i}E_{\mathrm{T}}^{\mathrm{miss}}(1-\cos\Delta\phi_{\gamma i,E_{\mathrm{T}}^{\mathrm{miss}}}) + 2E_T^{\ell}E_{\mathrm{T}}^{\mathrm{miss}}(1-\cos\Delta\phi_{\ell,E_{\mathrm{T}}^{\mathrm{miss}}}) + 2E_T^{\gamma i}E_T^{\ell}(1-\cos\Delta\phi_{\gamma i,\ell})} \tag{5.1}$$

$$M_{\mathrm{T}}^{\mathrm{W}} = \sqrt{2E_T^{\ell}E_{\mathrm{T}}^{\mathrm{miss}}(1-\cos\Delta\phi_{\ell,E_{\mathrm{T}}^{\mathrm{miss}}})} \tag{5.2}$$

Figure 5.7 shows the $M_{\mathrm{T}}^{\mathrm{W}\gamma 1}$ distribution and the $M_{\mathrm{T}}^{\mathrm{W}\gamma 2}$ distribution respectively. In this analysis, $M_{\mathrm{T}}^{\mathrm{W}\gamma 1} > 150$ GeV and $M_{\mathrm{T}}^{\mathrm{W}\gamma 2} > 80$ GeV are used for the signal region requirements, as applied in the 8 TeV analysis. Figure 5.8 is the $M_{\mathrm{T}}^{\mathrm{W}}$ distribution.

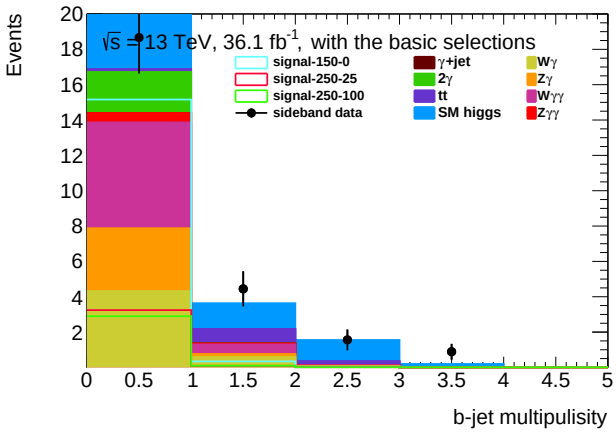

Figure5.9 Distribution of the number of b-jets with the basic selections, which are exactly two photons, exactly one lepton, and $E_{\mathrm{T}}^{\mathrm{miss}} > 40\,\mathrm{GeV}$. Contributions of non-peaking backgrounds are scaled by 10/55, which is the ratio of $m_{\gamma\gamma}$ width between the higgs window and the sideband window. Data (black points) are shown only for those distributed out of higgs window, and are scaled by 10/45. Shown uncertainty is only statistical error on sideband data.

5.3.7 B-jet

Figure 5.9 shows the distribution of the number of b-jets. Most of the signal events have no b-jets, while non-negligible background events have one or more b-jet. Non-peaking background events with b-jets are mainly from $t\bar{t}$ events, and peaking background events with b-jets are mainly from $t\bar{t}h$ events.

The difference between the signal and two type of the backgrounds suggests that significance can be improved by vetoing events with b-jets (b-jet veto). The improvement with the b-jet veto is estimated with the asymptotic formulae of the expected significance Z assuming the nominal signal hypothesis [62] and only statistical uncertainty, defined as

$$Z = \sqrt{2((s+b)\ln(1+\frac{s}{b}) - s)},$$

where s is the expected yields of the signal and b is the expected yields of all the backgrounds. For s, high-mass focus points were assumed.

From the calculation of significance Z using the yields evaluated by MCs, $\sim 10\%$ improvement of the significance is evaluated while keeping the acceptance of the signal yields. Therefore, the b-jet veto is introduced into signal region requirements.

5.3.8 Subdivision of the signal region

In Table 5.1, all the requirements for the signal region are summarized.

As a result of the optimization described in Chapter 7, the signal region defined above are subdivided to four subsets noted from SRa to SRd. Since those subsets are mentioned in the following chapter, only the definitions of those subsets are shown in the Table 5.2 The subdividing thresholds are shown in Figure 5.10.

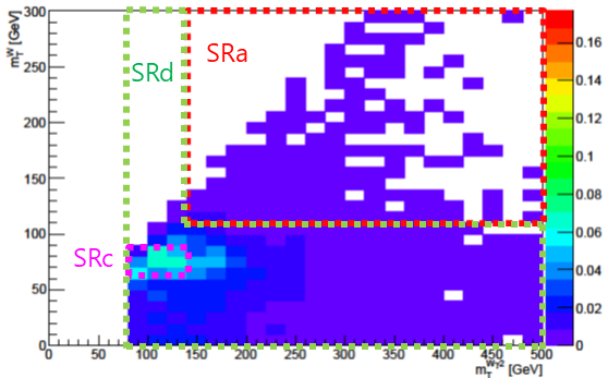

Figure5.10 Subdivided signal regions in ($M_{\mathrm{T}}^{\mathrm{W}\gamma 2}$, $M_{\mathrm{T}}^{\mathrm{W}}$). z axis showns the yield of the peaking background. SRb, which is not shown in the figure, is complement to SRa + SRc.

Table5.1 Requirements of the inclusive signal region.

Number of photon $p_{\mathrm{T}}^{\gamma 1}$ $p_{\mathrm{T}}^{\gamma 2}$	Exactly two > 40 GeV > 27 GeV (> 31 GeV after the optimization)
Number of leptons p_{T}^{e} or p_{T}^{μ}	Exactly one (electron or muon) > 25 GeV
$E_{\mathrm{T}}^{\mathrm{miss}}$	> 40 GeV
$m_{\gamma\gamma}$	> 120 GeV and < 130 GeV
$\Delta\phi(\mathrm{W},\mathrm{h})$ $M_{\mathrm{T}}^{\mathrm{W}\gamma 1}$ $M_{\mathrm{T}}^{\mathrm{W}\gamma 2}$	> 2.25 > 150 GeV > 80 GeV
Number of b-jets	Exactly zero

Table5.2 Definitions of the subsets of signal region. SRb and SRc are subsets of SRd.

SRa	$M_{\mathrm{T}}^{\mathrm{W}\gamma 2} > 140$ GeV and $M_{\mathrm{T}}^{\mathrm{W}} > 110$ GeV
SRb	$M_{\mathrm{T}}^{\mathrm{W}\gamma 2} < 140$ GeV or $M_{\mathrm{T}}^{\mathrm{W}} < 110$ GeV excluding SRc
SRc	$M_{\mathrm{T}}^{\mathrm{W}\gamma 2} < 140$ GeV and $60 < M_{\mathrm{T}}^{\mathrm{W}} < 90$ GeV
SRd	$M_{\mathrm{T}}^{\mathrm{W}\gamma 2} < 140$ GeV or $M_{\mathrm{T}}^{\mathrm{W}} < 110$ GeV

Chapter 6

Signal and background modeling

The signal region defined in the previous chapter is further optimized in the next chapter. For the optimization, reliable yields expectation of the signal and background are needed. In this chapter, the procedures to estimate the yields of signal and background are described. For the non-peaking backgrounds, the yields are evaluated using data-driven method, as described in Section 6.1. The others are evaluated by MCs, as described in Section 6.2.

6.1 Non-peaking Backgrounds

The non-peaking backgrounds are widely distributed in signal region and sideband regions. Thus, the yields of the non-peaking backgrounds in the signal region can be estimated by interpolating the shape of the distribution from the sideband region.

6.1.1 Yields evaluation method

As shown in Figure 5.5, the sideband region is dominated by non-peaking backgrounds. Assuming no contribution of the peaking backgrounds and the signal to the sideband region and continuous $m_{\gamma\gamma}$ shape of the non-peaking backgrounds, yields of non-peaking backgrounds in the signal region can be evaluated by using data distributed in the sideband region. Because of the limited statistics in the sideband region, a simple assumption is chosen as the shape of $m_{\gamma\gamma}$ distribution, which is the constant function[*1]

The yields are evaluated as following. At first, data in sideband region of each subset of the signal region are fitted with a constant function. The fitted distributions are shown in Figure 6.1 and Figure 6.2. From the fitted functions, the yields in the subsets are evaluated. Since all the $m_{\gamma\gamma}$ distributions are plotted in 5 GeV bin width, the yields in the 10 GeV of higgs window can be evaluated by a twice the fitted constant value. The results are shown in Table 6.1. In the table, the statistical uncertainties are also shown, which are evaluated in Section 8.1. The results are with the final selections.

Table6.1 Estimated yields of the non-peaking backgrounds with statistical uncertainty, by fitting constant function to the $m_{\gamma\gamma}$ sideband data, for each subset of the signal region. The yields expected from MCs and their statistical uncertainty are aslo shown.

Subsets of the signal region	Estimated yields from the fitting	MC expectation
SRa	0.22 ± 0.22	0.41 ± 0.11
SRb	2.44 ± 0.67	2.02 ± 0.41
SRc	0.89 ± 0.45	0.86 ± 0.42
SRd	3.33 ± 0.90	2.88 ± 0.59

[*1] This assumption is discussed in Section 6.1.2.

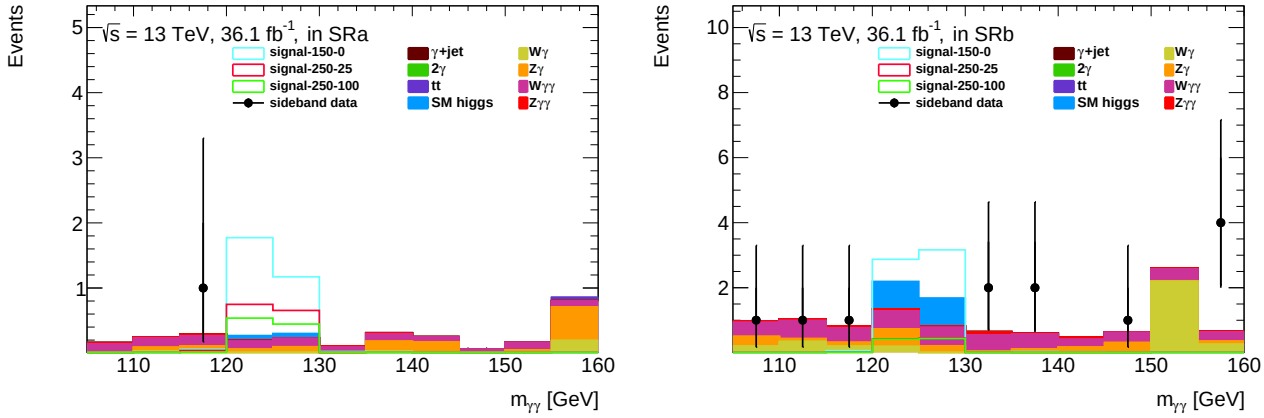

Figure6.1 $m_{\gamma\gamma}$ distributions in SRa (left) and in SRd (right). Data (black points) are shown only for those distributed out of higgs window. Shown uncertainty is only statistical error on sideband data.

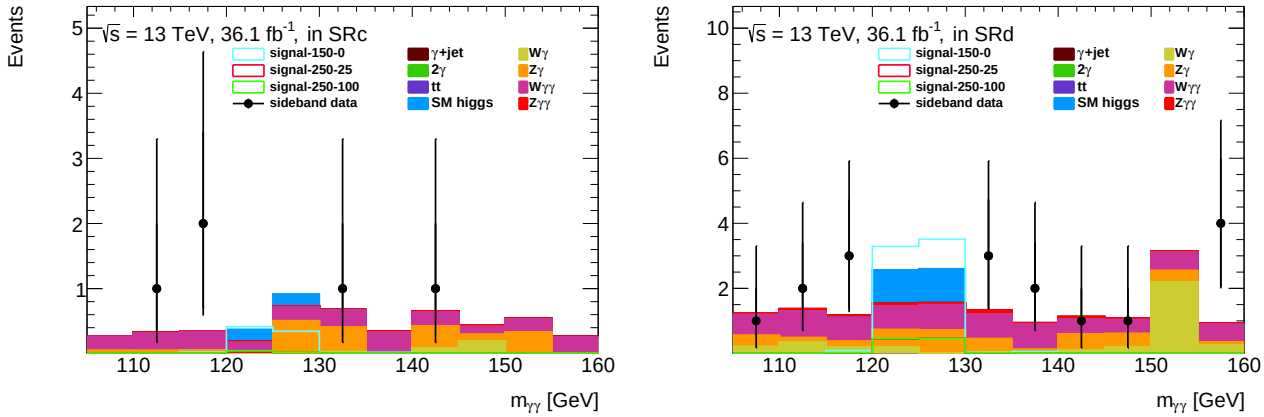

Figure6.2 $m_{\gamma\gamma}$ distributions in SRc (left) and in SRd (right). Data (black points) are shown only for those distributed out of higgs window. Shown uncertainty is only statistical error on sideband data.

6.1.2 Validations of the method

Fitting function dependence

In order to verify about the $m_{\gamma\gamma}$ shape, the study is performed with toy samples, which is the pseudo data generated under simple assumptions. This study is performed with the early selections. Due to lack of statistics in the subsets of the signal region, the study is performed only for the inclusive signal region.

For the study, two types of assumptions are considered; the genuine shape of the non-peaking backgrounds do not depend on the $m_{\gamma\gamma}$ (constant function), or it has linear dependence on $m_{\gamma\gamma}$ (linear function). At first, observed sideband data are fitted by the assumed function. Because of the large statistical fluctuation of the sideband data, the slope of the linear function is evaluated by the MC distributions, and the function is scaled to the sideband data while fixing the slope. Then, the fitted functions are assumed as genuine probability density function. Based on the two fitted functions, two types of toy samples are generated. For this study, 10,000 of toy samples for each assumption are generated.

After generating the toy samples, those are re-fitted with a constant and a linear function in the same manner to evaluate expected yield for each toy sample. Finally, mean and RMS of the

re-evaluated yields for each type of toy samples are calculated. The results are shown in Table 6.2. The results suggest that there are no dependence on the assumption of the shape, considering the large statistical error.

Fitting range dependence

Since the expected yields rely on the distribution of the data in sideband, they could be affected by the definition of sideband range. In order to verify the effect, several fittings to the data in the inclusive signal region has been performed with various definitions of the sideband range. This study is performed with the early selections.

Table 6.3 shows the results. Although small tendency can be seen in the results, the effect is much smaller than the statistical uncertainty. Therefore, this dependence is not considered further.

Leakage from signal region

The studies described above are based on the assumption that all the data distributed in the sideband region are non-peaking backgrounds. This assumption is satisfied if there are no leakage of the signal or the peaking backgrounds from the signal region. It is confirmed with the $m_{\gamma\gamma}$ distribution shown in Figure 5.5. From the distribution, the evaluated leakages to sideband region are smaller than 0.3 events. The leakages are much smaller than the yields of the non-peaking backgrounds expected by MCs. Therefore, the possibilities that the leakages affect the fitting results or the validation studies are negligible and not considered here.

6.1.3 Further validation about $m_{\gamma\gamma}$ shape

The validations described in the previous subsection had been performed in early stage of the development of analysis procedure. In final stage of the development, further study about $m_{\gamma\gamma}$ has been performed because of mild "slopes" around higgs window shown in Figure 5.5. The slopes seem to be wide tails leaked from the higgs window. It is expected to be statistical fluctuation, so the study is performed to guarantee that expectation. This study is performed with the final selections.

If the slopes are due to statistical fluctuation, similar fluctuation may be seen in other region. Since the used range of $m_{\gamma\gamma}$ is too narrow for discussion, $m_{\gamma\gamma}$ requirement is relaxed from [105, 160] GeV to [0,300] GeV. Because of wide range of $m_{\gamma\gamma}$, bin width is changed from 5 GeV to 10 GeV. The distribution is shown in Figure 6.3 As shown in the figure [*2] , data points are fluctuated

Table6.2 Results of the toy study. The nominal assumption is shown in third row. The differences between evaluated yields are small comparing to their error.

Toy assumption	fitted functions	evaluated yields
constant	linear	4.70 ± 1.00
linear	linear	4.70 ± 1.00
constant	constant	4.88 ± 1.03
linear	constant	4.89 ± 1.03

Table6.3 Results of the sideband range study. The nominal range is shown in third row. The differences between evaluated yields are small comparing to the error on the nominal yield.

Sideband range	evaluated yields
$110 < m_{\gamma\gamma} < 160$ GeV	5.25
$107.5 < m_{\gamma\gamma} < 160$ GeV	5.18
$105 < m_{\gamma\gamma} < 160$ GeV	4.88 ± 1.03
$105 < m_{\gamma\gamma} < 157.5$ GeV	4.71
$105 < m_{\gamma\gamma} < 155$ GeV	4.50

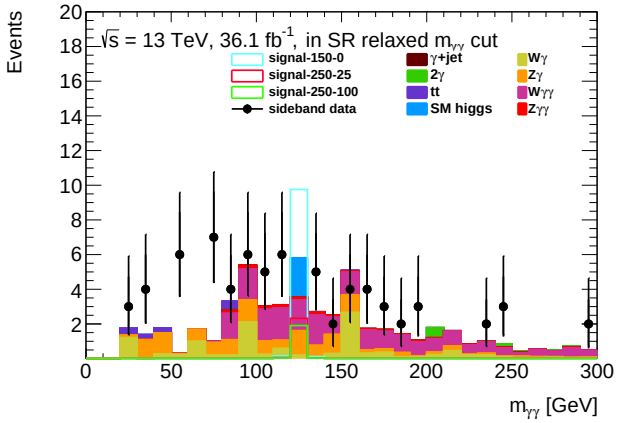

Figure6.3 $m_{\gamma\gamma}$ distributions in the inclusive SR with relaxed $m_{\gamma\gamma}$ requirement, which is [0, 300] GeV. Data (black points) are shown only for those distributed out of higgs window. Shown uncertainty is only statistical error on sideband data. Since $W\gamma\gamma$ sample is generating only $m_{\gamma\gamma} > 80$ GeV, there are deviation between data and MCs below 80 GeV region.

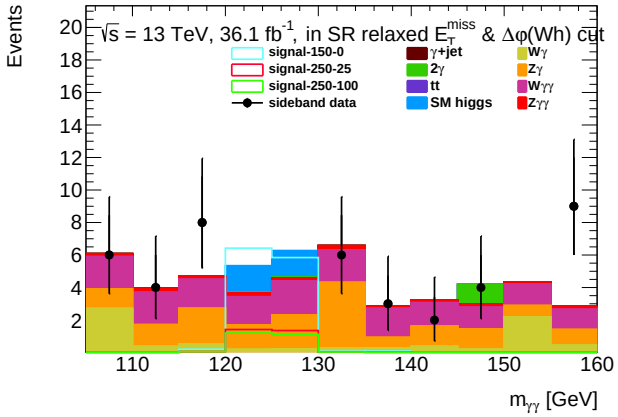

Figure6.4 $m_{\gamma\gamma}$ distributions in the inclusive SR with relaxed $E_{\mathrm{T}}^{\mathrm{miss}}$ and $\Delta\phi(\mathrm{W,h})$ requirements, which are 20 GeV and 0, respectively. Data (black points) are shown only for those distributed out of higgs window. Shown uncertainty is only statistical error on sideband data.

around the MC expectation, not only around the higgs window. The points around the higgs window accidentally have positive fluctuations, but the sizes of the fluctuations are reasonable to be statistical fluctuations.

One more study is performed by relaxing the selection. If the slopes are not due to statistical fluctuation, that shape is stable even with large statistics. In order to avoid effect to $m_{\gamma\gamma}$ shape, criteria on relatively non related discriminants, $E_{\mathrm{T}}^{\mathrm{miss}}$ and $\Delta\phi(\mathrm{W,h})$ are relaxed. For $E_{\mathrm{T}}^{\mathrm{miss}}$, threshold is relaxed from 40 GeV to 20 GeV. And $\Delta\phi(\mathrm{W,h})$ cut, which is $\Delta\phi(\mathrm{W,h}) > 2.25$, is removed. The result is shown in Figure 6.4 As expected, size of deviation from data to MCs becomes small. The data point of [130, 135] GeV is below the MC expectation.

Both of those study suggest that the mild slopes seen around the higgs window are due to statistical fluctuations.

[*2] It is seen that overall $m_{\gamma\gamma}$ distribution has mild slope. But it is confirmed that the assumption of slope dose not affect evaluation because of low statistic, as shown in the previous subsection.

6.2 Signal and Peaking Background

In contrast to the non-peaking backgrounds, it is difficult to separate the peaking backgrounds from the signal. All the kinematic variables introduced in the previous section are considered to efficiently separate them, but no variable could isolate only the peaking backgrounds with cut-base selection.

Even though isolating those two components are difficult, by dividing the signal region, an improvement of the significance was achieved using the "ratio" of yields between divided regions, as described in Chapter 7. For the evaluation of improvement, yield evaluations of signal and peaking backgrounds are important. In this section, the yields evaluated by MCs are explained.

6.2.1 Evaluated yields

Table 6.4 shows the yields expected by MCs. Those are evaluated with the final selections. Owing to the b-jet veto newly introduced in this analysis, $t\bar{t}h$ is suppressed to $\sim 10\%$.As shown in the table, the dominant source of the peaking background is the SM Wh.

Table6.4 Expected yields of the peaking backgrounds and the focus point signals for the subsets of the signal region.

Process	SRa	SRb	SRc	SRd
SM Wh	0.094 ± 0.014	1.504 ± 0.226	0.315 ± 0.047	1.818 ± 0.273
SM Zh	0.011 ± 0.002	0.067 ± 0.010	0.010 ± 0.002	0.077 ± 0.012
SM $t\bar{t}h$	0.033 ± 0.005	0.099 ± 0.015	0.014 ± 0.002	0.113 ± 0.017
ggh	< 0.001	< 0.001	< 0.001	< 0.001
VBFh	< 0.001	0.001 ± 0.001	< 0.001	0.001 ± 0.001
Total peaking background	0.138 ± 0.021	1.672 ± 0.251	0.338 ± 0.051	2.010 ± 0.302
$(m_{\tilde{\chi}_1^\pm, \tilde{\chi}_2^0}, m_{\tilde{\chi}_1^0}) = (150, 0)$	2.87	5.90	0.68	6.57
$(m_{\tilde{\chi}_1^\pm, \tilde{\chi}_2^0}, m_{\tilde{\chi}_1^0}) = (250, 25)$	1.36	0.86	0.04	0.90
$(m_{\tilde{\chi}_1^\pm, \tilde{\chi}_2^0}, m_{\tilde{\chi}_1^0}) = (250, 100)$	0.95	0.84	0.06	0.90

Chapter 7

Optimization of Signal regions

In this chapter, the defined signal region is further optimized. As an introduction, the idea of the optimization is described in Section 7.1. Some statistical definitions that are used for the optimization and the interpretation of the results are described in Section 7.2. The detail of the procedure of the optimization is described in Section 7.3, and the results of the optimization is described in Section 7.4.

7.1 Idea of optimization

As seen in Section 5.3, the signals and the backgrounds have different shapes in some kinematic variables, However, it is not possible to isolated only the signal using those variables. In other words, when the signal region is subdivided, both subsets have non negative yields of the signals and the backgrounds, such as shown in top of Figure 7.1. Since there are different shapes of some kinematic variables, the ratios of the yields between the two subsets subdivided by appropriate thresholds can be significantly different between the signal and the backgrounds. This information is useful to evaluate if there are any contributions of the signals in observed events; if there are only contributions of the backgrounds, the ratio between the two subsets must be close to the ratio of the backgrounds, such as shown in the bottom left of Figure 7.1. Otherwise, that could be due to the contributions of the signal, such as shown in the bottom right of Figure 7.1.

In order to evaluate the contributions of the signal, number of the observed events in both subdivided regions are fitted simultaneously by expected yields while fixing the ratio between the regions. It is called simultaneous fit. The merit of this procedure is that signal acceptance can be kept since the overall signal region is not changed.

The subdividing thresholds are defined by the optimization study described in this chapter. Since the purpose of this analysis is searching for un-discovered particles, the optimization has been performed by maximizing expected discovery significance defined in Section 7.2.3, by scanning the subdividing thresholds.

7.1.1 Distributions of discriminating variables

$E_{\mathrm{T}}^{\mathrm{miss}}$, $M_{\mathrm{T}}^{\mathrm{W}}$. $M_{\mathrm{T}}^{\mathrm{W}\gamma 1}$ and $M_{\mathrm{T}}^{\mathrm{W}\gamma 2}$ are considered as candidates of the subdividing variables in the optimization study. Figure 7.2 and Figure 7.3 show those distributions with the final selections.

7.2 Statistical definitions

Some statistical tools are used to search for the optimal subdivision and for the interpretation of the observed data in this analysis. In this section, the statistical tools used in this analysis are defined.

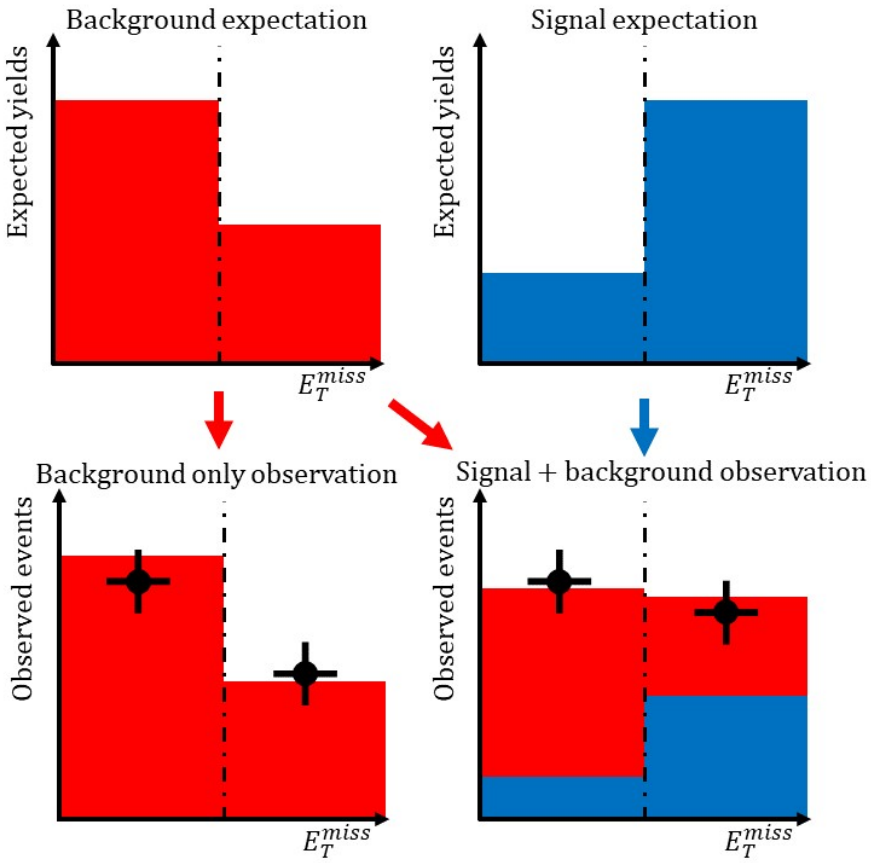

Figure7.1 Idea of optimization. As shown in the top two images, background is expected to have large contribution in low $E_{\mathrm{T}}^{\mathrm{miss}}$ region rather than high $E_{\mathrm{T}}^{\mathrm{miss}}$ region, in contrast to signal which has large contribution in high $E_{\mathrm{T}}^{\mathrm{miss}}$ region rather than low $E_{\mathrm{T}}^{\mathrm{miss}}$ region. In case that observed data includes only background, the ratio between the two regions is close to the expected ratio of background yields, as shown in the left bottom image. If there are contribution of signal in observed data, the ratio is different from the expected ratio of background yields, as shown in the right bottom image.

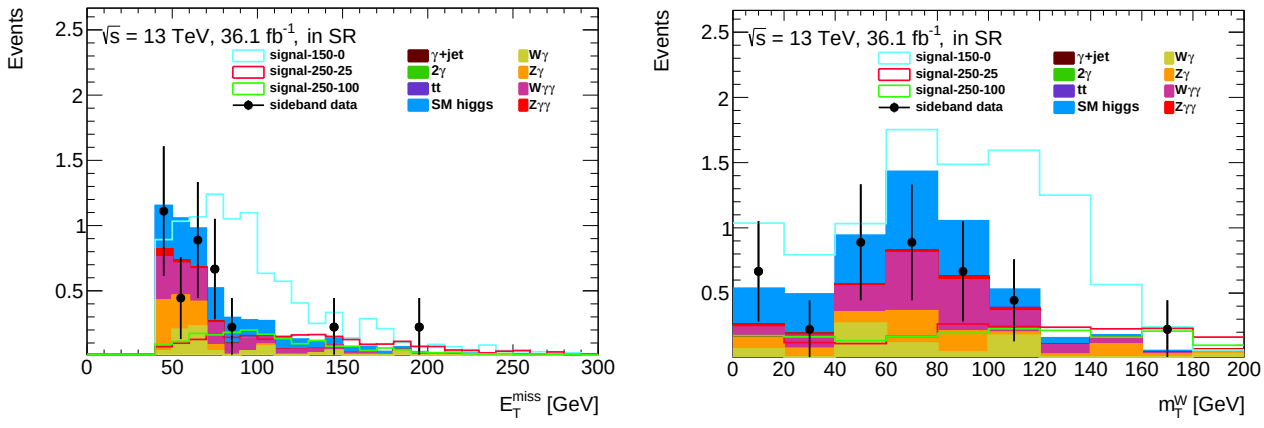

Figure7.2 Missing transverse energy (left) and $M_{\mathrm{T}}^{\mathrm{W}}$ (right) distributions in the signal region. Contributions of non-peaking backgrounds are scaled by 10/55, which is the ratio of $m_{\gamma\gamma}$ width between the higgs window and the sideband window. Data (black points) are shown for only for those distributed out of higgs window, and are scaled by 10/45. Shown uncertainty is only statistical error on sideband data.

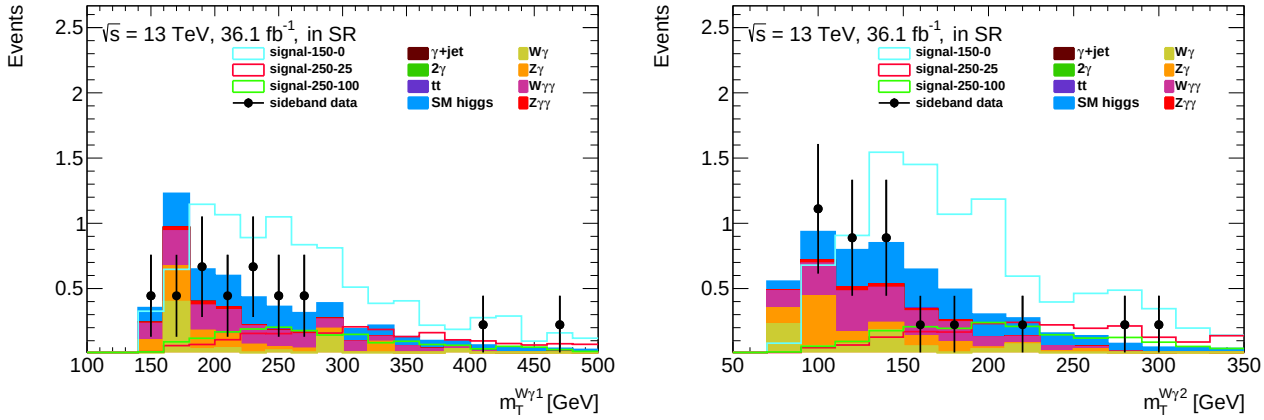

Figure7.3 $M_{\mathrm{T}}^{\mathrm{W}\gamma 1}$ (left) and $M_{\mathrm{T}}^{\mathrm{W}\gamma 2}$ (right) distributions in the signal region. Contributions of non-peaking backgrounds are scaled by 10/55, which is the ratio of $m_{\gamma\gamma}$ width between the higgs window and the sideband window. Data (black points) are shown for only for those distributed out of higgs window, and are scaled by 10/45. Shown uncertainty is only statistical error on sideband data.

7.2.1 Likelihood

In this analysis, binned likelihood ($\mathcal{L}$) is used. As described above chapters, the yields of non-peaking backgrounds (b_i), peaking backgrounds (h_i), and signals (s_i) are evaluated in each subset of the signal regions. Using those yields and their relative uncertainties which are $\sigma_{b,i}$, σ_h and σ_s respectively, $\mathcal{L}$ is defined as

$$\mathcal{L} = \exp(-\frac{{\theta_s}^2}{2}) \exp(-\frac{{\theta_h}^2}{2}) \Pi_i \frac{e^{-\lambda_i} {\lambda_i}^{N_i}}{N_i!} \exp(-\frac{{\theta_{b,i}}^2}{2}), \tag{7.1}$$

where $\lambda_i = \mu(1+\theta_s\sigma_s)s_i + (1+\theta_h\sigma_h)h_i + (1+\theta_{b,i}\sigma_{b,i})b_i)$. Here i shows a subset of the signal region. Therefore, it runs from "a" to "d". θ_s, θ_h and $\theta_{b,i}$ are nuisance parameters associated with the uncertainties of the signal, the peaking and the non-peaking backgrounds. μ is the signal strength. N_i is the observed number of events in each subset of the signal region. This likelihood is defined by the product of a Poisson function and constraint terms for the nuisance parameters. The Poisson function part provides high values when the total yields (λ_i) is close to the observed number of the events. The constraint terms are to limit fitted yields within size of the uncertainties.

As described in Chapter 8, dominant source of uncertainty is the statistical uncertainty for non-peaking backgrounds. On the other hand, σ_h and σ_s are mainly from systematical uncertainty on MC. Therefore, individual nuisance parameter is defined for each subset of the signal region for the non-peaking backgrounds. For the signal and the peaking backgrounds, one nuisance parameter is shared among all subsets of the signal region.

In the optimization study, $\sigma_h = 13.8\%$ and $\sigma_s = 15\%$ are used as tentative values. Those values are evaluated by rough estimation described in Section 8.2 and 8.3. The effect of the fluctuation of those uncertainties are discussed in Section 7.4.1, and the precise evaluation of them are discussed in Chapter 8. For $\sigma_{b,i}$, the uncertainties shown in Table 6.1 are used, which is evaluated in Section 8.1.

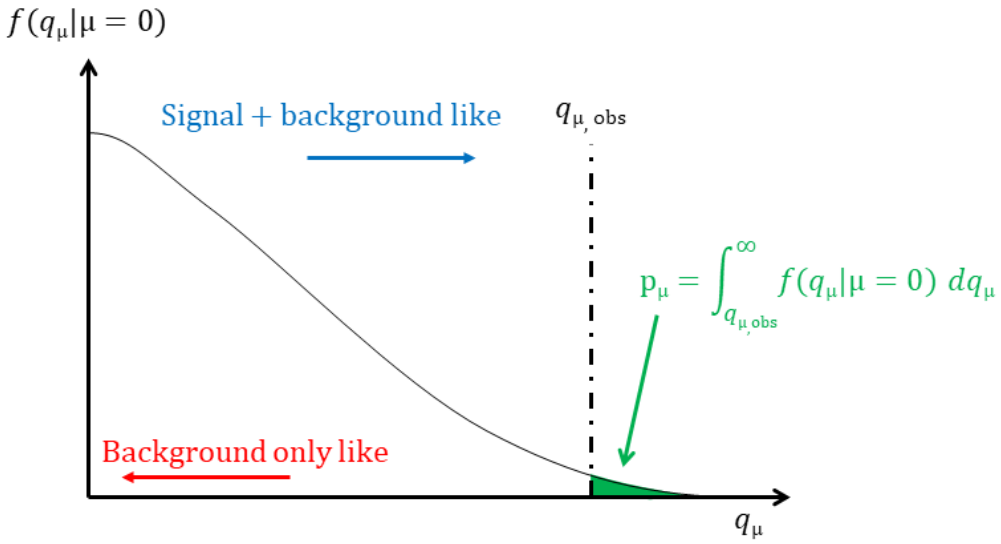

Figure7.4 Image of q_μ distribution and definition of p_μ. This image is case of the assumption of $\mu = 0$. With this assumption, backgrounds only like events show small q_μ, and signal + background like events show large q_μ. p_μ is defined as probability to observe q_μ larger than $q_{\mu,\mathrm{obs}}$. as shown as a green area.

7.2.2 Test statistic

In order to do statistical hypothesis tests, the test statistic is also defined with given signal strength μ as

$$q_\mu = \begin{cases} -2\ln \frac{\mathcal{L}(\mu,\hat{\hat{\theta}})}{\mathcal{L}(0,\hat{\theta}(0))} & (\hat{\mu} < 0), \\ -2\ln \frac{\mathcal{L}(\mu,\hat{\hat{\theta}})}{\mathcal{L}(\hat{\mu},\hat{\theta}(\mu))} & (\hat{\mu} \geq 0), \end{cases} \tag{7.2}$$

This is based on the likelihood ratio $\frac{\mathcal{L}(\mu,\hat{\hat{\theta}})}{\mathcal{L}(\hat{\mu},\hat{\theta}(\mu))}$, where $\hat{\hat{\theta}}$ is the nuisance parameters maximizing $\mathcal{L}$ with given μ. $\hat{\mu}$ and $\hat{\theta}$ are the combination of the signal strength the nuisance parameters maximizing $\mathcal{L}$. Since negative signal strength is not considered in this analysis, when $\hat{\mu}$ is negative, $\hat{\mu}$ is fixed to zero and $\hat{\theta}$ is re-evaluated with that setup.

When given μ describes well the observed events, the likelihood ratio is close to 1, and q_μ is close to 0. Large q_μ means inconsistency between given μ and the observed events. In order to evaluate the inconsistency, the p-value is defined as

$$p_\mu = \int_{q_{\mu,\mathrm{obs}}}^{\infty} f(q_\mu|\mu) dq_\mu \tag{7.3}$$

where $f(q_\mu|\mu)$ is the probability density function of q_μ under the assumption that given μ describes the physics. q_{obs} is calculated q_μ with the observed numbers of the events. Image of $f(q_\mu|\mu)$ and q_μ are drawn in Figure 7.4. The meaning of the p-value is the possibility that q_μ greater than q_{obs} is observed when given μ is correct.

In most of the cases in this analysis, $f(q_\mu|\mu)$ function is evaluated by using toy samples as following. First, background only model or background plus new physics model are assumed. Next, many toy sample in each signal region subset are generated, assuming that their probability density functions are Poisson functions which give the expected yields as their averages. Then, q_μ is evaluated with each generated toy sample, and the normalized distribution of evaluated q_μ is used as $f(q_\mu|\mu)$.

Since the evaluation with toy samples takes long time, the optimization has been performed with the asymptotic method described as following. The asymptotic method is under the assumption of the Wald appropriation [62]. With this assumption, $f(q_\mu|\mu)$ is given as

$$f(q_\mu|\mu) = \frac{1}{\sqrt{2\pi}} \frac{1}{\sqrt{q_\mu}} e^{-q_\mu/2}. \tag{7.4}$$

This method is useful to evaluate p-value in short time, but it is known that there is inconsistency between evaluated p-value with this method and the toy method, especially when the yields of signals and backgrounds are small. As shown in the previous chapter, the yields are expected to be small. Therefore, the asymptotic method is used only at the optimization study, and toy method is used for the other studies.

The evaluated p-value p_μ is interpreted as a significance (Z_μ) with following function:

$$Z_\mu = \Phi^{-1}(1 - p_\mu), \tag{7.5}$$

where Φ^{-1} is the inverted function of the standard Gaussian. In the ATLAS experiment, typically 5σ (p-value $= 2.87 \times 10^{-7}$) is required for the discovery of new physics, and 3σ (p-value $= 1.35 \times 10^{-3}$) is required for the evidence of new physics. For the discussion of the exclusion, when (1− p-value) is larger than the confidence level, the assumed model is excluded. Typically, 5% p-value (95% confidence level) is used as the threshold.

7.2.3 Significance for discovery

When observed number of events is greater than the yields expected by the SM, it could be due to the contribution of new physics. In that case, the significance for discovery is calculated as following. When such events are observed, q_μ is calculated under the assumption of $\mu = 0$. Evaluated significance from p_0 is called the discovery significance. It shows the probability that the inconsistency between the expectation and the data is larger than the experimentally observed case, under the assumption that there are no new physics.

In order to evaluate the significance with blinded information, the most probable significance for discovery is evaluated as expected discovery significance. For the evaluation, instead of q_{obs}, the most probable $q_{\rm exp}$ is used, which is the mean of the probability density function of q_μ under the assumption of $\mu = 1$ with the focus point signal models ($f(q_\mu|\mu = 1)$). Therefore, the evaluated p_0 shows the expected p_0 value when the assumed model is completely correct.

In the optimization, the expected p_0 values are used as the figure of merit. If expected p_0 is large, it means that no statistical differences from the SM expectation can be seen even if the assumed new physics exists. Therefore, this value can be used to estimate the range in the parameter space where the signal event can be discovered if it exists.

7.2.4 Significance for exclusion

When observed number of events is close to the yields expected by the SM, the results can be interpreted as the exclusion of some of the physics models which expect large signal yields. For this type of discussion, p_μ is calculated as a function of μ. Evaluated significance from p_μ is called the exclusion significance. If p_μ evaluated with $\mu = 1$ is smaller than (1− confidence level), assumed model is excluded by "confidence level".

The upper limit of the signal strength μ is also evaluated from p_μ. Typically, larger μ leads to smaller p_μ. μ which provides q_μ equal to (1− confidence level) is the upper limit of the signal strength. The product of the upper limit on the signal strength and the expected yields of signal is considered as the upper limit on the expected yields of the signal. By dividing the upper limit on the expected yields of signal by collected luminosity, the upper limit on the signal cross section can be evaluated.

In order to evaluate expected significance with blinded information for the exclusion, $q_{\rm exp}$ is evaluated from the mean of the probability density function of q_μ under the assumption of $\mu = 0$ ($f(q_\mu|\mu = 0)$). Therefore, the evaluated p_μ under this assumption shows expected p_μ value when there are no new physics.

7.2.5 Model independent significance

Significance evaluation under assumptions about the signal can be biased. To avoid such bias, model independent significance is evaluated. At this evaluation, since the expected signal yields (s_i) cannot be assumed, overall signal yields (S) is used instead of $s_i\mu$ Since the ratio of the signal yields between different signal regions cannot be assumed, this type of significance is evaluated in individual signal region.

For the interpretation of the results to the discovery significance, this model independent significance is used. By using model independent significance for exclusion, upper limits on the yield and the cross section of new physics can be evaluated without assuming any specific physics models.

7.3 Procedure of optimization

As described in Section 7.1, the optimization has been performed by maximizing the expected discovery significance. The procedure is described below.

First, discriminating variables for the subdivision are defined. In this study, one or two variables are used. For each chosen combination of the variables, the thresholds dividing signal region are scanned and expected discovery significance is evaluated with three focus points. Scan range and step are summarized in Table 7.1. Then, the thresholds achieving highest significances are chosen as the best thresholds for the scanned discriminating variables.

For the decision of the best thresholds, root mean square of the two high-mass signals is considered. This is because the low-mass signal has been excluded by the 8 TeV analysis, and owing to its large signal yield high enough significance is expected even without the optimization. The expected significance for the low-mass signal is only used for the verification of the high expected significance after the optimization.

This study has been performed with the early selections.

7.4 Optimization results

Table 7.2 shows the achieved significances and the best thresholds with one discriminating variable. Table 7.3 shows those with two discriminating variables. In order to see the improvement, original expected significances without subdividing signal region are shown in the top row of the tables, and the improvement ratios against the originals are shown in the Gain column. Those results are obtained with the early selections.

As shown in the tables, the optimization with two discriminating variables can achieve higher significances than the optimization with one discriminating variable. From Table 7.3, it is found that the subdivisions using ($M_{\rm T}^{{\rm W}\gamma 2}$,$M_{\rm T}^{\rm W}$) and using ($M_{\rm T}^{\rm W}$,$E_{\rm T}^{\rm miss}$) achieved similarly highest significances.

Table7.1 Optimization range and step

Discriminating variables	Ranges [GeV]	Steps [GeV]
$E_{\rm T}^{\rm miss}$	[40, 110]	10
$M_{\rm T}^{\rm W}$	[0, 160]	10
$M_{\rm T}^{{\rm W}\gamma 1}$	[150, 300]	10
$M_{\rm T}^{{\rm W}\gamma 2}$	[80, 150]	10

Since the achieved results with the two high-mass signals are similar, expected discovery significances with all the signal samples are evaluated with those two subdivisions to conclude which combination is the best. The results are shown in Figure 7.5 and 7.6. In those figures, expected significances for some of the higher mass signals cannot be evaluated since the evaluated p-value is too high. Although those two results are similar, ($M_{\mathrm{T}}^{\mathrm{W}\gamma 2}$,$M_{\mathrm{T}}^{\mathrm{W}}$) combination is chosen since it achieved slightly better significances than ($M_{\mathrm{T}}^{\mathrm{W}}$,$E_{\mathrm{T}}^{\mathrm{miss}}$). The region above the thresholds is called SRa, and the complement region is called SRd.

Figure 7.7 and Figure 7.8 show the ($M_{\mathrm{T}}^{\mathrm{W}\gamma 2}$, $M_{\mathrm{T}}^{\mathrm{W}}$) distributions of the peaking backgrounds and the three focus points, which defined in Section 5.3.1.

As shown in Figure 7.7, the peaking backgrounds are mainly distributed $M_{\mathrm{T}}^{\mathrm{W}} \sim 80$ GeV and low $M_{\mathrm{T}}^{\mathrm{W}\gamma 2}$ region, as expected from the main source of the peaking backgrounds which is the SM Wh. Since the SM Wh has only neutrino as a source of $E_{\mathrm{T}}^{\mathrm{miss}}$, the W object is expected to be reconstructed from a neutrino and a lepton only, without contributions of LSPs. Thus, $M_{\mathrm{T}}^{\mathrm{W}}$ is expected to be around the W mass (80 GeV). Due to the lack of the contributions of LSPs, $E_{\mathrm{T}}^{\mathrm{miss}}$ can be relatively lower than $E_{\mathrm{T}}^{\mathrm{miss}}$ of the signal events. This leads to relatively low $M_{\mathrm{T}}^{\mathrm{W}\gamma 2}$ value.

From the tendency described above, further subdivision is suggested. The idea is isolating the peaking backgrounds by subdividing SRd into SRc (the peaking backgrounds is mainly distributed) and SRb (the complement to SRc in the SRd). The definitions of the subsets are summarized in Table 5.2 and Figure 5.10. The expected significances are evaluated with the combination of SRa and SRb and SRc, and the combination of SRa and SRc also. Those results are shown in Figure 7.9 and 7.10. Comparing those results with Figure 7.6, obviously the original combination of SRa and SRd shows the best results. Therefore, the combination of SRa and SRd is chosen as the signal region subsets.

Table7.2 Best thresholds and achieved significances with one discriminating variable

Discriminating variables	Thresholds (GeV)	$(m_{\tilde{\chi}_1^\pm,\tilde{\chi}_2^0}, m_{\tilde{\chi}_1^0})$(GeV) = (150, 0)	Gain	(250, 25)	Gain	(250, 100)	Gain
Original	—	2.92	—	0.47	—	0.21	—
$E_{\mathrm{T}}^{\mathrm{miss}}$	90	2.87	0.98	0.64	1.37	0.34	1.59
$M_{\mathrm{T}}^{\mathrm{W}}$	120	3.05	1.04	0.88	1.88	0.59	2.77
$M_{\mathrm{T}}^{\mathrm{W}\gamma 1}$	270	2.75	0.94	0.72	1.55	0.33	1.54
$M_{\mathrm{T}}^{\mathrm{W}\gamma 2}$	40	3.22	1.10	0.65	1.40	0.37	1.74

Table7.3 Best thresholds and achieved significances with two discriminating variables

Discriminating variables	Thresholds (GeV)	$(m_{\tilde{\chi}_1^\pm,\tilde{\chi}_2^0}, m_{\tilde{\chi}_1^0})$(GeV) = (150, 0)	Gain	(250, 25)	Gain	(250, 100)	Gain
Original	—	2.92	—	0.47	—	0.21	—
$M_{\mathrm{T}}^{\mathrm{W}\gamma 1}$,$M_{\mathrm{T}}^{\mathrm{W}\gamma 2}$	(240,140)	2.93	1.00	0.74	1.57	0.41	1.95
$M_{\mathrm{T}}^{\mathrm{W}\gamma 1}$,$M_{\mathrm{T}}^{\mathrm{W}}$	(190,120)	3.07	1.05	0.87	1.87	0.59	2.78
$M_{\mathrm{T}}^{\mathrm{W}\gamma 1}$,$E_{\mathrm{T}}^{\mathrm{miss}}$	(220,90)	2.96	1.01	0.73	1.56	0.37	1.74
$M_{\mathrm{T}}^{\mathrm{W}\gamma 2}$,$M_{\mathrm{T}}^{\mathrm{W}}$	(140,110)	3.01	1.03	0.90	1.92	0.64	3.03
$M_{\mathrm{T}}^{\mathrm{W}\gamma 2}$,$E_{\mathrm{T}}^{\mathrm{miss}}$	(140,70)	2.97	1.01	0.73	1.56	0.41	1.93
$M_{\mathrm{T}}^{\mathrm{W}}$,$E_{\mathrm{T}}^{\mathrm{miss}}$	(100,70)	2.94	1.01	0.93	1.98	0.62	2.92

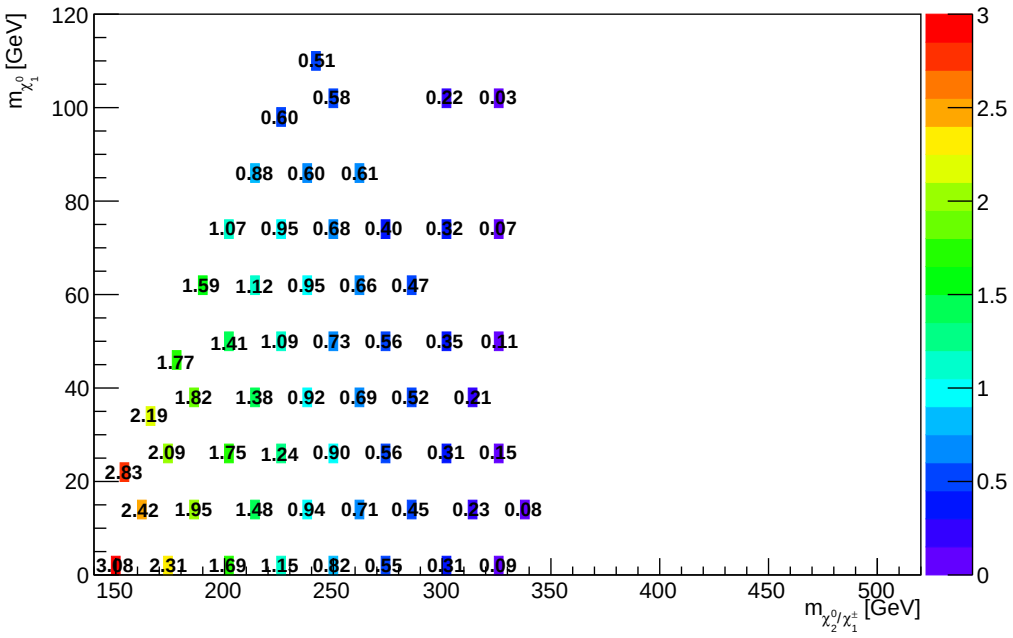

Figure7.5 Significances in ($m_{\tilde{\chi}_1^\pm,\tilde{\chi}_2^0}$,$m_{\tilde{\chi}_1^0}$) parameter space for the subdivision based on the values $M_{\mathrm{T}}^{\mathrm{W}} = 70$ GeV and $E_{\mathrm{T}}^{\mathrm{miss}} = 100$ GeV.

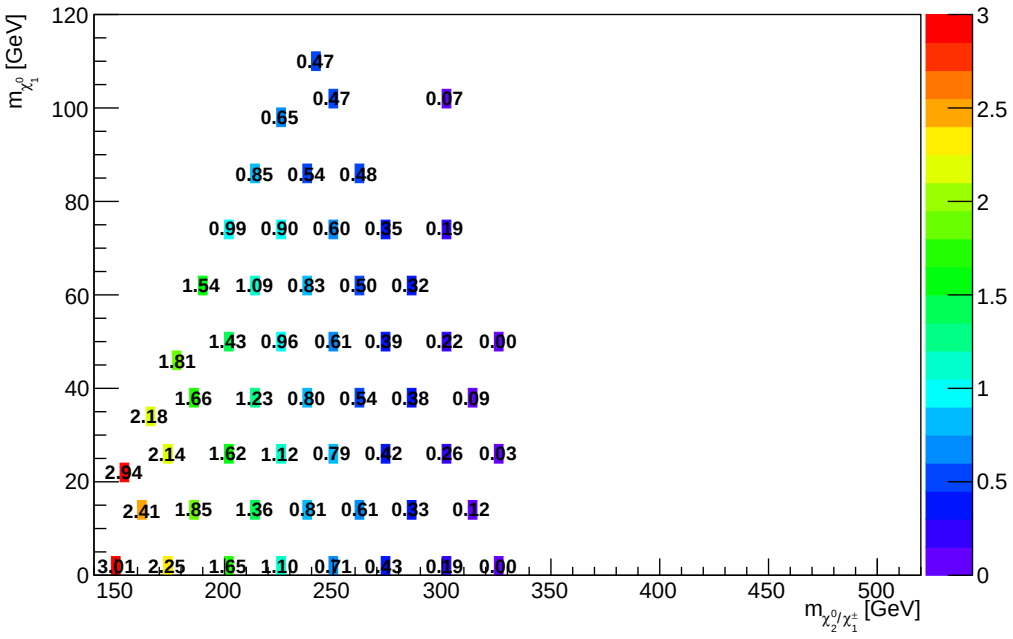

Figure7.6 Significances in ($m_{\tilde{\chi}_1^\pm,\tilde{\chi}_2^0}$,$m_{\tilde{\chi}_1^0}$) parameter space for the subdivision based on the values $M_{\mathrm{T}}^{\mathrm{W}\gamma 2} = 140$ GeV and $M_{\mathrm{T}}^{\mathrm{W}} = 110$ GeV.

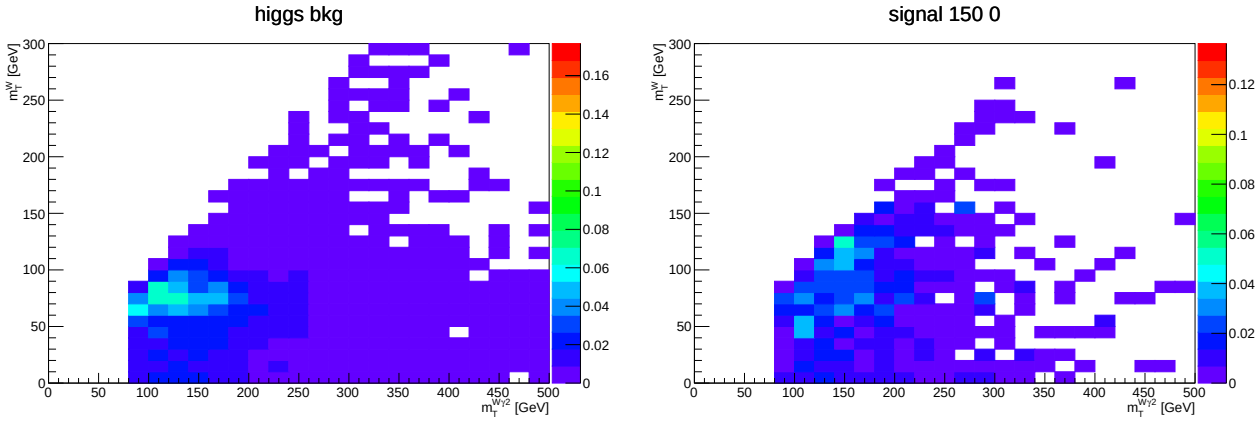

Figure7.7 $(M_{\mathrm{T}}^{\mathrm{W}\gamma 2}, M_{\mathrm{T}}^{\mathrm{W}})$ distribution of peaking background (left) and the $(m_{\tilde{\chi}_1^\pm,\tilde{\chi}_2^0}, m_{\tilde{\chi}_1^0}) = (150, 0)$ GeV (right) in the signal region.

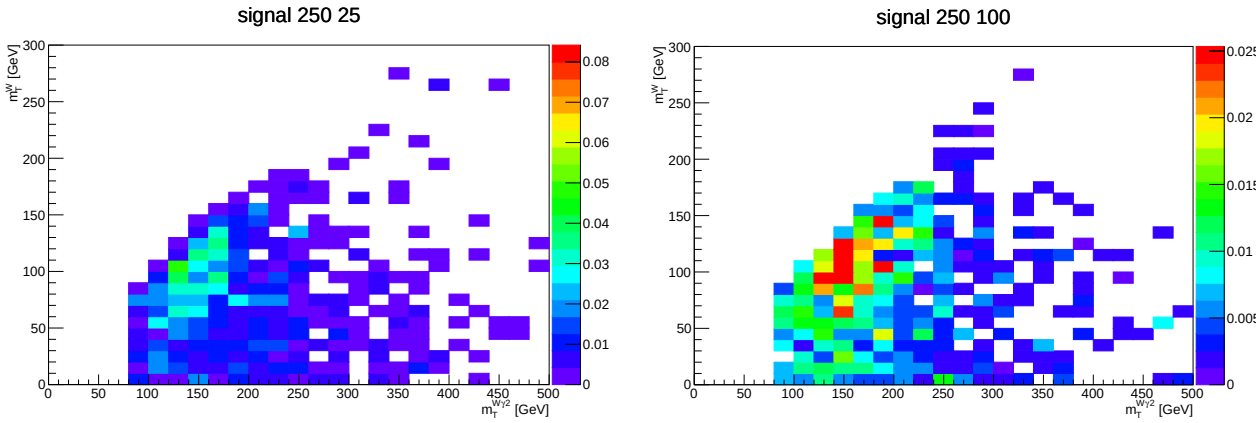

Figure7.8 $(M_{\mathrm{T}}^{\mathrm{W}\gamma 2}, M_{\mathrm{T}}^{\mathrm{W}})$ distribution of the $(m_{\tilde{\chi}_1^\pm,\tilde{\chi}_2^0}, m_{\tilde{\chi}_1^0}) = (250, 25)$ GeV signal point (left) and the $(m_{\tilde{\chi}_1^\pm,\tilde{\chi}_2^0}, m_{\tilde{\chi}_1^0}) = (250, 100)$ GeV signal point (right) in the signal region.

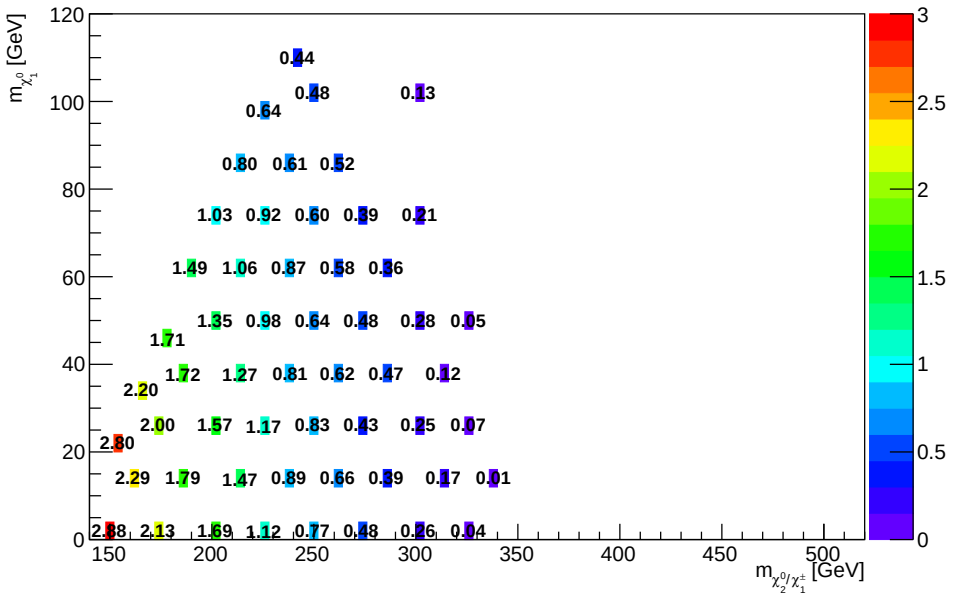

Figure7.9 Signal significance across the $(m_{\tilde{\chi}_1^\pm,\tilde{\chi}_2^0}, m_{\tilde{\chi}_1^0})$ grid with SRa, SRb and SRc.

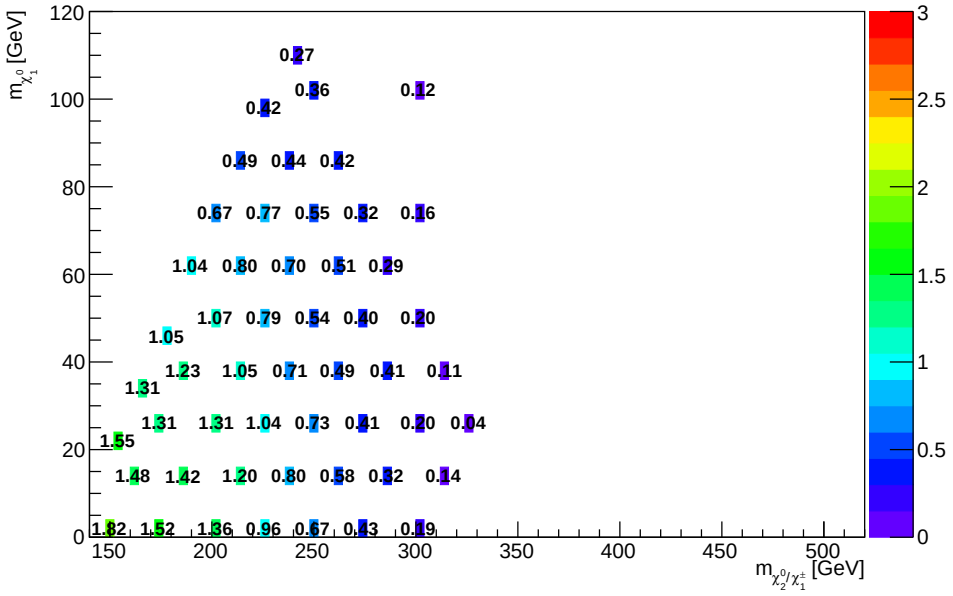

Figure7.10 Signal significance across the ($m_{\tilde{\chi}_1^\pm,\tilde{\chi}_2^0}$,$m_{\tilde{\chi}_1^0}$) grid with SRa and SRc.

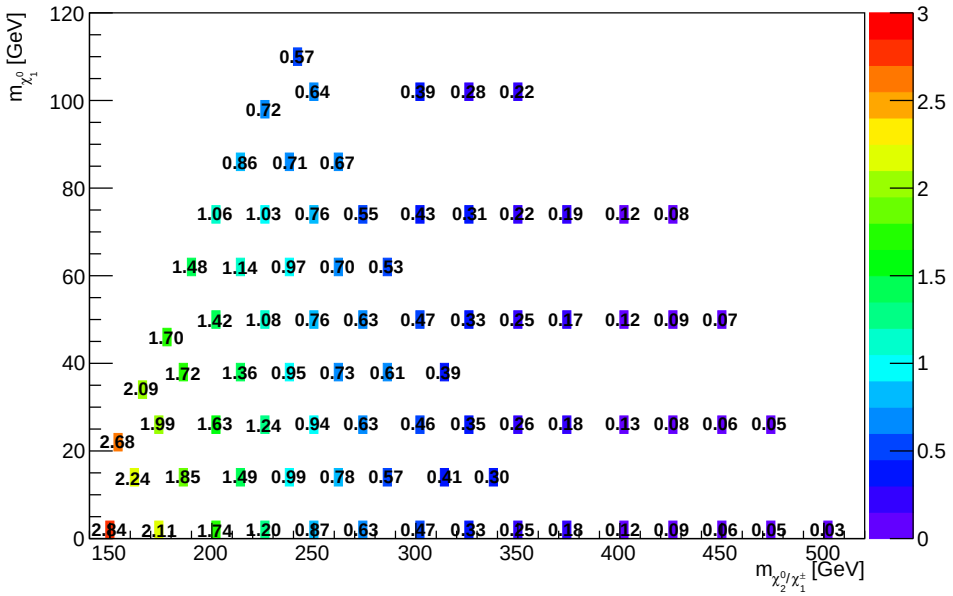

Figure7.11 Expected exclusion significances with $\sigma_h = 13.8\%$ and $\sigma_s = 8\%$.

7.4.1 Effect of uncertainties

The optimization study described above has been done with tentative values. In order to evaluate effect from fluctuation of the uncertainties, exclusion significances were evaluated with uncertainty on the peaking backgrounds σ_h from 8% to 20%. The results are shown in Figure 7.11 to 7.13. From those figures, there are no visible effect due to the fluctuation of σ_h. It is expected that this is due to large uncertainties on non-peaking backgrounds. This study suggests that significance cannot be improved even if uncertainties on peaking backgrounds or signals can be reduced from the precise evaluations. Therefore, the conservative evaluations have been done in Chapter 8.

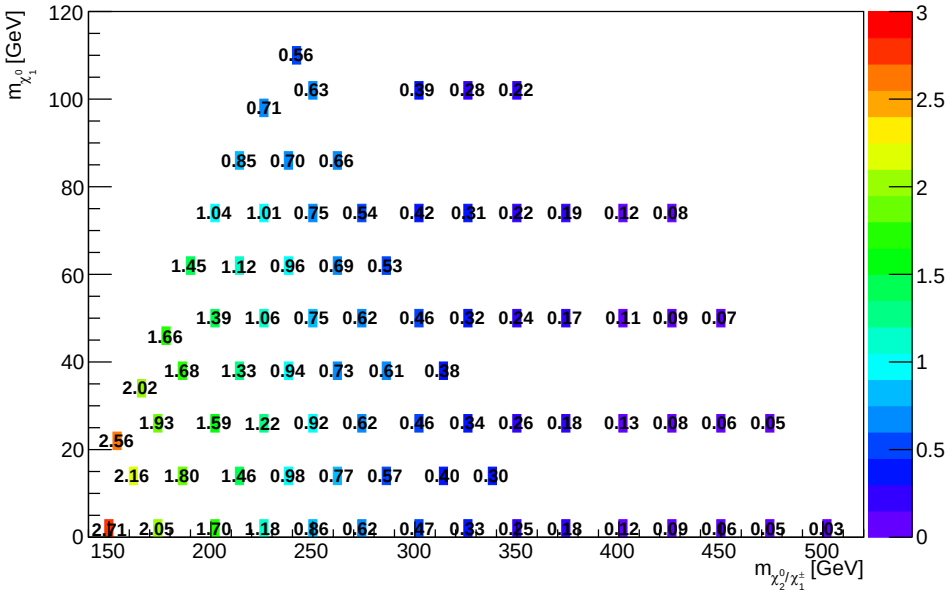

Figure7.12 Expected exclusion significances with $\sigma_h = 13.8\%$ and $\sigma_s = 15\%$.

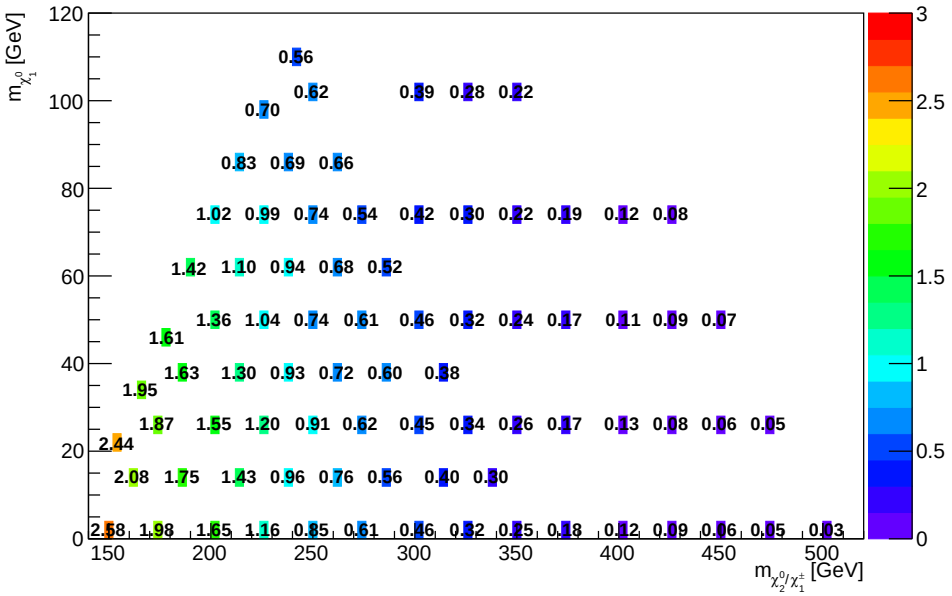

Figure7.13 Expected exclusion significances with $\sigma_h = 13.8\%$ and $\sigma_s = 20\%$.

7.4.2 Effect of updates of setup

The optimization studies described above have been performed with 27 GeV threshold on $p_{\mathrm{T}}^{\gamma 2}$. After those studies, the threshold is increased to 31 GeV. At the same period, a few more updates have been done as following:

- σ_h is updated from 13.8% to 15% according to the study described in Section 8.2
- σ_s is updated from 15% to 8% according to the study described in Section 8.3
- SM Wh and SM Zh samples are updated from LO samples to NNLO samples

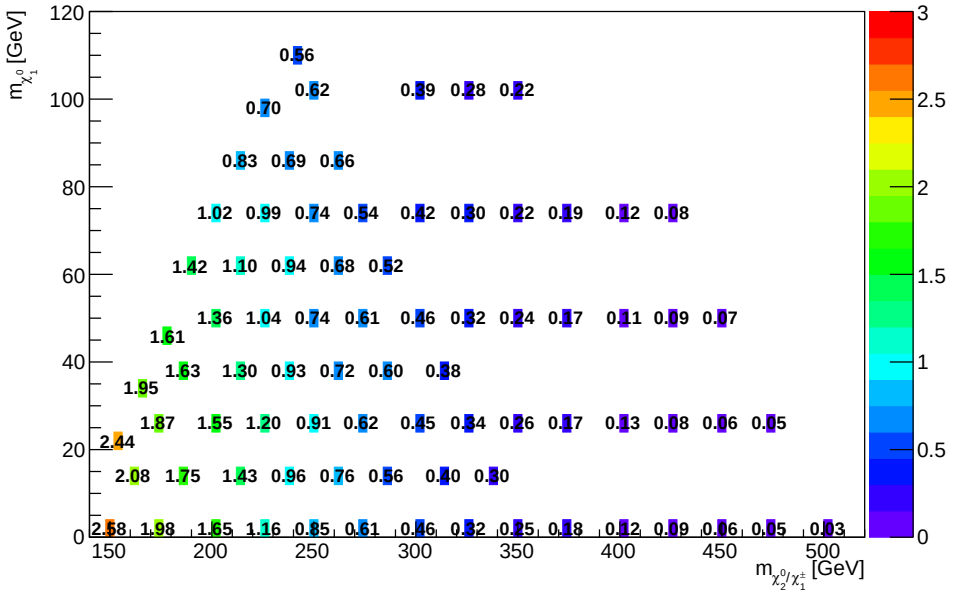

Figure7.14 Expected exclusion significances with $\sigma_h = 13.8\%$ and $\sigma_s = 20\%$ with the updated setup.

As described in Section 5.3.2, the requirements before this change are early selections, and those after the change are noted as final selections.

Since the optimization has been performed with the early selections, in order to evaluate the effect of those changes, expected exclusion significances is re-evaluated with final selections, as shown in Figure 7.14. From the comparison between Figure 7.12 and 7.14, it is concluded that there are no significant effects due to this update. Therefore, the same optimized results are used with the final selections.

Chapter 8

Systematic and statistical uncertainty

In this chapter, the uncertainties on the three types of the events, namely the non-peaking backgrounds, the peaking backgrounds, and the signals, are described.

The yields of the non-peaking backgrounds are evaluated from the sideband data. Therefore, it is affected by statistical fluctuation of the sideband data. This is discussed in Section 8.1.

In contrast, the peaking backgrounds and the signals are evaluated from the MCs. Therefore, it is affected by uncertainty on the MCs. This is discussed in Section 8.2 and 8.3.

The evaluation has been performed for SRa to SRd in this chapter. The uncertainties used in the optimization study has been evaluated in the same manner.

8.1 Non-peaking Background

As described in Section 6.1.1, the non-peaking backgrounds are evaluated by the sideband fit. Due to the low statistics of the data in the sideband region, large statistical fluctuation is expected. It is evaluated by using the toy sample.

The evaluation procedure is shown in Figure 8.1 It has been performed as following. At first, sideband data is fitted with a constant function. Then, toy samples are generated using Poisson function which has the fitted result as its mean. Next, each generated sample is fitted by a constant function and yield is re-evaluated. Finally, the statistical uncertainties are evaluated from those distributions.

The distributions of re-evaluated yields for the overall toy samples are shown in Figure 8.2 and Figure 8.3. The uncertainty is defined as 1σ equivalent width of the distribution. However, as shown in the distributions, re-evaluated yields are discretely distributed. This is because generated toy samples have discrete number of events for each bin. Due to their discreteness, the width exactly equivalent to 1σ cannot be defined. Therefore, in this analysis, the wider side of the width closest to 1σ equivalent width is chosen as shown in the figures.

In the case that the evaluated uncertainties for upper side and lower side are different, conservative side, i.e. with larger one, is chosen as an uncertainty. The evaluated uncertainties are summarized in Table 6.1. Due to low statistics in the sideband region, the evaluated uncertainties are large as expected.

8.2 Peaking Background

As described in Section 7.4.1, the results are not affected by the uncertainties on peaking backgrounds and the signals due to the large uncertainties on the non-peaking backgrounds. Therefore, in this analysis, conservative uncertainties are evaluated and used.

At first, the experimental uncertainties are evaluated. Since the yields are evaluated by the MCs, the evaluation of the uncertainties also relies on the MCs. The uncertainties include errors on event generator and detector performance.

In the ATLAS experiment there are many sources of the experimental uncertainties. They are

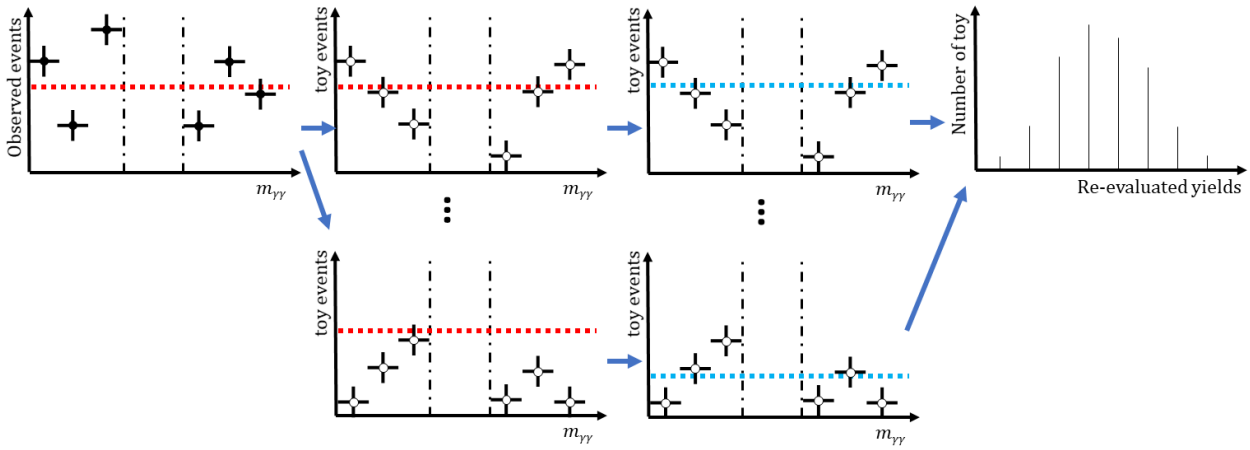

Figure8.1 Conceptual drawing of uncertainty evaluation procedure for non-peaking backgrounds. From left side, sideband data fit, toy sample generation, re-evaluation of yields of toy samples, and distribution of re-evaluated yields is shown. From the width of the distribution, uncertainty is evaluated.

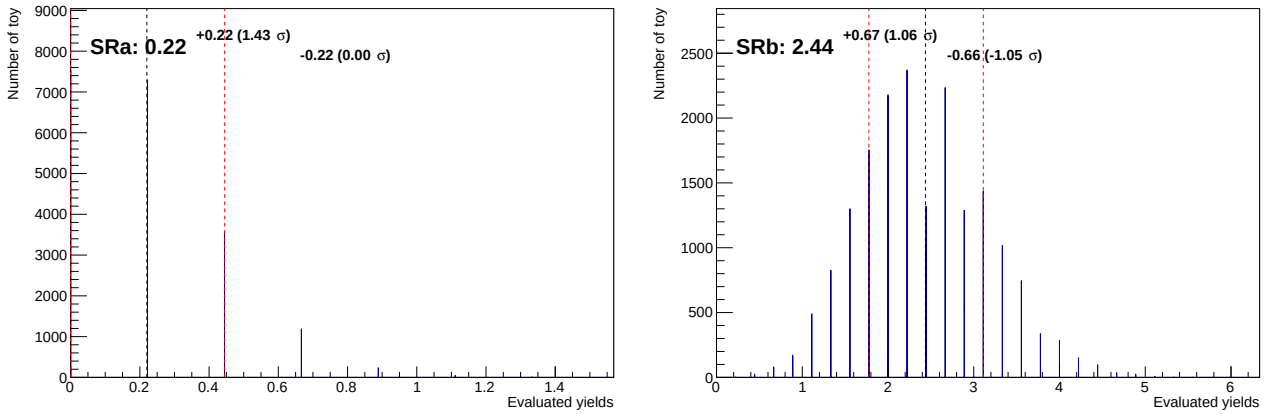

Figure8.2 Distributions of re-evaluated yields in SRa (left) and in SRb (right).

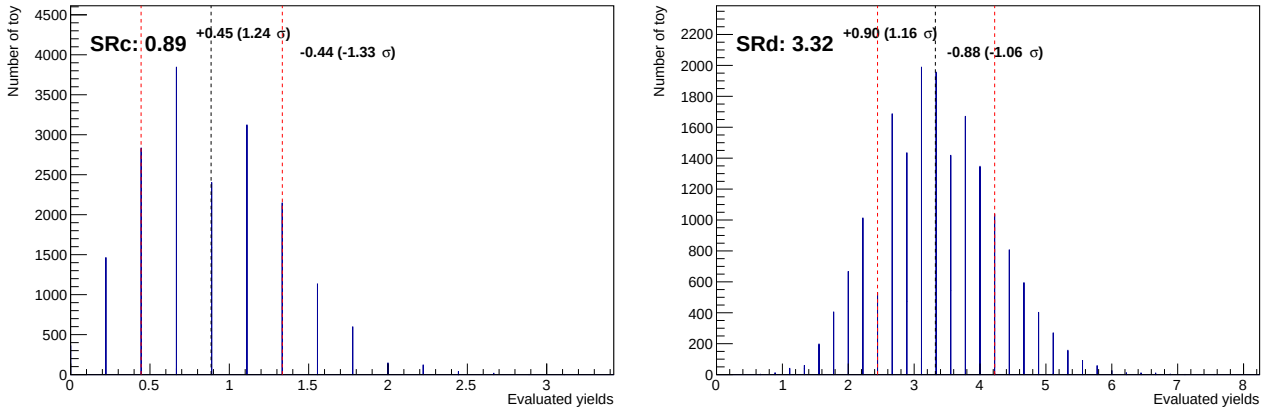

Figure8.3 Distributions of re-evaluated yields in SRc (left) and in SRd (right).

classified into the groups which are not correlated to each other. In this analysis, following groups are taken into account.

- photon ID efficiency
- b-tag scale factor
- photon energy resolution
- photon energy scale factor
- 3 groups of jet energy scale factors[*1]
- jet energy resolution
- $E_{\mathrm{T}}^{\mathrm{miss}}$ resolution
- $E_{\mathrm{T}}^{\mathrm{miss}}$ scale factor
- photon isolation efficiency

All of systematics have both positive and negative variations on the sources except for the photon isolation efficiency[*2].

For the evaluation of effects from those uncertainties to the evaluated yields, specific MC sample is developed for each group in the ATLAS experiment. Those samples are generated with a performance parameter shifted for 1σ. Taking differences between nominal sample and those systematical samples, systematical uncertainties on the yields can be evaluated. In table 8.1, the evaluated yields and systematics with the various specific samples are summarized. In order to evaluate total experimental uncertainties, quadratic sum of the those uncorrelated systematics are calculated in SRa and SRd.

Table8.1 Yields and systematics of the peaking backgrounds evaluated by systematic MCs. In the case that the absolute value of evaluated systematic is smaller than 0.001, it is shown as 0.

Sources	SRa Yield	SRa systematics	SRd Yield	SRd systematics
Nominal	0.111		2.09	
ph-totSF-eff-id-up	0.113	0.002	2.12	0.03
ph-totSF-eff-id-down	0.109	-0.002	2.05	-0.04
jet-totBtagSF-up	0.111	0	2.09	0
jet-totBtagSF-down	0.111	0	2.09	0
SYST-EG-RESOLUTION-ALL-1down	0.108	-0.003	2.08	-0.01
SYST-EG-RESOLUTION-ALL-1up	0.107	-0.004	2.06	-0.03
SYST-EG-SCALE-ALL-1down	0.106	-0.005	2.05	-0.04
SYST-EG-SCALE-ALL-1up	0.108	-0.003	2.07	-0.02
SYST-JET-GroupedNP-1-1down	0.102	-0.009	2.11	0.02
SYST-JET-GroupedNP-1-1up	0.122	0.011	2.05	-0.04
SYST-JET-GroupedNP-2-1down	0.107	-0.004	2.08	-0.01
SYST-JET-GroupedNP-2-1up	0.112	0.001	2.07	-0.02
SYST-JET-GroupedNP-3-1down	0.105	-0.006	2.09	0
SYST-JET-GroupedNP-3-1up	0.113	0.002	2.07	-0.02
SYST-JET-JER-SINGLE-NP-1up	0.119	0.008	2.08	-0.01
SYST-MET-SoftTrk-ResoPara	0.106	-0.005	2.07	-0.02
SYST-MET-SoftTrk-ResoPerp	0.104	-0.007	2.07	-0.02
SYST-MET-SoftTrk-ScaleDown	0.113	0.002	2.07	-0.02
SYST-MET-SoftTrk-ScaleUp	0.103	-0.008	2.07	-0.02
SYST-PH-Iso-DDonoff	0.111	0	2.09	0

[*1] There are 88 nuisance parameters (NP) related to this factor. But those are reduced to 3 groups.

[*2] The photon isolation is corrected using a data-driven method with single photon and single electron events. The uncertainty is evaluated by turning off this correction. Therefore, only one systematic sample is evaluated for this factor.

For the systematic sources which have positive and negative variations, only larger effects are chosen for the calculation. The results are 13.3% in SRa, and 3.9% in SRd. The conservative one, 13.3%, is used as a total experimental uncertainty in the following discussion.

Then, the theoretical uncertainty is discussed. There are two types of the theoretical uncertainties; one affects the overall normalization. The other affects the shape of the kinematic distribution.

The theoretical uncertainties which affect the overall yields are related to the cross-section calculation. Following sources of the uncertainties related to the cross-section are taken into account.

- Effect from higher order QCD term (0.7% [63])
- PDFs and QCD scale uncertainty (0.7% [63])
- Branching fraction from H to diphoton (2.0% [64])

The total effect, which is evaluated by quadratic sum, is 3.6%. The quadratic sum of the overall experimental uncertainty (13.3%) and the overall theoretical uncertainty (3.6%) is the value (13.8%) used for the early selections.

The theoretical uncertainties which affect the shape of kinematic distributions are related to the modeling uncertainty. Those are evaluated by using MCs with the specific correction function described below. The sources taken into account are:

- PDFs uncertainty
- QCD scale factor
- Underlying event parton shower (UEPS)
- NLO electroweak corrections

The yields with those sources can be evaluated with the correction factor, which is a function of truth momentum of the vector boson. This type of uncertainty is evaluated only for the contribution of SM Wh, which is the main source of the peaking backgrounds ($\sim 90\%$). The evaluated yields and the systematics are summarized in Table 8.2. The overall uncertainty on the modeling, evaluated by quadratic sum, is 4.1%.

Finally, overall uncertainty, which is calculated by quadratic sum of three types of the uncertainties described above, is evaluated as 14.4%. Since it is confirmed that the uncertainties on the peaking backgrounds does not affect the results, rounded value, 15%, is chosen as the total uncertainties and used for the final selections.

8.3 Signal

For the uncertainty on the yields of the signals, only experimental uncertainty is taken into account. With the same manner described in the previous section, the experimental uncertainty is evaluated. First, the experimental uncertainties on the high-mass focus points are evaluated with LO samples. Since the results are around 6.4% to 8.6%, 15%, which is around twice of the estimated values, is used as a conservative tentative value. The tentative value is used for early selections.

Then, the same calculations have been performed for all the used signals with NLO samples, as shown in Figure 8.4 and 8.5. The evaluated uncertainties are distributed from 2% to 14%. No

Table8.2 Yields and systematic of SM Wh valuated by MCs with correction factors. In the case that the absolute value of evaluated systematic is smaller than 0.001, it is shown as 0.

Sources	SRa Yield	SRa systematics	SRd Yield	SRd systematics
Nominal	0.094		1.816	
QCD	0.092	-0.002	1.783	-0.033
PDF	0.094	0	1.809	-0.007
UEPS	0.097	+0.003	1.861	+0.045
NLO electroweak	0.095	-0.001	1.843	+0.027

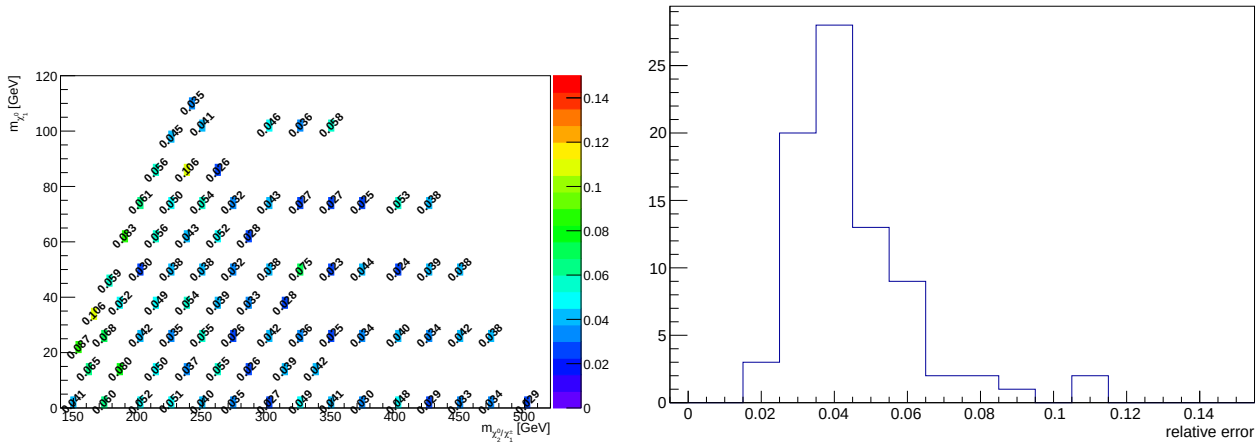

Figure8.4 Evaluated conservative uncertainty for the signal points with SRa selections in $(m_{\tilde{\chi}_1^\pm,\tilde{\chi}_2^0}, m_{\tilde{\chi}_1^0})$ space (left) and the projection of the evaluated values (right).

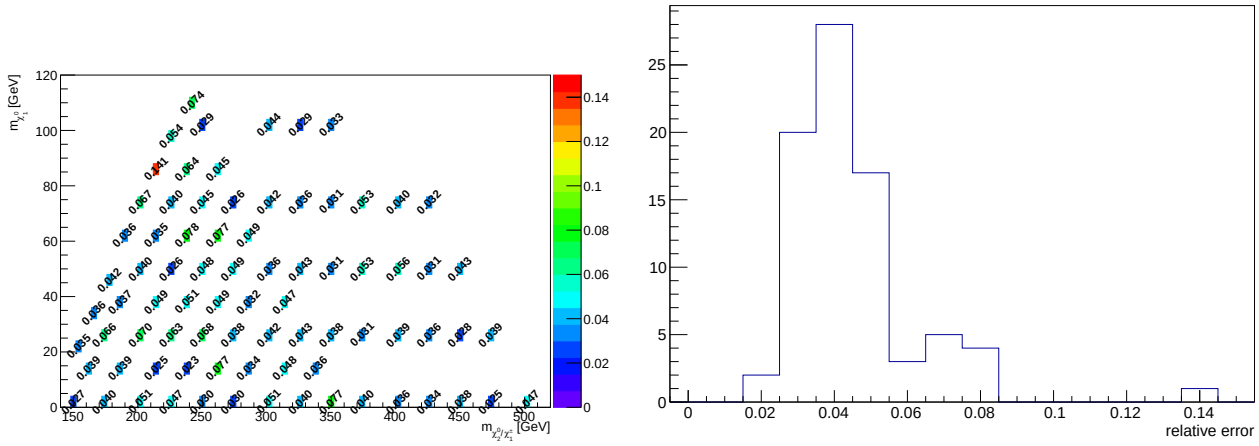

Figure8.5 Evaluated conservative uncertainty for the signal points with SRd selections in $(m_{\tilde{\chi}_1^\pm,\tilde{\chi}_2^0}, m_{\tilde{\chi}_1^0})$ space (left) and the projection of the evaluated values (right).

tendency related to LSP or NLSP mass is appeared in the 2D plots. Therefore, the information is summarized into 1D plots. From these 1D plots, it is suggested that relative uncertainties around 14% are outliers. Since 97% of the signals show relative uncertainties lower than 8%, 8% is chosen as the relative uncertainties on all signal samples and used for the final selections.

8.4 Expected exclusion upper limit

With the uncertainties described above, the upper limit of the excluded region is expected as following. The expected exclusion significances are re-evaluated with the final selections and with the toy method for all signal points, and then plotted to $(m_{\tilde{\chi}_1^\pm,\tilde{\chi}_2^0}, m_{\tilde{\chi}_1^0})$ space. The intermediate spaces between the used signal points are complemented by interpolation. Then, the contour line corresponding to the confidence level is taken from the plot as the expected upper limit of the exclusion region. In this analysis, standard 95% is used as the confidence level, which corresponds to 1.64σ. In the same manner, the error band is evaluated by replacing input numbers from mean to mean $\pm$ 1σ. The result is shown in Figure 8.6.

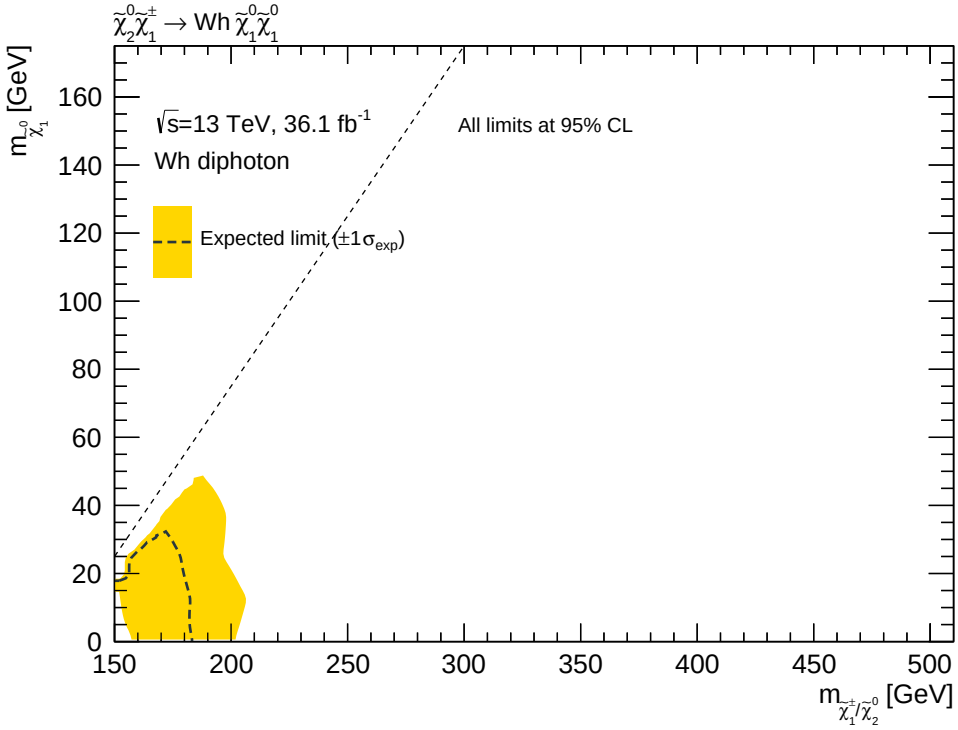

Figure8.6 Estimated expected exclusion upper limit for $\sigma_h = 15\%$ and $\sigma_s = 8\%$. Expected 95% CL exclusion regions in the $(m_{\tilde{\chi}_1^\pm,\tilde{\chi}_2^0}, m_{\tilde{\chi}_1^0})$ space in the simplified model, using 13 TeV data. The solid band around the expected limit shows the $\pm1\sigma_{\text{exp}}$ uncertainty band where all uncertainties including $\sigma_h = 15\%$ and $\sigma_s = 8\%$.

8.4.1 Comparison with 8 TeV analysis

Figure 8.7 shows the expected limit evaluated in 8 TeV analysis. As shown in the figure, the expected upper limit in the 8 TeV analysis is distributed around $m_{\tilde{\chi}_1^\pm,\tilde{\chi}_2^0} = 160$ GeV with 20.3 fb^{-1} data. On the other hand, the expected upper limit in the 13 TeV analysis is distributed around $m_{\tilde{\chi}_1^\pm,\tilde{\chi}_2^0} = 180$ GeV with 36.1 fb^{-1} data, as shown in Figure 8.6. This improvement on the expected limit is smaller than the naive expectation.

In order to understand this, the expected yields are normalized to the yields per fb^{-1}. The compared result is shown in Table 8.3. The yields in the 8 TeV analysis are taken from the high M_T region described in [19], which has similar definitions with the inclusive signal region in the 13 TeV analysis. The yields in the 13 TeV analysis is evaluated with the early selections. As shown in the table, the ratio of the yields per fb^{-1} is 1.3 between two analyses. However, the ratio is expected to be around two from the cross sections with the 8 TeV and the 13 TeV center of mass energies.

After the investigation about this difference, three possible sources were found. One is the differences on the used selection criteria. Although almost all criteria are the same between the 8 TeV analysis and the 13 TeV analysis, some criteria are tightened in the 13 TeV analysis, such as the isolation criterion for photon, the threshold on the momentum of sub-leading photon, the trigger and the b-jet veto. In order to evaluate the effect of those criteria, the yield of the low-mass signal in inclusive signal region in the 13 TeV analysis is re-evaluated with the criteria relaxed to the level used in 8 TeV analysis specifically as following:

- The isolation criterion was changed from topoEtcone40 $< 2.45\,\text{GeV} + 0.022 \times p_{\text{T}}(\gamma)$ to topoEtcone20 $< 0.065 \times p_{\text{T}}(\gamma)$ & ptcone20 $< 0.05 \times p_{\text{T}}(\gamma)$

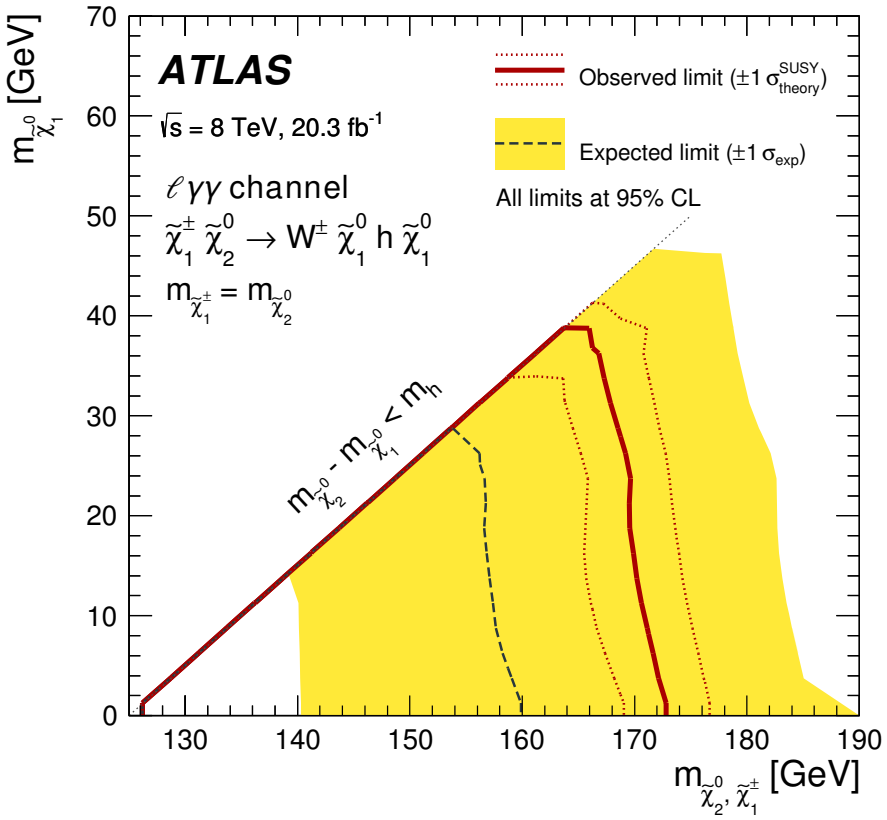

Figure8.7 Observed (solid line) and expected (dashed line) 95% CL exclusion regions in the mass plane of $m_{\tilde{\chi}_1^0}$ vs. $m_{\tilde{\chi}_1^{\pm},\tilde{\chi}_2^0}$ in the simplified model, using 8 TeV data, only for the diphoton channel. The dotted lines around the observed limit represent the results obtained when changing the nominal signal cross section up or down by the $\pm1\sigma^{\text{SUSY}}_{\text{theory}}$ theoretical uncertainty. The solid band around the expected limit shows the $\pm1\sigma_{\text{exp}}$ uncertainty band where all uncertainties, except those on the signal cross sections, are considered. The figure is cited from [19]

- The threshold on $p_{\text{T}}^{\gamma 2}$ was changed from 27 GeV to 20 GeV
- The b-jet veto and the trigger requirement were removed

Then, the yield per fb^{-1} of the low-mass signal in the 13 TeV analysis is increased from 0.313 to 0.364. With this yield, the ratio between two analyses is calculated as 1.5, which is still lower than 2.0 of theoretical expectation. Although these relaxed criteria achieve higher acceptance on signal, these cannot be used in the 13 TeV analysis due to much dense environment of events than the 8 TeV analysis.

Table8.3 Comparison between the 8 TeV and 13 TeV analyses of the numbers of expected events, per fb^{-1} of accumulated data, for peaking backgrounds, non-peaking backgrounds and focus-point signal events for the inclusive signal region.

Process	8 TeV Analysis, per fb^{-1}	13 TeV Analysis, per fb^{-1}	Ratio
SM Wh	0.044	0.061	1.4
Other peaking backgrounds	0.003	0.006	2.0
Non-peaking background	0.030	0.135	4.5
$(m_{\tilde{\chi}_1^{\pm},\tilde{\chi}_2^0}, m_{\tilde{\chi}_1^0}) = (150, 0)$ GeV	0.240	0.313	1.3

The second possible sources is the signal cross section used in the 8 TeV analyses. The MC samples for signals used in the 8 TeV analysis were generated without the hadronic tau decays where the tau is from W. However, the cross section used for the normalization was calculated by including it. This lead 30% over estimation on the yields of the signals in the 8 TeV analysis. If the yield of low-mass signal in the 8 TeV analysis is corrected for this over estimation factor, it becomes 0.185 from 0.240. With this corrected yield, the ratio between two analyses becomes 2.0 which is equivalent to the theoretical expectation.

The last possible source to make the improvement small is found on the evaluation of the non-peaking backgrounds. It is evaluated with sideband fit based on the observed events in higher or lower $m_{\gamma\gamma}$ region than the signal region in both the 8 TeV and the 13 TeV analyses. With $M_{\mathrm{T}}^{\mathrm{W}\gamma 1}$ and $M_{\mathrm{T}}^{\mathrm{W}\gamma 2}$ cuts are applied, 47% of the sideband events pass the selection in the 13 TeV analysis. On the other hand, only 17% of the events could pass the same selection in the 8 TeV analysis. According to the 8 TeV analysis, 48% of the events in the MC samples passed the same selection, which is the efficiency close to the efficiency of the 13 TeV data. This suggests that there are large down fluctuation in data in the 8 TeV analysis. Since the evaluation of the non-peaking backgrounds depends on the sideband data, the yield of the non-peaking backgrounds used in the calculation of the expected and the observed limits is smaller than the expectation from MC. Such inconsistency between data and MC is not seen in the 13 TeV analysis, thus the ratio of the yields of non-peaking backgrounds between two analyses are larger than the other components, as shown in Table 8.3.

The possible sources about the signal cross section and the estimation on non-peaking backgrounds suggests over estimation on the expected limit in the 8 TeV analyses. And it is possible that the over estimation is a part of the reasons of the relatively small improvement comparing to the naive expectation.

Chapter 9

Results

In this chapter, observed data in the signal region is shown. The observed data is compared with the expected backgrounds described in the previous chapters. The observed events are described in Section 9.1. The statistical evaluation for those observed events are performed in Section 9.2.

9.1 Observed events

After the estimation of the background described in above chapters, the blinded data in the signal region is opened. $m_{\gamma\gamma}$ distributions with unblinded data are shown in Figure 9.1 and 9.2. The numbers of observed events in the signal region are summarized in Table 9.1 with the expected yields. As shown in the table and the figures, two events in SRa and nine events in SRd are observed, while 0.36 events are expected in SRa and 5.35 events are expected in SRd. Therefore, the observed data in both signal regions are greater than the expected total yields of background.

In order to see the characteristics of the events in the SRs, their kinematic distributions are compared with the expectations. All details are shown in Appendix A. No strong bias which suggests that the excesses are due to miss modelling can be seen in the kinematic distributions.

The inconsistency between the SM expectations and the observed numbers is interpreted in two ways under following assumptions; it is due to the statistical fluctuation of the SM background, or it is due to the contributions of new physics. The former leads to the interpretation in terms of the exclusion limit of the model. The later leads to the interpretation in terms of the statistical significances. Those two interpretations are discussed in the next sections.

9.2 Observed upper limit

At first, the inconsistency is interpreted in terms of the statistical significances as following. The significances is evaluated by p_0 described in Section 7.2.3. In order to avoid any biases from the modeling of the signal, model independent p_0 is evaluated in SRa and SRd individually.

The evaluated p_0 is 2.7% in SRa and 8.6% in SRd, which are equivalent to 1.93σ in SRa and 1.36σ in SRd. From those evaluations, it is concluded that the inconsistency between the observed event and the expected yields of the backgrounds are not statistically significant. This is expected to be due to the large statistical uncertainty on non-peaking backgrounds. In other words, the mild excess is within a level of the statistical fluctuation.

Next, the interpretation in terms of the exclusion limit of the model is performed as following. p_μ with $\mu = 1$ is calculated with all signal points as described in Section 7.2.4. However, no signals assumed in this analysis could be excluded, due to the observed excess. Therefore, instead of excluding any signal models, the upper limit of the cross sections are evaluated for each signal point. The results are shown in Figure 9.3. In the figure, the upper limits of the cross section are shown by text, and the expected upper limit of the excluded model is also shown.

The model independent exclusion limit is calculated too. The results are interpreted to the upper limit on the signal yields (S^{95}) and the production of the cross section of the new physics and the

Table9.1 Expected numbers of peaking background, non-peaking background, and focus-point signal events for SRa and SRd. Here, the peaking background is fully broken down into its potential contributing components. Non-peaking-background uncertainty is dominated by the statistical uncertainty on the side-band fits. The peaking background uncertainties include both theoretical (production rate) and experimental (detector effect) contributions, as described in the text. The uncertainties on the "WH" and "Other peaking" backgrounds are taken to be fully correlated. Also shown are the observed numbers of events in SRa and SRd.

Process	SRa	SRd
SM Wh	0.094 ± 0.014	1.818 ± 0.273
SM Zh	0.011 ± 0.002	0.077 ± 0.012
SM $t\bar{t}h$	0.033 ± 0.005	0.113 ± 0.017
ggh	< 0.001	< 0.001
VBFh	< 0.001	0.001 ± 0.001
Total peaking background	0.138 ± 0.021	2.010 ± 0.302
Non-peaking background	0.22 ± 0.22	3.33 ± 0.90
Total background	0.36 ± 0.22	5.34 ± 0.95
Observed events	2	9
$(m_{\tilde{\chi}_1^\pm,\tilde{\chi}_2^0}, m_{\tilde{\chi}_1^0}) = (150, 0)$	2.87	6.57
$(m_{\tilde{\chi}_1^\pm,\tilde{\chi}_2^0}, m_{\tilde{\chi}_1^0}) = (250, 25)$	1.36	0.90
$(m_{\tilde{\chi}_1^\pm,\tilde{\chi}_2^0}, m_{\tilde{\chi}_1^0}) = (250, 100)$	0.95	0.90

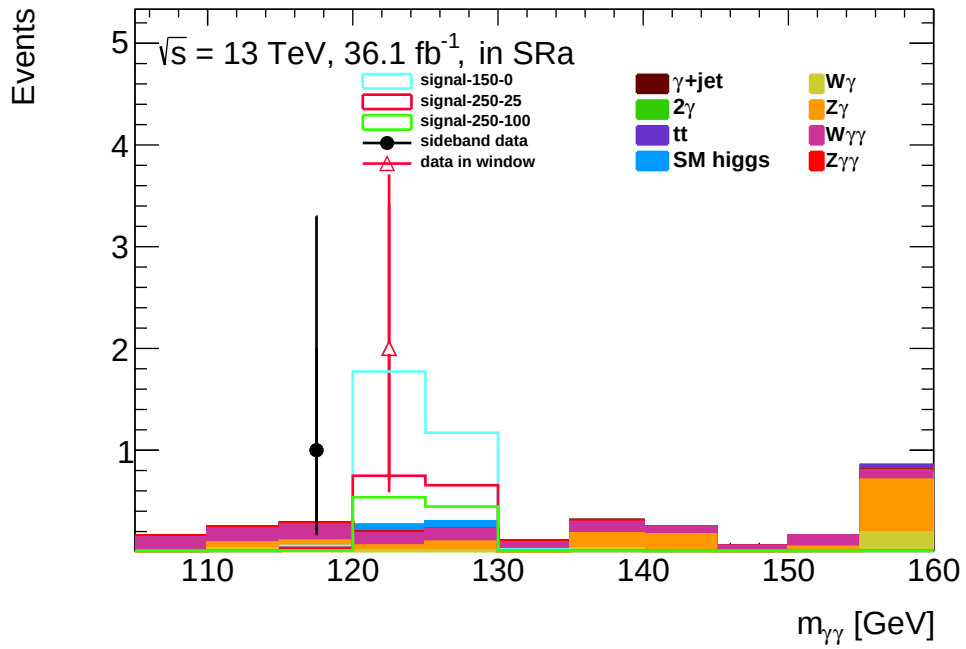

Figure9.1 $m_{\gamma\gamma}$ distribution of data and expected background and signals with SRa selection.

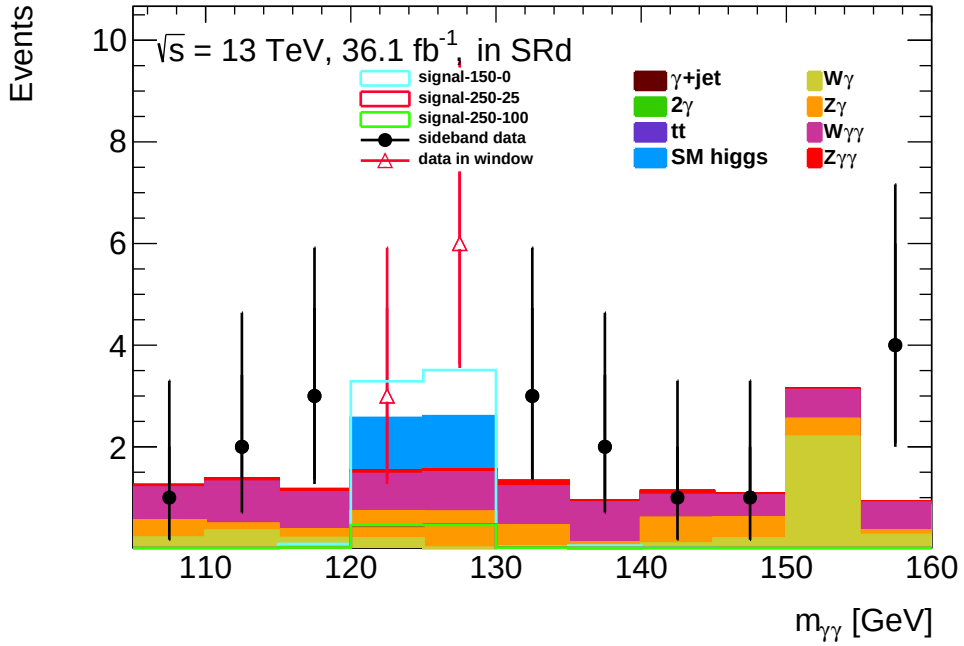

Figure9.2 $m_{\gamma\gamma}$ distribution of data and expected background and signals with SRd selection.

acceptance for that signal ($\langle\epsilon\sigma\rangle^{95}$). In Table 9.2, those results calculated with the number of observed events, and with the SM expected number are summarized with the discovery significances.

If the mild excesses came from new physics, it is going to be clear with higher statistical data.

9.3 Discussions

9.3.1 Best fit μ

The mild excess seen in Section 9.1 can be interpreted in terms of signal models with some assumed masses. With an assumption of the signal model, expected yields in SRa and SRd are estimated. The signal model which has expected yields close to the mild excess is considered as a "preferred" signal model. Such preferred signal model can be searched using the signal strength μ, which is defined in Section 7.2.1. μ is the normalization factor for signal model. If assumed model well explains the mild excess, best fit μ ($\hat{\mu}$), which is the μ value after fitting to data without any constraints, should be consist with 1.

Table9.2 Summary of the number of events expected from SM sources ($N^{\rm SM}_{\rm exp}$), and the observed number of events ($N_{\rm obs}$), for each SR. Also shown is the derived model-independent 95% CL limit ($S^{95}_{\rm obs}$) on the number of possible events from new physics, as well as both the observed ($\langle\epsilon\sigma\rangle^{95}_{\rm obs}$) and expected ($\langle\epsilon\sigma\rangle^{95}_{\rm exp}$) 95% CL limit on the visible cross section from new physics, assuming an integrated luminosity of 36.1 fb^{-1}.

Signal Region	$N_{\rm obs}$	$N^{\rm SM}_{\rm exp}$	$S^{95}_{\rm obs}$	$S^{95}_{\rm exp}$	$\langle\epsilon\sigma\rangle^{95}_{\rm obs}$[fb]	$\langle\epsilon\sigma\rangle^{95}_{\rm exp}$[fb]	Significance (p_0 value)
SRa	2	0.36 ± 0.22	5.7	$3.8^{+0.3}_{-0.1}$	0.158	$0.105^{+0.008}_{-0.003}$	1.93 (0.027)
SRd	9	5.34 ± 0.95	10.4	$6.1^{+3.2}_{-1.0}$	0.288	$0.169^{+0.089}_{-0.028}$	1.36 (0.086)

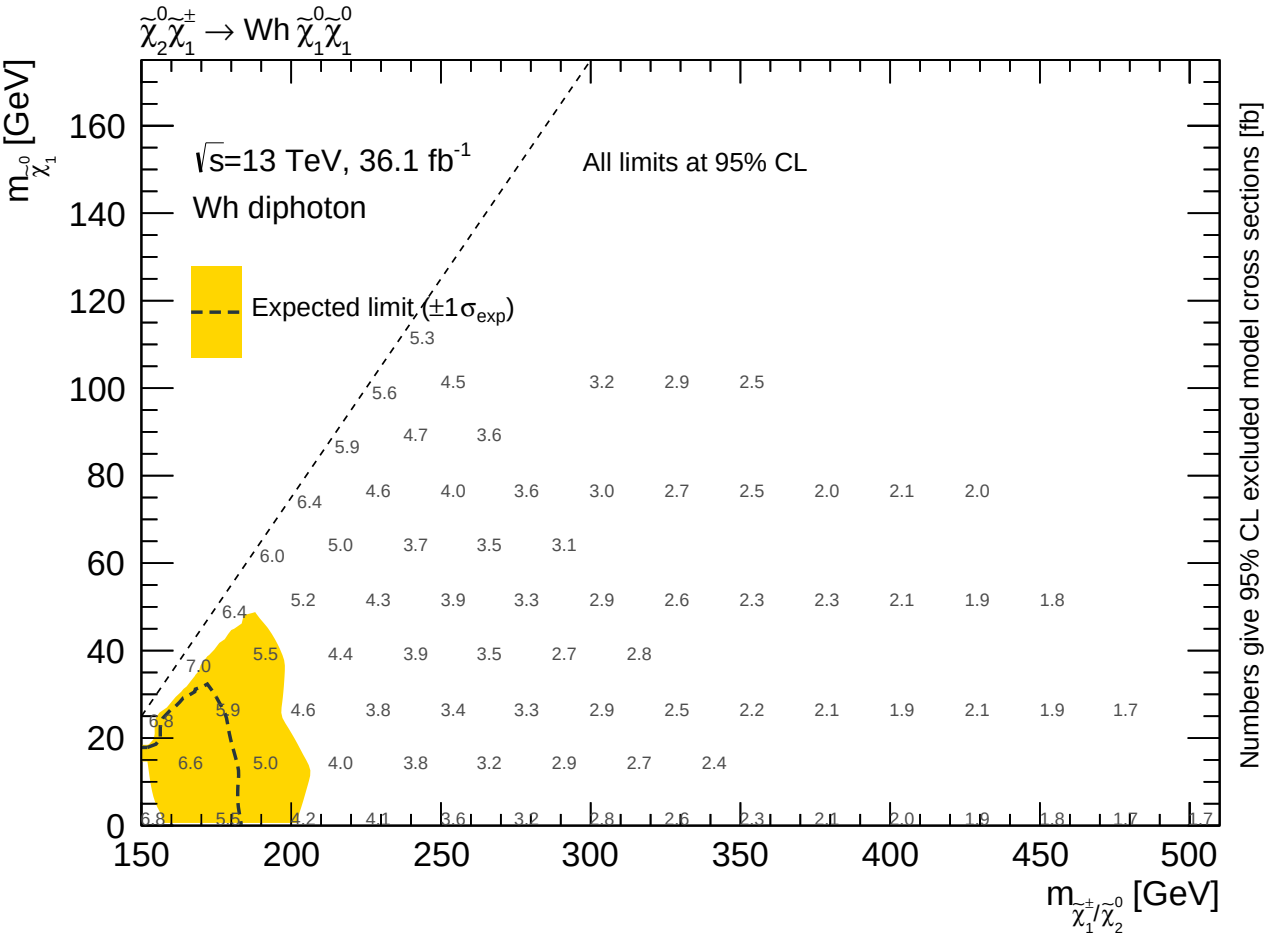

Figure9.3 Observed 95% CL upper limit on the cross section for wino-like gaugino production in the context of the model described in Section 1.2.3. Also shown is the expected 95% CL exclusion region. Due to the observed excesses in both SRa and SRd, no region in the parameter space of the model is excluded by the analysis.

Figure 9.5 shows calculated $\hat{\mu}$ for all signal models. From the figure, the region $m_{\tilde{\chi}_1^\pm,\tilde{\chi}_2^0} \sim 200$ GeV seems to be preferred.

However, there is large fitting error on $\hat{\mu}$ due to large statistical uncertainty. Deviations of $\hat{\mu}$ from 1 are divided by fitting error $((\hat{\mu}-1)/(\text{error on } \hat{\mu}))$ and summarized in Figure 9.6. As shown in the figure, most of points are within ±1. Those points are consistent with $\hat{\mu}=1$ within its fitting error. Therefore, preferred signal "region" spreads around from $m_{\tilde{\chi}_1^\pm,\tilde{\chi}_2^0} = 150$ GeV to $m_{\tilde{\chi}_1^\pm,\tilde{\chi}_2^0} = 350$ GeV.

Because of large statistical error, the preferred signal region spreads widely. However, Figure 9.5 and Figure 9.6 show some expected tendency; From light $m_{\tilde{\chi}_1^\pm,\tilde{\chi}_2^0}$ to heavy $m_{\tilde{\chi}_1^\pm,\tilde{\chi}_2^0}$, $\hat{\mu}$ is increased. This tendency came from the cross section differences described in Section 3.2.2.

Although it is hard to see in Figure 9.5, Figure 9.6 shows another clear tendency; The points of $m_{\tilde{\chi}_1^\pm,\tilde{\chi}_2^0} \sim 250$ GeV shows $(\hat{\mu}-1)/(\text{error on } \hat{\mu})$ from around 0.4 to 0.9. Since cross section, which depends on $m_{\tilde{\chi}_1^\pm,\tilde{\chi}_2^0}$, is similar for those points, this tendency came from the ratio of yields. In general, heavy $m_{\tilde{\chi}_1^0}$ leads to high yields in SRd because of large $E_{\mathrm{T}}^{\mathrm{miss}}$. In the case of $m_{\tilde{\chi}_1^\pm,\tilde{\chi}_2^0} \sim 250$ GeV, light $m_{\tilde{\chi}_1^0}$ is preferred rather than heavy $m_{\tilde{\chi}_1^0}$.

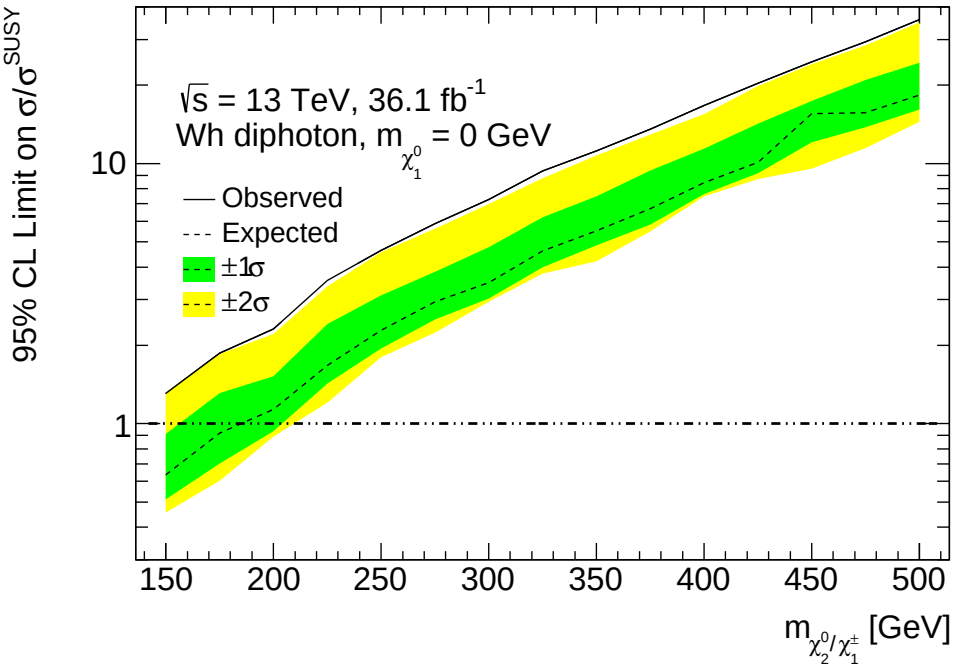

Figure9.4 Observed 95% CL upper limit on the cross section for wino-like gaugino production in the context of the model described in Section 1.2.3 for $m_{\tilde{\chi}_1^0} = 0$ GeV points. Also shown is the expected 95% CL exclusion limits with overall uncertainty.

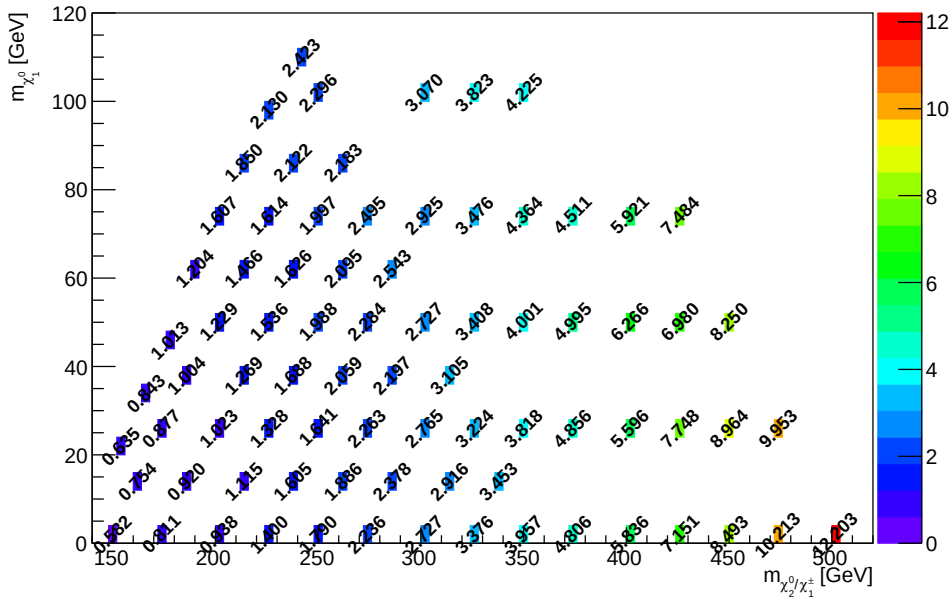

Figure9.5 $\hat{\mu}$ for wino-like gaugino production in the context of the model described in Section 1.2.3.

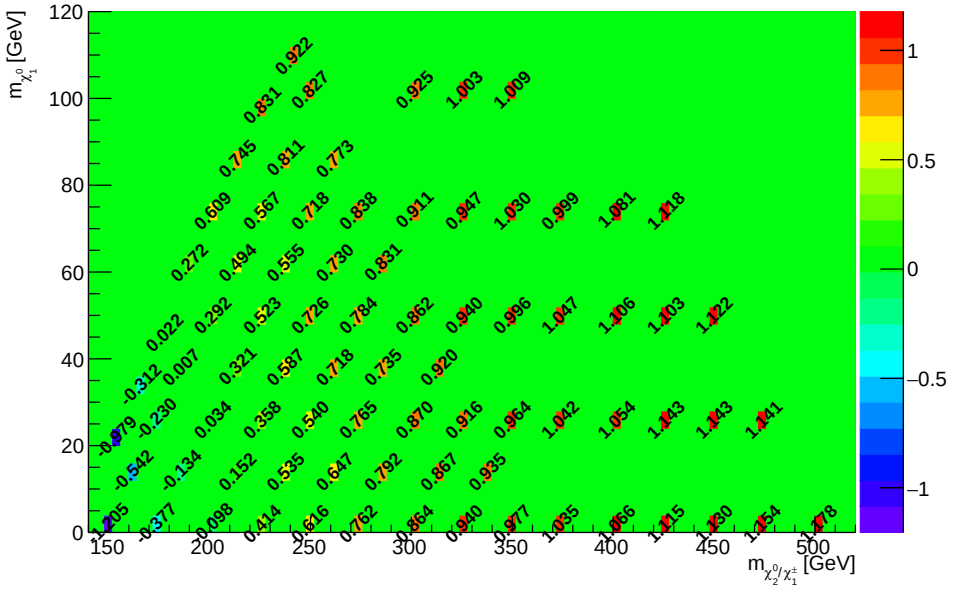

Figure9.6 $(\hat{\mu}-1)$/(error on $\hat{\mu}$) for wino-like gaugino production in the context of the model described in Section 1.2.3.

9.3.2 Expected observations in other channel

In case the mild excess is a sign of new physics, excess can be seen in other channel introduced in Section 1.2.3. As shown in Figure 1.6, the 3ℓ channel provided the second largest limit. In this section, expected observations in 3ℓ channel with the same data set is discussed.

For this discussion, following points are assumed:

- Signal acceptance is the same between 8 TeV analysis and 13 TeV analysis.
- Number of backgrounds is increased following the ratio of luminosity and the ratio of cross section of dominant process, which is $t\bar{t}$.
- The signal model is $(m_{\tilde{\chi}_1^\pm,\tilde{\chi}_2^0}, m_{\tilde{\chi}_1^0}) = (187.5, 12.5)$ GeV

Regarding the signal model, this point is chosen as the point of $\hat{\mu}$ closest to 1. As discussed in the previous subsection, the preferred region is from $m_{\tilde{\chi}_1^\pm,\tilde{\chi}_2^0} = 150$ GeV to $m_{\tilde{\chi}_1^\pm,\tilde{\chi}_2^0} = 350$ GeV. The cross section is decreased from 5.2 fb to 0.2 fb. The point assumed in this discussion have the cross section of 2.3 fb. Therefore, the estimation can be move from twice to 1/10.

In 3ℓ channel with 8 TeV data described in [65], the signal region called SR2τb is the typical signal region for Wh-mediated signal. The numbers used in that analysis is summarized in Table 9.3[*1] As shown in the table, expected signal (backgrounds) yields with 13 TeV data set is calculated as 6.44 (42.2) respectively. With those yields, asymmetric significance $S/\sqrt{B} = 0.99$ which is lower than that of the diphoton channel. It is caused by the large number of backgrounds in the 3ℓ channel. However, expected signal yield is larger than diphoton channel. Therefore, if backgrounds can be suppressed while keeping signal acceptance by improvement of the analysis procedure, significance can be larger than the diphoton channel. For 2σ observation only by the 3ℓ channel with 13 TeV data set, backgrounds need to be reduced below 10.4 events.

[*1] 5 events were observed in this region in 8 TeV analysis. When 7.2 backgrounds are expected, the probability that 5 or less events are observed is 28% from Poisson distribution. Therefore this mass point was not excluded in 8 TeV analysis.

Table9.3 Acceptance, cross sections and luminosity used in 3ℓ channel with 8 TeV data [65]. Cross sections with 13 TeV is also shown. Expected yields for 13 TeV data set are calculated from other numbers. For the calculations, signal acceptance with 13 TeV is assumed to be same with 8 TeV case. And expected yield of backgrounds is scaled using cross section ratios of $t\bar{t}$ and luminosity.

process	$\sqrt{s}$ [TeV]	cross section [pb]	luminosity [fb^{-1}]	acceptance	expected yields
signal	8	1.035	20.3	7.78×10^{-5}	1.63
	13	2.293	36.1	–	6.44 (calculated)
backgrounds	8	0.247 ($t\bar{t}$)	20.3	–	7.2
	13	0.816 ($t\bar{t}$)	36.1	–	42.2 (calculated)

Chapter 10

Conclusion

A search for direct production of electroweak gauginos decaying via Higgs boson and W boson is performed using 36.1 fb^{-1} of proton-proton collision data at $\sqrt{s} = 13$ TeV collected by the ATLAS detector at the LHC in 2015 and 2016. In this thesis, the channel where Higgs decays to diphoton and W decays to $\ell\nu$, such as

$$pp \to \tilde{\chi}_2^0 + \tilde{\chi}_1^\pm \to \tilde{\chi}_1^0 + h + \tilde{\chi}_1^0 + W \to \tilde{\chi}_1^0 + \gamma + \gamma + \tilde{\chi}_1^0 + \ell + \nu \tag{10.1}$$

is sought. Because of characteristics that mass reconstructed by diphoton is expected to have keen peak around the Higgs mass, expected SM backgrounds can be suppressed by the cut on diphoton mass. The background sources which can be suppressed by the diphoton mass cut are classified as non-peaking background, and the background sources which have Higgs in their process, meaning they cannot be suppressed by the diphoton mass cut, are classified as peaking backgrounds. Due to the low branching ratio from higgs to diphoton, expected signal yields are relatively low comparing to the other channels of electroweak gauginos searches. Therefore, statistical treatment is the key of this analysis.

For the event selection, exactly expected numbers of the reconstructed objects are required, such as exactly two photons, exactly one lepton and large missing transverse energy ($E_{\mathrm{T}}^{\mathrm{miss}}$). Selection criteria related to $E_{\mathrm{T}}^{\mathrm{miss}}$ are useful to suppress backgrounds since only signal event is expected to have large $E_{\mathrm{T}}^{\mathrm{miss}}$ bacause of $\tilde{\chi}_1^0$. Using $E_{\mathrm{T}}^{\mathrm{miss}}$, not only $E_{\mathrm{T}}^{\mathrm{miss}}$ cut, but also $M_{\mathrm{T}}^{\mathrm{W}\gamma 1}$ cut and $M_{\mathrm{T}}^{\mathrm{W}\gamma 2}$ are applied. In order to suppress non-peaking backgrounds as described above, $m_{\gamma\gamma}$ cut is applied. Regarding non-peaking backgrounds, W boson objects, which is reconstructed from $E_{\mathrm{T}}^{\mathrm{miss}}$ and lepton, and higgs object, which is reconstructed from diphoton, may not flay away back-to-back because of additional objects and miss-reconstructed objects. Therefore, $\Delta\phi(\mathrm{W}, \mathrm{h})$ cut is applied to reduce contributions of non-peaking backgrounds. One new criterion, b-jet veto is introduced. It can reduce one of the major peaking background sources, SM $t\bar{t}h$ background. This new criterion improves significance by $\sim$10%.

After the event selection, yields of the backgrounds and the signals are evaluated. In order to avoid uncertainty from MC simulations, the non-peaking backgrounds are evaluated using sideband data with data-driven method, The method is validated based on possible assumptions and confirmed for its stability. The yields of the peaking backgrounds and signals are evaluated using MC simulations. Because of large statistical error on the non-peaking backgrounds, systematical uncertainty of the evaluations using MCs are confirmed to be small enough not to affect the results.

Based on the evaluated yields, the signal region is further optimized. Because of very similar kinematical characteristics of signals and SM Wh background, typical cut-base selection cannot improve significance. In order to enhance significance without losing signal acceptance, the signal region is divided into two regions, SRa and SRd. The optimization of the dividing thresholds is performed by maximizing expected discovery significances. This optimization achieves $\sim$ 300% of improvement in significance at maximum.

The expected limit of model exclusion is evaluated using the optimized signal region. Evaluated limit is distributed around $m_{\tilde{\chi}_1^\pm, \tilde{\chi}_2^0} = 180$ GeV. This is improved form $m_{\tilde{\chi}_1^\pm, \tilde{\chi}_2^0} = 160$ GeV of the

limit evaluated in the 8 TeV analysis. The improvement is not significant. It is suggested that there are possible sources of over estimation in the 8 TeV analysis found out by the detailed comparisons between this and the 8 TeV analyses.

After setting the expected limit, collected data is compared with the expectation in the signal region. There are two events in SRa and nine events in SRd, while 0.36 ± 0.22 and 5.35 ± 0.95 events are expected in SRa and SRd respectively. This mild excess is equivalent to 1.93σ deviation and 1.36σ deviation in SRa and SRd respectively. Those statistical values suggest that there are mild excesses in both signal regions, but the mild excess is within a level of the statistical fluctuation. On the other hand, due to these mild excesses, any signal model points assumed in this analysis cannot be excluded. Instead, upper limit of the cross section of the wino-like gaugino pair productions are calculated. Also, model independent exclusion limit on the signal yields is evaluated. The evaluated upper limit of yields are 5.7 fb in SRa and 10.4 fb in SRd. The dominant uncertainty is statistical error on the non-peaking background.

This result may suggest that there are still a room for the new physics assumed in this thesis. If it exists and the mild excess is from such physics, the mild excess between the expectation and data would be clear with more luminosity.

If the mild excess is interpreted as a sign of new physics, the preferred signal model evaluated from the best fit μ ($\hat{\mu}$) are from $m_{\tilde{\chi}_1^\pm, \tilde{\chi}_2^0} = 150$ GeV to $m_{\tilde{\chi}_1^\pm, \tilde{\chi}_2^0} = 350$ GeV. The wide region is due to large statistical uncertainty.

The mild excess is used to predict the expectation of the 3ℓ channel with 13 TeV data set. This calculation is performed by extrapolating the 8 TeV analysis results. Expected asymmetric significance is 0.99σ.

Acknowledgements

I would like to express the deepest appreciation to my supervisor, Associate Professor Osamu Jinnouchi. I joined his laboratory 6 years ago. But even before that period, he showed me how physics is attractive through an interview he kindly accepted. After I joined his laboratory, he gave me many challenging topics. Without those experiences, I could not learn the skills I have acquired so far. And especially the study described in this thesis would not have been finished. It was so challenging because of the small analysis group and limited time. He spent so much time for the discussion with me about this topic, and suggested so many great ideas. His kind help drives the analysis.

I would like to express my gratitude to Professor Bruce Schumm, who is the convener of the diphoton analysis group. He collected the results to form a paper and suggested what we need. Also his pointed question changed stacked situation many times. Thanks to his help, the analysis is going to be published. I would like to thank the members of the diphoton analysis group.

I would like to thank to Dr. Alberto Cervelli and Dr. Jeanette Lorenz, who are the conveners of the Wh analysis group. They helped discussions about analysis procedure. And their technical helps are necessary for the analysis.

I would like to show my appreciation to Dr. Yohei Yamaguchi, who was a staff of Jinnouchi Lab. Especially during my stay at CERN, he supervised me so kindly. I believe my stay could not go smooth without him.

I would like to thank Assistant Professor Yosuke Takubo, who is a Pixel project leader, for his help about my tasks related to the inner detector from when I was a master student. He supervised me about detector study, and also invited me for many joyful events. His kind help is one of the reasons I decided to dive into academic world.

I would like to thank Professor Masahiro Kuze who is my sub-supervisor, for his interesting lecture and suggestive discussion.

I would like to thank all the members of Jinnouchi Lab for joyful lab life. Especially to Dr. Daiki Yamaguchi, Dr. Ryo Nagai, Dr. Nora Pettersson and Dr. Kazuki Motohashi.

I would like to thank house mates at CERN, Satoshi Higashino, Dr. Shunsuke Honda, Takuya Honda and Kosuke Takeda. They gave me many good memories.

This work was supported by JSPS KAKENHI Grant Number JP16J0774.

Finnally, I would like to thank my family for their supports, I would like to thank Ai Shitaba, who is my fiancée, for making my life so happy.

Bibliography

[1] Murray Gell-Mann. "A Schematic Model of Baryons and Mesons". In: *Phys. Lett.* 8 (1964), pp. 214–215. DOI: 10.1016/S0031-9163(64)92001-3.

[2] Steven Weinberg. "A Model of Leptons". In: *Phys. Rev. Lett.* 19 (1967), pp. 1264–1266. DOI: 10.1103/PhysRevLett.19.1264.

[3] Abdus Salam. "Weak and Electromagnetic Interactions". In: *Conf. Proc.* C680519 (1968), pp. 367–377.

[4] S. L. Glashow, J. Iliopoulos, and L. Maiani. "Weak Interactions with Lepton-Hadron Symmetry". In: *Phys. Rev.* D2 (1970), pp. 1285–1292. DOI: 10.1103/PhysRevD.2.1285.

[5] ATLAS Collaborations. *Summary plots from the ATLAS Standard Model physics group.* https://atlas.web.cern.ch/Atlas/GROUPS/PHYSICS/CombinedSummaryPlots/SM/.

[6] Georges Aad et al. "Observation of a new particle in the search for the Standard Model Higgs boson with the ATLAS detector at the LHC". In: *Phys. Lett.* B716 (2012), pp. 1–29. DOI: 10.1016/j.physletb.2012.08.020. arXiv: 1207.7214 [hep-ex].

[7] Serguei Chatrchyan et al. "Observation of a new boson at a mass of 125 GeV with the CMS experiment at the LHC". In: *Phys. Lett.* B716 (2012), pp. 30–61. DOI: 10.1016/j.physletb.2012.08.021. arXiv: 1207.7235 [hep-ex].

[8] Morad Aaboud et al. "Measurement of the Higgs boson mass in the $H \to ZZ^* \to 4\ell$ and $H \to \gamma\gamma$ channels with $\sqrt{s} = 13$ TeV pp collisions using the ATLAS detector". In: (2018). arXiv: 1806.00242 [hep-ex].

[9] P. A. R. Ade et al. "Planck 2015 results. XIII. Cosmological parameters". In: *Astron. Astrophys.* 594 (2016), A13. DOI: 10.1051/0004-6361/201525830. arXiv: 1502.01589 [astro-ph.CO].

[10] Stephen P. Martin. "A Supersymmetry primer". In: (1997). [Adv. Ser. Direct. High Energy Phys.18,1(1998)], pp. 1–98. DOI: 10.1142/9789812839657_0001,10.1142/9789814307505_0001. arXiv: hep-ph/9709356 [hep-ph].

[11] K. Abe et al. "Search for proton decay via $p \to e^+\pi^0$ and $p \to \mu^+\pi^0$ in 0.31megatonyears exposure of the Super-Kamiokande water Cherenkov detector". In: *Phys. Rev.* D95.1 (2017), p. 012004. DOI: 10.1103/PhysRevD.95.012004. arXiv: 1610.03597 [hep-ex].

[12] R. Barbier et al. "R-parity violating supersymmetry". In: *Phys. Rept.* 420 (2005), pp. 1–202. DOI: 10.1016/j.physrep.2005.08.006. arXiv: hep-ph/0406039 [hep-ph].

[13] A. Djouadi et al. "The Minimal supersymmetric standard model: Group summary report". In: *GDR (Groupement De Recherche) - Supersymetrie Montpellier, France, April 15-17, 1998.* 1998. arXiv: hep-ph/9901246 [hep-ph]. URL: https://inspirehep.net/record/481987/files/arXiv:hep-ph_9901246.pdf.

[14] Andrea Ventura. "Searches for supersymmetry". In: *Int. J. Mod. Phys. Conf. Ser.* 46 (2018), p. 1860006. DOI: 10.1142/S2010194518600066. arXiv: 1711.00152 [hep-ex].

[15] ATLAS Collaborations. *Summary plots from the ATLAS Supersymmetry physics group.* https://atlas.web.cern.ch/Atlas/GROUPS/PHYSICS/CombinedSummaryPlots/SUSY/.

[16] Morad Aaboud et al. "Search for dark matter and other new phenomena in events with an energetic jet and large missing transverse momentum using the ATLAS detector". In: *JHEP* 01 (2018), p. 126. DOI: 10.1007/JHEP01(2018)126. arXiv: 1711.03301 [hep-ex].

[17] Benjamin Fuks et al. "Gaugino production in proton-proton collisions at a center-of-mass energy of 8 TeV". In: *JHEP* 10 (2012), p. 081. DOI: 10.1007/JHEP10(2012)081. arXiv: 1207.2159 [hep-ph].

[18] Georges Aad et al. "Search for direct production of charginos, neutralinos and sleptons in final states with two leptons and missing transverse momentum in pp collisions at $\sqrt{s} = 8$ TeV with the ATLAS detector". In: *JHEP* 05 (2014), p. 071. DOI: 10.1007/JHEP05(2014)071. arXiv: 1403.5294 [hep-ex].

[19] ATLAS Collaboration. "Search for direct pair production of a chargino and a neutralino decaying to the 125 GeV Higgs boson in $\sqrt{s} = 8$ TeV pp collisions with the ATLAS detector". In: *Eur. Phys. J. C* 75 (2015), p. 208. DOI: 10.1140/epjc/s10052-015-3408-7. arXiv: 1501.07110 [hep-ex].

[20] Kiel Howe and Prashant Saraswat. "Excess Higgs Production in Neutralino Decays". In: *JHEP* 10 (2012), p. 065. DOI: 10.1007/JHEP10(2012)065. arXiv: 1208.1542 [hep-ph].

[21] Georges Aad et al. "Search for the electroweak production of supersymmetric particles in $\sqrt{s}$=8 TeV pp collisions with the ATLAS detector". In: *Phys. Rev.* D93.5 (2016), p. 052002. DOI: 10.1103/PhysRevD.93.052002. arXiv: 1509.07152 [hep-ex].

[22] Kazuki Yajima. "Performance and description of the upgraded readout with the new back-end electronics for the ATLAS Pixel detector". In: (2017). URL: http://cds.cern.ch/record/2252813.

[23] Cinzia De Melis. "The CERN accelerator complex. Complexe des acéclérateurs du CERN". In: (2016). General Photo. URL: https://cds.cern.ch/record/2119882.

[24] Lyndon Evans and Philip Bryant. "LHC Machine". In: *JINST* 3 (2008), S08001. DOI: 10.1088/1748-0221/3/08/S08001.

[25] G. Aad et al. "The ATLAS Experiment at the CERN Large Hadron Collider". In: *JINST* 3 (2008), S08003. DOI: 10.1088/1748-0221/3/08/S08003.

[26] Karolos Potamianos. "The upgraded Pixel detector and the commissioning of the Inner Detector tracking of the ATLAS experiment for Run-2 at the Large Hadron Collider". In: *PoS* EPS-HEP2015 (2015), p. 261. arXiv: 1608.07850 [physics.ins-det].

[27] Morad Aaboud et al. "Study of the material of the ATLAS inner detector for Run 2 of the LHC". In: *JINST* 12.12 (2017), P12009. DOI: 10.1088/1748-0221/12/12/P12009. arXiv: 1707.02826 [hep-ex].

[28] Morad Aaboud et al. "Performance of the ATLAS Trigger System in 2015". In: *Eur. Phys. J.* C77.5 (2017), p. 317. DOI: 10.1140/epjc/s10052-017-4852-3. arXiv: 1611.09661 [hep-ex].

[29] ATLAS Collaborations. *LuminosityPublicResultsRun2*. https://twiki.cern.ch/twiki/bin/view/AtlasPublic/LuminosityPublicResultsRun2.

[30] Fernando Monticelli. "The Upgrade of the ATLAS Electron and Photon Triggers for LHC Run 2 and their Performance". In: *PoS* ICHEP2016 (2016), p. 246.

[31] S. Agostinelli et al. "GEANT4: A Simulation toolkit". In: *Nucl. Instrum. Meth.* A506 (2003), pp. 250–303. DOI: 10.1016/S0168-9002(03)01368-8.

[32] John Allison et al. "Geant4 developments and applications". In: *IEEE Trans. Nucl. Sci.* 53 (2006), p. 270. DOI: 10.1109/TNS.2006.869826.

[33] T. Gleisberg et al. "Event generation with SHERPA 1.1". In: *JHEP* 02 (2009), p. 007. DOI: 10.1088/1126-6708/2009/02/007. arXiv: 0811.4622 [hep-ph].

[34] Hung-Liang Lai et al. "New parton distributions for collider physics". In: *Phys. Rev. D* 82 (2010), p. 074024. DOI: 10.1103/PhysRevD.82.074024. arXiv: 1007.2241 [hep-ph].

[35] Stefano Frixione, Paolo Nason, and Carlo Oleari. "Matching NLO QCD computations with Parton Shower simulations: the POWHEG method". In: *JHEP* 11 (2007), p. 070. DOI: 10.1088/1126-6708/2007/11/070. arXiv: 0709.2092 [hep-ph].

[36] Torbjorn Sjöstrand, Stephen Mrenna, and Peter Z. Skands. "PYTHIA 6.4 Physics and Manual". In: *JHEP* 05 (2006), p. 026. DOI: 10.1088/1126-6708/2006/05/026. arXiv: hep-ph/0603175.

[37] Peter Zeiler Skands. "Tuning Monte Carlo Generators: The Perugia Tunes". In: *Phys. Rev. D* 82 (2010), p. 074018. DOI: 10.1103/PhysRevD.82.074018. arXiv: 1005.3457 [hep-ph].

[38] Torbjorn Sjöstrand, Stephen Mrenna, and Peter Z. Skands. "A Brief Introduction to PYTHIA 8.1". In: *Comput. Phys. Commun.* 178 (2008), pp. 852–867. DOI: 10.1016/j.cpc.2008.01.036. arXiv: 0710.3820 [hep-ph].

[39] Richard D. Ball et al. "Parton distributions with LHC data". In: *Nucl. Phys.* B867 (2013), pp. 244–289. DOI: 10.1016/j.nuclphysb.2012.10.003. arXiv: 1207.1303 [hep-ph].

[40] Richard D. Ball et al. "Parton distributions with QED corrections". In: *Nucl. Phys. B* 877 (2013), pp. 290–320. DOI: 10.1016/j.nuclphysb.2013.10.010. arXiv: 1308.0598 [hep-ph].

[41] ATLAS Collaboration. *ATLAS Pythia 8 tunes to* 7 *TeV data*. ATL-PHYS-PUB-2014-021. 2014. URL: https://cds.cern.ch/record/1966419.

[42] Georges Aad et al. "Measurement of the Z/γ^* boson transverse momentum distribution in pp collisions at $\sqrt{s} = 7$ TeV with the ATLAS detector". In: *JHEP* 09 (2014), p. 145. DOI: 10.1007/JHEP09(2014)145. arXiv: 1406.3660 [hep-ex].

[43] J. Alwall et al. "The automated computation of tree-level and next-to-leading order differential cross sections, and their matching to parton shower simulations". In: *JHEP* 07 (2014), p. 079. DOI: 10.1007/JHEP07(2014)079. arXiv: 1405.0301 [hep-ph].

[44] M. Bahr et al. "Herwig++ Physics and Manual". In: *Eur. Phys. J. C* 58 (2008), p. 639. DOI: 10.1140/epjc/s10052-008-0798-9. arXiv: 0803.0883 [hep-ph].

[45] Michael H. Seymour and Andrzej Siodmok. "Constraining MPI models using σ_{eff} and recent Tevatron and LHC Underlying Event data". In: *JHEP* 10 (2013), p. 113. DOI: 10.1007/JHEP10(2013)113. arXiv: 1307.5015 [hep-ph].

[46] J. Alwall et al. "The automated computation of tree-level and next-to-leading order differential cross sections, and their matching to parton shower simulations". In: *JHEP* 2014 (2014), p. 158. DOI: 10.1007/JHEP07(2014)079. arXiv: 1405.0301 [hep-ph].

[47] E Torró Pastor, D Côté, and X Portell Bueso. *Validation of the ATLFAST-II package for the simulation of supersymmetry events*. Tech. rep. ATL-COM-PHYS-2011-1181. Geneva: CERN, 2011. URL: https://cds.cern.ch/record/1379479.

[48] M. Aaboud et al. "Performance of the ATLAS Track Reconstruction Algorithms in Dense Environments in LHC Run 2". In: *Eur. Phys. J.* C77.10 (2017), p. 673. DOI: 10.1140/epjc/s10052-017-5225-7. arXiv: 1704.07983 [hep-ex].

[49] *Performance of primary vertex reconstruction in proton-proton collisions at $\sqrt{s}$ =7 TeV in the ATLAS experiment*. Tech. rep. ATLAS-CONF-2010-069. Geneva: CERN, 2010. URL: https://cds.cern.ch/record/1281344.

[50] W Lampl et al. *Calorimeter Clustering Algorithms: Description and Performance*. Tech. rep. ATL-LARG-PUB-2008-002. ATL-COM-LARG-2008-003. Geneva: CERN, 2008. URL: https://cds.cern.ch/record/1099735.

[51] Christos Anastopoulos et al. *Photon identification pre-recommendations for run 2*. https://cds.cern.ch/record/2022342. Geneva, 2015.

[52] *Electron efficiency measurements with the ATLAS detector using the 2015 LHC proton-proton collision data*. Tech. rep. ATLAS-CONF-2016-024. Geneva: CERN, 2016. URL: https://cds.cern.ch/record/2157687.

[53] Georges Aad et al. "Muon reconstruction performance of the ATLAS detector in proton 寰苑 roton collision data at $\sqrt{s}$ =13 TeV". In: *Eur. Phys. J.* C76.5 (2016), p. 292. DOI: 10.1140/epjc/s10052-016-4120-y. arXiv: 1603.05598 [hep-ex].

[54] Matteo Cacciari, Gavin P. Salam, and Gregory Soyez. "The Anti-k(t) jet clustering algorithm". In: *JHEP* 04 (2008), p. 063. DOI: 10.1088/1126-6708/2008/04/063. arXiv: 0802.1189 [hep-ph].

[55] Georges Aad et al. "Topological cell clustering in the ATLAS calorimeters and its performance in LHC Run 1". In: *Eur. Phys. J.* C77 (2017), p. 490. DOI: 10.1140/epjc/s10052-017-5004-5. arXiv: 1603.02934 [hep-ex].

[56] *Tagging and suppression of pileup jets with the ATLAS detector*. Tech. rep. ATLAS-CONF-2014-018. Geneva: CERN, 2014. URL: http://cds.cern.ch/record/1700870.

[57] *Selection of jets produced in 13TeV proton-proton collisions with the ATLAS detector*. Tech. rep. ATLAS-CONF-2015-029. Geneva: CERN, 2015. URL: https://cds.cern.ch/record/2037702.

[58] *Expected performance of the ATLAS b-tagging algorithms in Run-2*. Tech. rep. ATL-PHYS-PUB-2015-022. Geneva: CERN, 2015. URL: http://cds.cern.ch/record/2037697.

[59] Giacinto Piacquadio and Christian Weiser. "A new inclusive secondary vertex algorithm for b-jet tagging in ATLAS". In: *J. Phys. Conf. Ser.* 119 (2008), p. 032032. DOI: 10.1088/1742-6596/119/3/032032.

[60] *Performance of Missing Transverse Momentum Reconstruction in ATLAS studied in Proton-Proton Collisions recorded in 2012 at 8 TeV*. Tech. rep. ATLAS-CONF-2013-082. Geneva: CERN, 2013. URL: http://cds.cern.ch/record/1570993.

[61] Georges Aad et al. "Jet energy measurement with the ATLAS detector in proton-proton collisions at $\sqrt{s} = 7$ TeV". In: *Eur. Phys. J.* C73.3 (2013), p. 2304. DOI: 10.1140/epjc/s10052-013-2304-2. arXiv: 1112.6426 [hep-ex].

[62] Glen Cowan et al. "Asymptotic formulae for likelihood-based tests of new physics". In: *Eur.Phys.J.* C71 (July 2010), p. 1554. DOI: 10.1140/epjc/s10052-011-1554-0. arXiv: 1007.1727.

[63] ATLAS Collaboration. *Supporting documentation : Probing Higgs production modes and couplings with the $H \to \gamma\gamma$ channel with the Run 2 of LHC in the ATLAS experiment*. ATL-COM-PHYS-2016-1784. 2017. URL: https://cds.cern.ch/record/2238687/files/ATL-COM-PHYS-2016-1784.pdf.

[64] Pieri, Marco. *SM Higgs Branching Ratios and Total Decay Widths*. Update in CERN Report 4, 2016. 2016. URL: https://twiki.cern.ch/twiki/bin/view/LHCPhysics/CERNYellowReportPageBR.

[65] Georges Aad et al. "Search for direct production of charginos and neutralinos in events with three leptons and missing transverse momentum in $\sqrt{s} = 8$TeV pp collisions with the ATLAS detector". In: *JHEP* 04 (2014), p. 169. DOI: 10.1007/JHEP04(2014)169. arXiv: 1402.7029 [hep-ex].

AppendixA

Kinematic distributions in signal region

TableA.1 Photon characteristics for the 11 signal events (GeV and mm units). The first two events fell into SRa and the final nine in SRd. "Iso" refers to the value of the topEtCone40 variable. R_{conv} shows the radius of conversion vertex. For converted photons, it is classified as type 1 (one track only with Si hits), type 2 (one track only with no Si hits), type 3 (two tracks both with Si hits), or type 5 (two tracks and only one with Si hits).

		Leading Photon				Subleading Photon			
Run	Event	p_{T}	(η,ϕ)	R_{conv} (Type)	Iso	p_{T}	(η,ϕ)	R_{conv} (Type)	Iso
282712	922772599	155.5	(0.3,-0.9)	297 (1)	5.38	72.3	(0.0,-2.1)	Unvonv	0.21
303892	4127378101	98.0	(0.3,-1.0)	48 (3)	0.55	32.2	(1.7,-2.9)	320 (5)	0.04
280423	81213163	85.9	(1.1,-1.3)	632 (2)	-1.24	69.0	(0.0,-2.6)	Unconv	0.02
300863	1002432542	68.0	(0.8,1.5)	Unconv	1.50	36.7	(-0.2,-1.2)	Unconv	-0.95
301973	567913060	74.4	(-0.6,1,1)	630 (2)	1.49	56.8	(-1.1,-1.4)	Unconv	2.52
302380	473324458	171.2	(-0.7,-3.0)	Unconv	-2.17	94.0	(-0.3,2.4)	Unconv	0.36
303208	5060330829	71.9	(-0.4,-0.8)	Unconv	1.98	32.5	(1.1,2.6)	Unconv	-2.04
304008	2769513232	133.4	(0.7,2.6)	Unconv	1.09	94.5	(0.1,-2.7)	49 (3)	2.95
309640	4285889264	104.0	(-0.5,0.8)	Unconv	-1.24	51.3	(0.1.,2.7)	Unconv	1.32
310341	1548645619	77.8	(0.9,-2.7)	Unconv	-2.55	55.1	(-0.6,2.7)	Unconv	-0.08
310863	337227316	122.9	(-1.7,1.1)	Unconv	2.14	52.9	(-1.8,2.9)	Unconv	-0.03

TableA.2 Lepton,jet and event characteristics for the 11 signal events (GeV units). The first two events fell into SRa and the final nine in SRd.

		Lepton			Leading jet		Subleading Jet			
Run	Event	Type	p_{T}	(η,ϕ)	p_{T}	(η,ϕ)	p_{T}	(η,ϕ)	$E_{\mathrm{T}}^{\mathrm{miss}}$	$\langle\mu\rangle$
282712	922772599	e	26.6	(-0.4,-2.3)	78.0	(1.4,1.8)	43.8	(2.6,-1.5)	163.4	14.8
303892	4127378101	e	99.0	(2.0,1.6)	—	—	—	—	66.4	16.6
280423	81213163	e	67.9	(1.7,0.9)	34.7	(1.8,0.4)	—	—	58.8	16.9
300863	1002432542	μ	33.8	(-0.7,2.4)	66.6	(2.6,0.1)	—	—	82.4	22.5
301973	567913060	e	38.9	(-1.0,3.0)	—	—	—	—	66.9	25.4
302380	473324458	μ	120.4	(-0.5,-0.3)	—	—	—	—	143.0	27.8
303208	5060330829	e	35.7	(-0.7,-2.1)	38.5	(-1.0,0.4)	—	—	54.4	16.6
304008	2769513232	μ	158.0	(0.8,0.1)	—	—	—	—	64.6	23.4
309640	4285889264	μ	55.7	(1.7,-2.1)	125.7	(-1,5.1.0)	50.9	(-2.7,-2.4)	64.8	23.6
310341	1548645619	μ	25.9	(1.0,-1.0)	—	—	—	—	115.5	29.3
310863	337227316	μ	27.9	(0.7,-2.6)	210.2	(0.1,1.7)	—	—	253.8	41.9

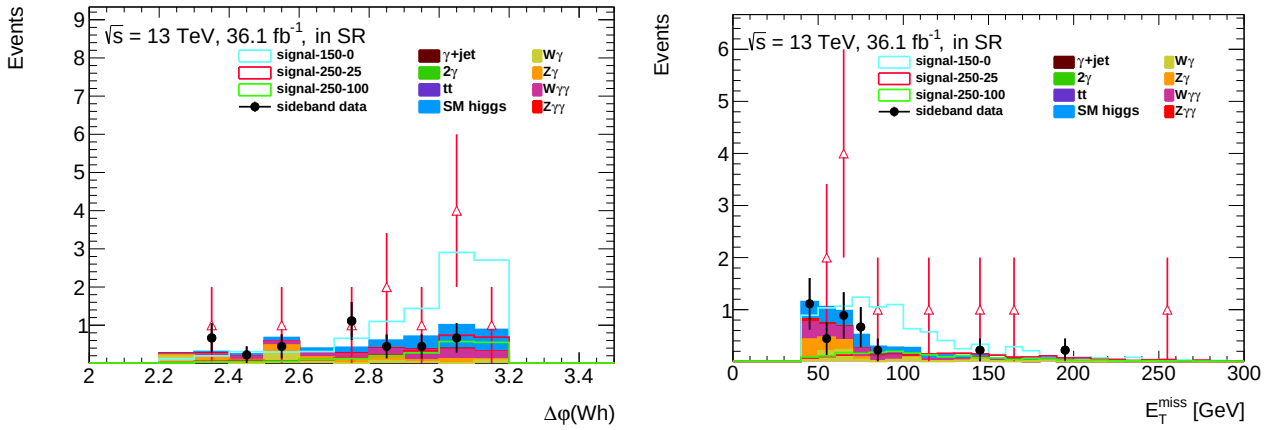

FigureA.1 Signal region distribution in $\Delta\phi(\mathrm{W},\mathrm{h})$ and $E_{\mathrm{T}}^{\mathrm{miss}}$.

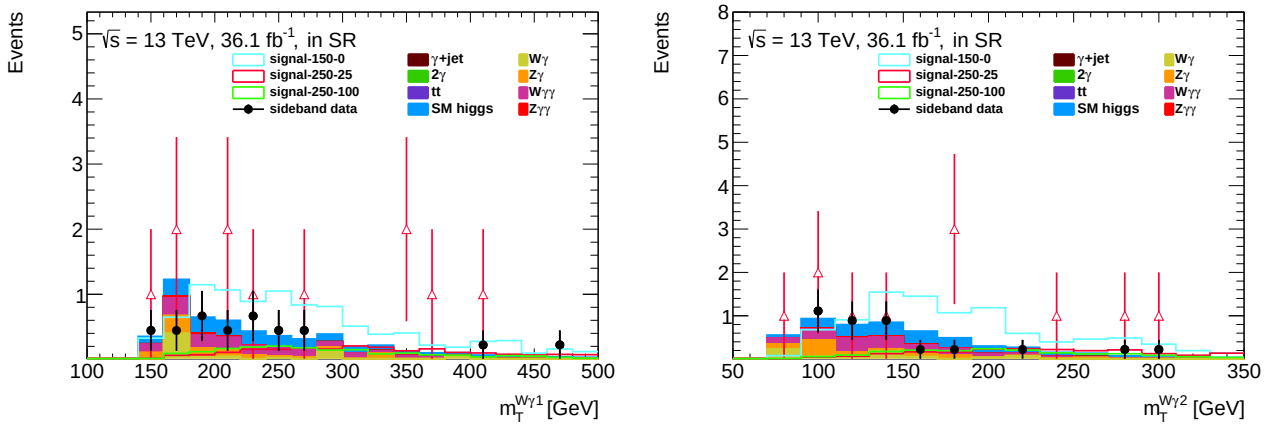

FigureA.2 Signal region distribution in $M_{\mathrm{T}}^{\mathrm{W}\gamma 1}$ and $M_{\mathrm{T}}^{\mathrm{W}\gamma 2}$

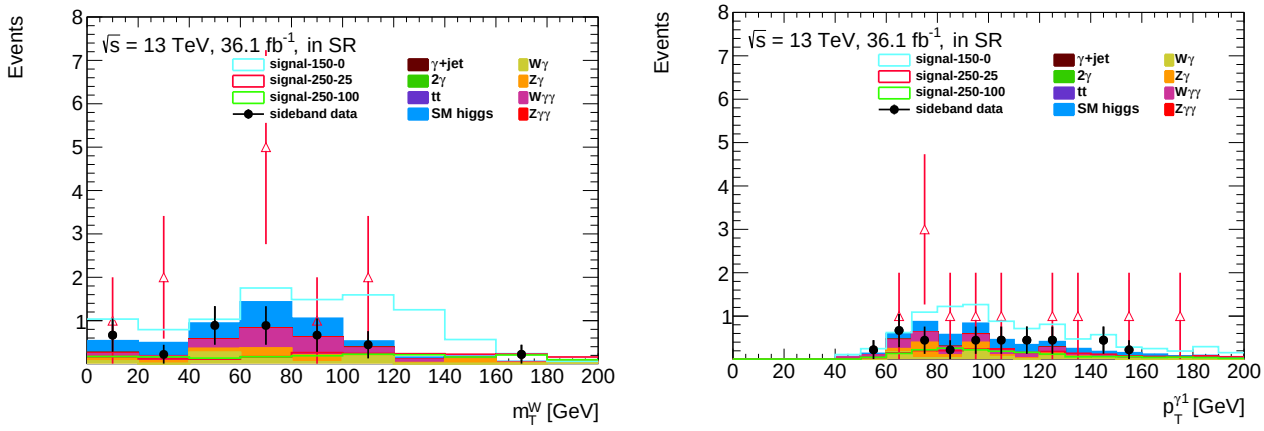

FigureA.3 Signal region distribution in $M_{\mathrm{T}}^{\mathrm{W}}$ and $p_{\mathrm{T}}^{\gamma 1}$.

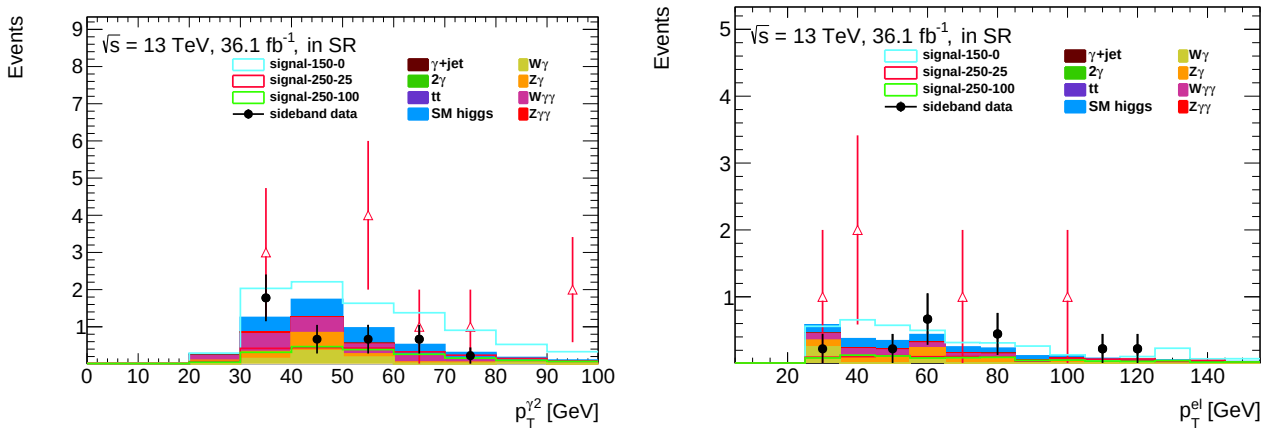

FigureA.4 Signal region distribution in $p_{\mathrm{T}}^{\gamma 2}$ and p_{T}^{e}.

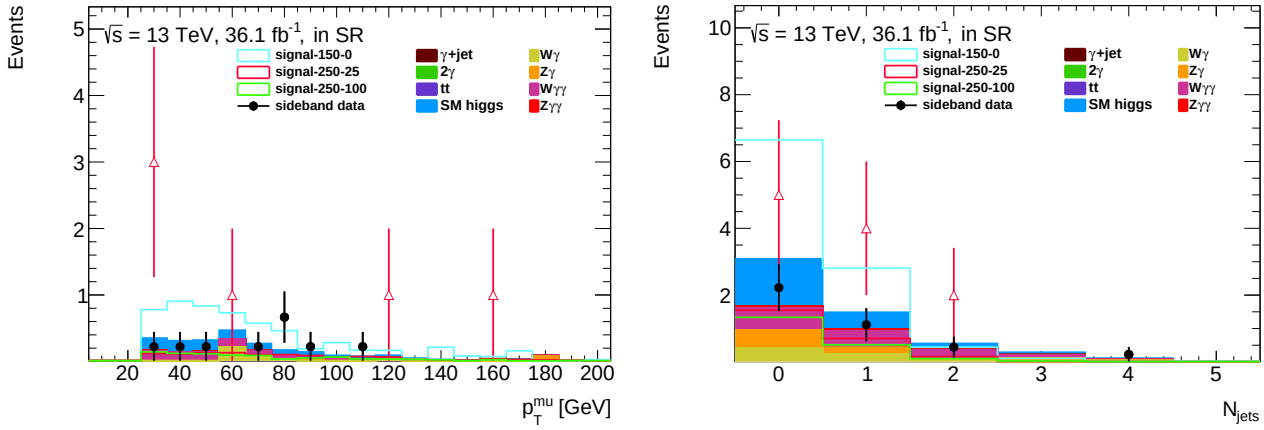

FigureA.5 Signal region distribution in p_{T}^{μ} and the number of jets.

TableA.3 Lepton vertex characteristics for the 11 signal events. The first two events fell into SRa and the final nine in SRd. The perfect agreement between the z positions of the lepton and primary vertices indicated that the lepton reference vertex was always found to be the reconstructed primary vertex.

Run	Event	z of PV (mm)	z of lepton vertex (mm)	d_0 (μm)	d_0 sig	z_0	$z_0 \sin\theta$
282712	922772599	-8.32	-8.32	-8.87	-0.490	-0.051	0.046
303892	4127378101	-5.30	-5.30	26.02	0.904	-0.023	-0.006
280423	81213163	88.43	(NA*1)	6.68	0.140	0.271	0.097
300863	1002432542	63.69	63.69	10.98	0.936	0.066	0.051
301973	567913060	65.80	65.80	-9.21	-0.300	0.021	0.014
302380	473324458	-11.91	-11.91	0.70	0.060	0.048	0.042
303208	5060330829	-9.82	-9.82	5.190	.320	0.043	0.034
304008	2769513232	25.65	25.65	-8.83	-0.897	0.006	0.004
309640	4285889264	18.58	18.58	2.49	0.231	-0.075	-0.025
310341	1548645619	-15.55	-15.55	-0.24	-0.019	-0.005	-0.003
310863	337227316	-25.10	-25.10	1.60	0.143	0.006	0.005

List of Figures

List of Tables